April 2019

Studies of the Long-term Change of Global Mean and Regional Sea Surface Height

Yingli Zhu
University of South Florida, zhuyingliouc@gmail.com

Studies of the Long-term Change of Global Mean and Regional Sea Surface Height

by

Yingli Zhu

A dissertation submitted in partial fulfillment
of the requirements for the degree of
Doctor of Philosophy
College of Marine Science
University of South Florida

Major Professor: Gary T. Mitchum, Ph.D.
Don P. Chambers, Ph.D.
Mark A. Merrifield, Ph.D.
Brad E. Rosenheim, Ph.D.
Philip R. Thompson Ph.D.

Date of Approval:
March 25, 2019

Keywords: Sea level, Background noise, Trend difference, Northeast Pacific, Temporal damping, Wave propagation

Dedication

This dissertation is dedicated to my parents Huxin Zhu and Quanhua Lu, for their unconditional love.

Acknowledgments

I would like to express my sincere gratitude to my advisor Gary T. Mitchum for his support, patience, and mentoring. I could never finish this dissertation without his continuing encouragement, enormous time input and ideas. I want to give my thanks to my committee members, Don P. Chambers, Mark A. Merrifield, Brad E. Rosenheim and Philip R. Thompson. Over the course of graduate studies, I also find many friends, making the student life more colorful. I am grateful for having support from friends, all the members of College of Marine Science and my family.

Table of Contents

List of Tables

List of Figures

Abstract

Sea level change could have profound impacts on our society. We report here on three related sea level change problems. First, a variety of regression models have predicted different rates for global mean sea level rise over the past century. Some of these models are accelerating and others are not. We ask whether we can distinguish between these using a new nonparametric noise model that we have developed. Simulations show that we can, and further imply that GMSL is rising at an accelerating rate. Second, historical global mean sea level is reconstructed from tide gauges that are located along coastlines and islands, but over the past 25 years we also have data from satellite altimeters that give global coverage. This raises the question as to whether there are differences between coastal and open-ocean sea level trends. Linear sea level trends from tide gauges, with and without vertical land motion corrections, are compared with the trends derived from altimetric observations in the nearby open ocean. The globally averaged trend difference is not significant, but at the regional scale there are possibly significant differences in some areas. These trend comparisons highlight the importance of having accurate estimates of vertical land motion for correcting tide gauge records. Finally, in contrast to global mean sea level change, which reflects ocean volume changes, regional sea level variations are mostly associated with water volume redistribution. Earlier work in the Northeast Pacific suggests that wave propagation and local damping are the two main mechanisms that might account for large-scale, low-frequency sea level variability, but these studies have reached conflicting conclusions. We develop a novel sea level model driven by wind, buoyancy and eddy forcing and including both mechanisms to examine their relative roles in the Northeast Pacific. The diagnosis demonstrates that

temporal damping is more important to the sea level response than propagation over most of the Northeast Pacific, while propagation plays a role in the southwest portion of the study region where the stresses associated with mesoscale eddies dominates.

Chapter 1

Introduction

Sea surface height (SSH), often called sea level, is a measure of water volume that depends on the density profile and the water mass loading in the water column. SSH rises with decreased density or addition of water to water column, and decreases with increased density or removal of water from water column. It changes on a range of spatiotemporal scales owing to a number of factors such as sea surface buoyancy and momentum flux, tides, ocean dynamic adjustments, geological processes, and so on. For example, wind stress over the ocean surface not only generates small-scale gravity waves lasting from seconds to minutes, but also induces downwelling or upwelling under the influence of the Coriolis force resulting in low-frequency SSH anomalies. Tides induced by the gravity effects of the sun and the moon show semi-diurnal, diurnal and other long-period sea level oscillations. Heat and fresh water flux over the ocean surface cause expansion or contraction, which result in a seasonal cycle of sea level. In addition, SSH anomalies may propagate a long distance via ocean dynamic adjustment such as propagation of Kelvin and Rossby waves. Besides redistribution of water mass within the ocean, water exchange between the land and ocean leads to sea level variations on seasonal or longer timescales. Proxy records also show that sea level underwent large fluctuations due to water exchange between the land and ocean and other tectonic processes in the past. Consequently, a full understanding and accurate projection of sea level change require significant continuing observation and study.

Understanding how sea level evolves across time and space is critical to our society. As more greenhouse gases are released into the atmosphere, the Earth gets warmer due to

the greenhouse effect. One of the consequences is a rising global mean sea level (GMSL) with a possible accelerating rate (e.g. Church and White (2011) [1]. Superimposed on the rising GMSL are nonuniform sea level rising rates that vary geographically around the global ocean. For example, the rising rate of sea level between 1992 to present over the west tropical Pacific is three times as high as the global mean, whereas it is close to zero and even negative over the east Pacific. Our society, especially low-lying coastal and island communities, are becoming increasingly concerned about the threats of sea level rise. As high tide, wave and mean sea level are superimposed, large extreme sea level events are more likely to happen, causing damages. At the end of this century, GMSL is projected to be tens of centimeters higher than the present level (Church et al., 2013 [2]), which will be a big challenge for the environment and management of coastal areas. Since SSH can approximately reflect heat content and ocean dynamic processes, it is also a substantial variable for studying ocean dynamics and climate change. For example, SSH measured by satellite altimeter provides opportunities of investigating global Rossby waves and eddies (e.g. Chelton and Schlax, 1996 [3]; Chelton et al., 2011 [4]). Sea level can also be used to calculate ocean surface circulation and heat transport, giving us more insights into ocean physics (e.g. Bonjean and Lagerloef, 2002 [5]; Kelly et al., 2014 [6]). Therefore, it is critical to understand how global and regional sea level changed in the past and what processes drove the changes, which help us improve projections of the future sea level and provide more scientific information of sea level change for the society and policy makers.

This study is focused on low-frequency sea level variations during the period with continuous and long instrumental sea level records, approximately from the late 19th century to present. There are two sets of instrumental observation of sea level being exploited to reveal how sea level changed globally and regionally. The earliest instrumental observations of sea level came from tide gauges dating back to the 18th century in Europe. Today the number of tide gauge has increased to thousands, and they are mainly located along the continental coasts with a few at open-ocean islands. The network of tide gauges provides

researchers with sea level records more than one hundred years long at some tide gauges, which allow studies of the long-term sea level variability on global mean or at individual station. However, they are limited by station sparsity with most of the open ocean not sampled. Satellite altimeter TOPEX/Poseidon (T/P) ushered in the era of continuous and nearly global measurement of sea level with high precision and resolution. T/P and the following missions, Jason-1, Jason-2, Jason-3 and other missions (e.g. European Remote Sensing (ERS)) have produced more than 25 years data, from which GMSL estimates more accurate than the previous estimates from tide gauges alone can be calculated. The dense data coverage over the global ocean makes it available to study large-scale, low-frequency variability over the open ocean. Based on these observations, this study consists of three projects: long-term change of GMSL; sea level trend differences between the coastal and open ocean; and low-frequency variability of SSH in the Northeast Pacific (NP). The three projects range from long-term change (on secular time scale) of GMSL to low-frequency (on interannual to decadal time scale) variations of regional sea level, with the eventual goal of giving more insights of how sea level has changed globally and regionally over roughly the past 100 years.

In the first project we note that GMSL has been rising since the late of 19th century, reflecting an integrated result of the global climate change. The rise of GMSL and how its rate changed in the past are a serious concern in a warmer climate, and will be investigated in the first project. The change of GMSL is determined by globally averaged density variation associated with temperature and salinity anomalies, and water mass variation related to water exchange between the ocean and land, with a small contribution from glacial isostatic adjustment (GIA). The long records at tide gauges are valuable for detecting the long-term variation such as the secular trend. The secular rising rates may differ from station to station and are accompanied by significant decadal and multi-decadal variations. When grouped by their locations and then averaged over the global ocean, these long sea level records yield a smoothed mean sea level that, however, could be biased by the sparse sampling. To take

regional variations of sea level into account, more complex statistical techniques such as EOF reconstruction are applied to derive GMSL (e.g. Church and White, 2006 [7]). GMSL derived either by the arithmetic average or by a complex statistical technique possesses a secular trend and low-frequency variations. Although the derived GMSL time series are not always consistent with each other because of differences in statistical techniques and the number of tide gauges used, it rose at a rate of about 1.7mm/year in 20th century, and rose at a larger rate in 21st century, indicating a possible acceleration (e.g. Merrifield et al., 2009 [8]). The accompanying low-frequency variations could either represent a change of the secular trend due to climate change or a multi-decadal natural oscillation.

It is common to use regression models to extract signals from noisy data. To extract long-term sea level variations, various models, including a quadratic model, a linear trend with a harmonic cycle, and piecewise trend model have been used, but no agreement has been reached as to how the rising rate changed in the past. In other words, it is unclear which model would more accurately describe long-term sea level change. An important question is whether we can distinguish these regression models used to explain long-term sea level change; if the answer is yes, then it comes to which model is the best one; if the answer is no, we cannot say which model is preferred. The traditional regression model comparison methods, such as the F test and J test, require that time series be independent or the regression model be nested when using F test. To overcome these limitations, a general noise model that captures the autocorrelation structure of noise in time series is needed to distinguish these GMSL models using Monte Carlo simulations. In this first project, a nonparametric noise model is developed based on a maximum likelihood estimator, and this model is used to distinguish between different regression models for GMSL.

In the second project we consider that GMSL trends over the last century are mainly derived from sea level records of tide gauges that are mostly located on the global coast, which casts doubt as to whether this reconstructed GMSL is able to represent the true GMSL that is predominantly determined by sea level in the open ocean (Holgate and Woodworth, 2004

[9]; White et al., 2005 [10]). Since the open-ocean wind stress and current can induce sea level change on the coast (Hong et al., 2000 [11]; Sallenger et al. 2012 [12]), the mechanisms of sea level variability on the coast might be different from those acting in the open ocean. For instance, the along-coast wind stress and coastal waves have been suggested to largely cause sea level changes along the coast (Enfield and Allen, 1980 [13]). In contrast, steric effects dominate sea level change in the open ocean (e.g. Suzuki and Ishii, 2011 [14]; Forget and Ponte, 2015 [15]). It is thus essential to know whether there are sea level trend differences between the coastal and open ocean.

In this second project, global and regional sea level trend differences of the coastal and nearby open ocean are investigated. Altimetry data close to the coast is likely contaminated by land, even though it has high precision in the open ocean. For now, sea level records on the coast mainly rely on tide gauge measurements that have been used to derive GMSL before the altimeter era. The estimate of GMSL from tide gauges largely represents coastal mean sea level (CMSL) that may deviate from the true GMSL for the global ocean. The decadal trend of CMSL was suggested to be larger than that of GMSL in the late 1990s. There are also some periods, such as the late 1970s and 1980s, when CMSL rose slower than GMSL. As the time series lengthens, the trend difference between CMSL and GMSL tends to decrease and is close to zero. It is recognized that sea level changes at tide gauges are induced by both water volume changes and vertical land movements (VLMs). VLMs are generated by GIA due to the post glacial rebound, tectonic activities, fluid extraction from underground and other factors. Few observations of VLMs existed during the time of these studies, so numerical simulations of GIA were often used to account for VLMs. However, GIA is no longer valid where the tectonic activities or other factors dominate VLMs. Position measurements at GPS stations collocated with tide gauges are now available for estimate of VLMs. The increasing number of GPS stations and longer records enable us to correct tide gauge sea level for VLMs. With the coastal sea level from tide gauges corrected for VLMs and sea level observed by satellite altimeters in the nearby open ocean, sea level trend differences

are investigated globally and regionally. Moreover, ocean processes probably responsible for regional sea level trend differences are examined.

In the third project, we turn to the regional sea level variations that are as important as GMSL for local communities and are more associated with water volume redistribution in the ocean. Altimetry observations enable us to examine low-frequency climate variations that have profound fingerprints in sea level. El Niño-Southern Oscillation (ENSO) is one the most prominent climate modes that has global influences through ocean pathways and the atmosphere teleconnection. Studying the regional low-frequency sea level variability is an important way to understand climate modes, favoring sea level projections. This project is focused on the eastern North Pacific (NP) where there are two primary climate modes that influence climate and ecosystem, which are the Pacific Dedadal Oscillation (PDO) and the North Pacific Gyre Oscillation (NPGO). These are represented by the first and second EOF modes of the SSH field, respectively (Cummins et al., 2005 [16]; Di Lorenzo et al., 2008 [17]).

Local wind stress forcing via Ekman pumping, buoyancy forcing via altering water density, and eddy activities all contribute to sea level variations. The roles of external forcing and internal modes are suggested to be nonuniform over the ocean with one or multiple factors dominating in a specific region (Vivier eta al., 1999 [18]; Cabanes et al., 2006 [19]). Views on the source of the low-frequency variability in the NP ocean are highly divided due to the teleconnection between tropical and extratropical regions and the coupling of ocean and atmosphere. Regardless of the source of wind stress anomalies, previous researchers have simulated the SSH variability with a linear damping model (Lagerloef, 1995 [20]), a first-mode baroclinic Rossby wave model (Qiu, 2002 [21]), and a model including both the damping and the Rossby wave (Cummins and Lagerloef, 2004 [22]; Capotondi et al., 2005 [23]; Capotondi et al., 2009 [24]). Most of the previous studies show similar performances, and no single model has an advantage over the others, which leads to the following question. What are the relative roles of wave propagation and linear damping in controlling low-frequency sea level variations?

Although wind stress can account for a large fraction of variability in the interior NP, it failed to account for sea level variations over some regions. Buoyancy and eddy momentum fluxes are shown to play important roles in the subtropical North Pacific and in the North Pacific drift, respectively (Thompson and Ladd 2004 [25]; Qiu et al., 2015 [26]). Therefore, the relative roles of each external forcing, wave propagation and linear damping are open to question. In this third project, a novel diagnostic framework is developed to examine the mechanisms of low-frequency variability of SSH in the NP.

In summary, tide gauge and altimeter sea level data are exploited to study long-term sea level variations ranging from global mean secular changes to regional low-frequency variations. In chapter 2, regression models predicting long-term GMSL change are statistically distinguished based on a newly developed noise model. In chapter 3, sea level trend differences between the coastal and open ocean are examined and the ocean processes responsible for the regional trend differences are examined as well. In chapter 4, a novel sea level diagnostic model is developed to reveal the roles of wave propagation, linear damping and external forcing in driving the large-scale, low-frequency sea level variations in the NP.

Chapter 2

Distinguishing between Regression Models of Global Mean Sea Level Reconstructions

2.1 Introduction

As an indicator of climate change, global mean sea level (GMSL) rises under a warming climate, causing an environmental concern for coastal communities. Before the satellite altimeter era, sea level records are mainly from tide gauges located along continental coasts and on islands, and multiple statistical methods have been applied to reconstruct GMSL for the last century (Douglas, 1991 [27]; Chambers et al., 2002 [28]; Holgate and Woodworth, 2004 [9]; Jevrejeva et al., 2008 [29]; Wöppelmann et al., 2009 [30]; Church and White, 2011 [1]; Ray and Douglas, 2011 [31]; Calafat et al., 2014 [32]; Hay et al., 2015 [33]). The rate seems to change through the record, however, no consensus on how it has changed has been reached from the analysis of the models mentioned above.

As I said, a variety of regression models have been used to describe sea level variability in the literature. Generally, there are three types of regression models used to account for the long-term rate change in GMSL of more than one century. The first one typically used is the quadratic polynomial model. Fitting a quadratic model to GMSL yields an acceleration since the 19th century (Church and White, 2006 [7]; Jevrejeva et al., 2008 [29]; Church and White, 2011 [1]; Woodworth et al., 2011 [34]; Jevrejeva et al., 2014 [35]). The change of sea level rising rate is not necessarily uniform throughout the period. The second type of model is a stepwise trend model that includes several knots at which linear trend changes its value. Previous studies show that GMSL may have experienced three rate changes since the

late 19th century, an increasing rate in 1930s, a decreasing rate in 1960s, and an increasing rate in 1990s (Church and White, 2006 [7]; Jevrejeva et al., 2006 [36]; Holgate, 2007 [37]; Jevrejeva et al., 2008 [29]; Woodworth et al., 2009 [38]; Merrifield et al., 2009 [8]). These relatively high and low rates are respectively ascribed to the low-level volcanic activities in the first half 20th century and large volcanic eruptions since 1960s that offset some of the acceleration (Church et al., 2005 [39]; Church and White, 2006 [7]). The acceleration after 1990 was due to a transfer from out-of-phase to in-phase variation in the tropical and southern oceans (Merrifield et al., 2009 [8]). These rate changes may, however, reflect a natural oscillation and the third type of model is a linear trend plus a long-term harmonic oscillation. Chambers et al. (2012) [40] examined long records from tide gauges with this model, suggesting the possible existence of a quasi 60-year oscillation in GMSL. The fast sea level rise from 1920 to 1950 is also suggested to be caused by a combination of a peaking of the 60-year cycle with the low-level volcanic activity (Jevrejeva et al., 2008 [29]). The three types of models imply distinct physical processes and desire an examination of their differences. Distinguishing sea level models commonly used in literatures can give us insight of how GMSL changed in the past century and enable better projections of future sea level.

Accurate uncertainty estimates of the regression coefficients and comparisons between regression models require knowledge of the background noise (for a recent review see Bos et al., 2014 [41]). Data points in observed time series are often not independent but serially correlated. Chambers et al., 2002 [28] showed significant low-frequency variabilities superimposed on the long-term trend in GMSL. The low-frequency components such as El Niño-Southern Oscillation (ENSO) and Pacific Decadal Oscillation (PDO) can obscure the real long-term sea level change and contribute to short-term trend (Calafat and Chambers, 2013 [42]; Hamlington et al., 2013 [43]; Haigh et al., 2014 [44]). With the large low-frequency variations in the time series, the significance of the acceleration of the GMSL rate should be accessed with caution (Beckley et al., 2007 [45]; Hamlington et al., 2013; [43] Jord, 2014 [46]). Consequently, autocorrelation should be carefully evaluated instead of simply assum-

ing a white noise model. Autocorrelation functions such as the first order Markov function or a Gaussian function are commonly used to characterize noise (Nerem and Mitchum, 2002 [47]). In addition, the noise can also be characterized by its frequency spectrum, described by a number of functions, such as power-law function (Mao et al., 1999 [48]; Becker et al.,2014 [49]), autoregressive function of order one (AR(1)) (Ghil et al, 2002 [50]), Autoregressive-Integrated-Moving average (ARIMA) class of models (Ocana et al., 2016 [51]), or a combination of white and colored spectrum (Williams and Willis, 2006 [52]). An advantage of using the noise frequency spectrum is that it can be easily used to generate noise realizations for Monte Carlo simulations. Although the power-law and autoregressive noise models are most often better noise models than white noise, the spectral shape may vary from series to series. For example, the sea level residual spectrum at one tide gauge fits well to an AR(1) model, while the spectrum of one GPS residual time series has the shape of power law (Doran, 2010 [53]). Choosing the wrong noise model could cause an overestimation or underestimation of the error variance by a factor of 5 or more (Doran, 2010 [53]). Hughes and Williams (2010) [54] also point out that the assessment of the statistical error depends on the amplitude of variability and the assumed shape of noise spectrum. So comparing regression models that describe GMSL also requires an accurate noise model estimation, which we suggest is an unsolved problem. In this chapter, however, we suggest a novel approach to this problem and apply this new method to address the question of whether accelerating versus non-accelerating regression models for GMSL can be distinguished, and further, whether different types models in each of these two classes can be separated.

In addition to the problem of not knowing the correct shape of the noise spectrum, caution must be taken when deriving the noise spectrum from the residual of a regression model. Applying a regression model to a time series, like subtracting a trend, changes the temporal correlation structure (Diggle, 1990 [55]). Some variance is removed from the noise by regression models at frequencies where the regression model has spectral power. This problem was referred to as overfitting by Doran (2010) [53], who showed that it causes an

underestimation bias of true noise. Traditional noise models do not address this overfitting problem.

A nonparametric noise model, taking into account overfitting problem, is developed, providing basis for regression model comparisons. Data and method are presented in the next section. Fitting procedures of the nonparametric model are described in detail in section 2.3, and model performance is compared with a parametric model as well as other traditional noise models via Monto Carlo simulations, demonstrating the advantages of the new noise model. In the section 2.4, six regression models predicting reconstructed GMSL are distinguished by Monto Carlo simulations based on the new nonparametric noise model. Conclusions and discussions are presented in the last section.

2.2 Data and method

2.2.1 Data

In this study, GMSL reconstructed by Church and White (2011) [1] is used, which is downloaded from http://www.cmar.csiro.au/sealevel/sl_data_cmar.html. The monthly GMSL time series from 1880 to 2013 was reconstructed by combining tide gauge sea level with spatial functions estimated from altimeter observed sea level, providing us a sea level record long enough for studying long-term rate change.

2.2.2 Method

A set of samples of one process is typically composed of signal and noise. Noise could arise from a variety of sources, like sampling or instrument error, and often is characterized by spectrum. On one hand, the shape of noise spectrum is unknown. On the other hand, the temporal correlation structure of noise can be changed by data processing like regression (Diggle, 1990 [55]) or smoothing. The reduction of noise variance by fitting regression model is also reported and referred to as overfitting by Doran (2010) [53]. An approach of estimating

noise spectrum based on maximum likelihood is developed, with the influence of regression model on noise taken into account.

2.2.2.1 Maximum likelihood estimate based on noise periodogram

First, we consider the simple case without involving regression models. The Fourier transform of a random, stationary time series, x_n, with a Gaussian distribution, is defined as

$$G(x_n) = X_k + iY_k$$

with

$$X_k = \sum_n x_n c_{nk}$$
$$Y_k = \sum_n x_n s_{nk}$$

and c_{nk}, s_{nk} are the cosine and sine terms defined by

$$c_{nk} = \cos \frac{2\pi nk}{N}$$
$$s_{nk} = \sin \frac{2\pi nk}{N}$$

where n is time index, k is frequency index, and N is data length.

Since a linear combination of normal variables is itself normally distributed (Priestley, 1981 [56]), X_k and Y_k are also Gaussian variables. If X_k and Y_k have the same variance and an orthogonality relation that is

$$X_k = N(0, \sigma_k^2)$$
$$Y_k = N(0, \sigma_k^2)$$
$$cov(X_k, Y_k) = 0$$

the periodogram, $P_k = X_k^2 + Y_k^2$, normalized by the variance has a chi-square distribution, i.e.

$$\frac{P_k}{\sigma_k^2} \sim \chi_2^2$$

When $k = \frac{n}{2}$ and n is even, Y_k is equal to zero with zero variance, resulting in

$$\frac{P_k}{\sigma_k^2} \sim \chi_1^2$$

For simplicity, this situation is nevertheless ignored here because the noise energy at the highest frequency is so small that it is negligible, and χ_2^2 distribution hold at all frequencies. Given $E(P_k) = S_k$ where S_k is the noise spectrum and mean value of χ_2^2 being equal to two, it follows that

$$\sigma_k^2 = \frac{S_k}{2}$$

hence,

$$\frac{2P_k}{S_k} \sim \chi_2^2$$

It is common to convert periodogram and spectrum into logarithmic form (Lee and Wong, 2003 [57]), and the probability density function (PDF) of $ln\frac{P_k}{S_k}$ is

$$g\left(ln(\frac{P_k}{S_k})\right) = exp\left\{ln(\frac{P_k}{S_k}) - \frac{P_k}{S_k}\right\}.$$

Given a PDF, the measure of likelihood or probability of obtaining a set of data could be approximated as $\prod_k g_k\Delta$, where g is PDF and Δ is a constant that can be ignored. Maximum likelihood estimates of parameters in PDF are those that maximize the likelihood function, which is equivalent to minimizing the minus log-likelihood

$$l = -\sum_k ln(g_k).$$

Based on this probability density function, the log-likelihood of log-spectrum is

$$l(ln(S)) = \sum_k \left\{ \frac{P_k}{S_k} - ln(\frac{P_k}{S_k}) \right\}.$$

which is the merit function consistent with that described by Ruddick et al.(2000) [58]. Given noise periodogram P, spectrum S is estimated by minimizing the merit function $l(ln(S))$.

2.2.2.2 Maximum likelihood estimate based on Fourier coefficients of model residual

Since our knowledge of background noise is usually retrieved from the residual of regression model, now we consider the case involving regression models. In matrix form, one regression model can be expressed as

$$Z = AL + E$$

where Z is observation vector with elements of x_n, A is regression matrix, L is regression coefficient vector, and E is noise vector. In addition to true signals, part of noise variance is treated as signal and removed by regression. To utilize Doran's (2010) [53] derivation of spectrum estimation from residual spectrum, an arbitrary linear regression matrix, A, is orthogonalized by Gram-Schmit process into an matrix Q times an upper triangular matrix R. Regression model becomes

$$Z = QRL + E = QB + E$$

where B is regression coefficient vector when regression matrix is Q, and can be transformed back to L by $L = R^{-1}B$. The resulting residual $\hat{x}_n$ of the regression model that is elements in E, is written as

$$\hat{x}_n = x_n - \sum_i \beta_i f_{ni},$$

where β_i are errors of fit coefficients in B, and f_{ni} are orthonormal basis functions in Q. The Fourier transform of $\hat{x}_n$ is written as

$$G(\hat{x}_n) = \hat{X}_k + i\hat{Y}_k$$

where $\hat{X}_k$ and $\hat{Y}_k$ are defined by the same way as X_k and Y_k.

Fitting regression model to noise not only reduces power spectrum density at frequencies where the regression model has impacts, but also changes covariance of $\hat{X}_k$, $\hat{Y}_k$. For instance, the trend model has the biggest influence at the lowest frequency, and $\frac{2P_k}{S_k}$ at that frequency no longer follows χ^2 distribution.

Doran (2010) [53] developed a relationship between the residual spectrum $\hat{S}_k$ and the true noise spectrum S_k, written as

$$\hat{S}_k = S_k + \frac{1}{N^2}\sum_p S_p \sum_i \sum_j S_k^{ij} S_p^{ij} - \frac{2}{N} S_k \sum_i S_k^{ii}$$

where i, j are basis function index, p is also frequency index and

$$S_k^{ij} = Re(F_{ki} F_{kj}^*)$$
$$S_k^{ii} = F_{ki} F_{ki}^*$$

where F is Fourier transform of basis function f, and is defined by the same way as G; asterisk symbol represents complex conjugate. Doran applied an iteration method to estimate S_k from $\hat{S}_k$ but with some errors.

Here a solution with a compact form is given. Define $\hat{S} \equiv [\hat{S}_1 \quad \hat{S}_2 \quad \cdots \quad \hat{S}_2]^T$, $S \equiv [S_1 \quad S_2 \quad \cdots \quad S_k]^T$, and C a symmetric $k \times k$ matrix with elements

$$C_{kp} \equiv [1 - \frac{2}{N}\sum_i S_k^{ii}]\delta_{kp} + \frac{1}{N^2}\sum_i \sum_j S_k^{ij} S_p^{ij}$$

where δ_{kp} is the Kronecker delta defined as

$$\delta_{kp} = \begin{cases} 1 & k = p \\ 0 & k \neq p \end{cases}$$

This allows us to write

$$\hat{S} = CS$$

and thus

$$S = C^{-1}\hat{S}$$

assuming that the inverse exists.

Figure 2.1 demonstrates an example of how S and $\hat{S}$ are related. 10000 surrogate data are generated from a power-law noise, and a linear trend model is fitted to these data. The residual spectrum is estimated as the mean of the 10000 residual periodogram. It is apparent to see a lowered energy at the lowest frequency. The reduced variance in residual spectrum is successfully recovered by multiplying $\hat{S}$ with the inverse of C determined by the linear trend model.

Here two features are noticed. First, the residual and true spectrum are smooth and represented by expectation values of periodogram. One residual periodogram could also be corrected for overfitting by this relationship, but the correction is unstable with some negative values generated owing to noisy features of periodogram. The iteration method proposed by Doran (2010) [53] can give an approximate correction to the residual periodogram that is less accurate but stable. Second, if harmonic terms are included in a regression model, the correction is unstable because the inverse of C tends to be singular.

Because realizations of background noise, x_n, are random and independent from each other, Fourier transforms of fitted signal and residual are also random and independent. Since Fourier coefficients of noise, X_k and Y_k, are Gaussian variables, Fourier coefficients of fitted signal and residual are also Gaussian distributed. The Gaussian distribution is further

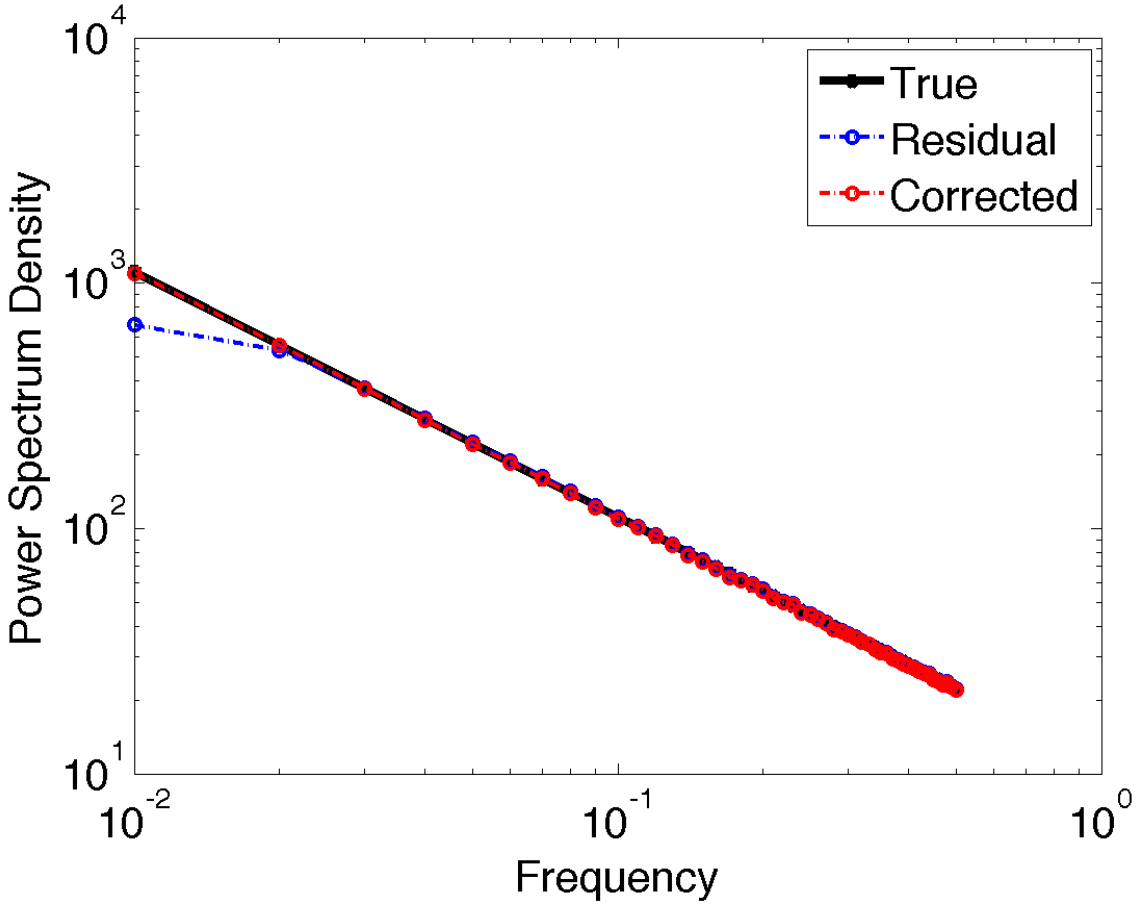

Figure 2.1: Power-law spectrum (black line), residual spectrum (blue line) from residuals of a linear trend model and corrected spectrum (red line) .

verified by Monte Carlo simulations. Seven regression models are fitted to 1000 realizations of 100-point noise generated from a noise model. The Fourier coefficients of residuals of the seven regression models are tested against the hypothesis that they follow the Gaussian distribution by using Kolmogorov-Smirnov (KS) test, Lilliefors test, Jarque-Bera test, and Shapiro-Wilk test. The null hypothesis is that the distribution shape of $\hat{X}_k$ or $\hat{Y}_k$ has a Gaussian shape, and the hypothesis is tested for $\hat{X}_k$ and $\hat{Y}_k$ separately. Additionally, the true noise realizations are tested against the Gaussian distribution for comparison. Red bars in Figure 2.2 and 2.3 show the cases that the hypothesis is rejected for the residual but not rejected for the true noise. Only few cases failed to pass the tests. Fourier coefficients of

model residual, $\hat{X}_k$ and $\hat{Y}_k$, both follow Gaussian distribution at significance level of 5%. Royston's and Henze-Zirkler's multivariate normality tests further demonstrate that the real and imaginary parts of Fourier coefficients at each frequency derived from the residuals have a bivariate normal distribution at significance level of 5% (Figure 2.4). Figure 2.4, same as Figure 2.2 and 2.3, shows the cases that the bivariate normality hypothesis is rejected for the residual but is not rejected for the true noise, indicating that $\hat{X}_k$ and $\hat{Y}_k$ follow a bivariate distribution.

These tests verify that $\hat{X}_k$ and $\hat{Y}_k$ both follow Gaussian distribution and they follow bivariate normality distribution with their variance and covariance shown as:

$$\hat{X}_k = N(0, \sigma^2_{\hat{X}_k})$$
$$\hat{Y}_k = N(0, \sigma^2_{\hat{Y}_k})$$
$$cov(\hat{X}_k, \hat{Y}_k) \neq 0$$

Next we derive expressions relating variance and covariance of $\hat{X}_k$ and $\hat{Y}_k$ to the background noise spectrum, S_k.

Taking Fourier transform of the residual gives

$$G(\hat{x}_n) = G(x_n) - \sum_i \beta_i F_{ki}$$

where F_{ki} is the Fourier transform of f_{ni}. This is equivalent to:

$$\hat{X}_k = X_k - \sum_i \beta_i \,\mathrm{Re}(F_{ki})$$
$$\hat{Y}_k = Y_k - \sum_i \beta_i \,\mathrm{Im}(F_{ki})$$

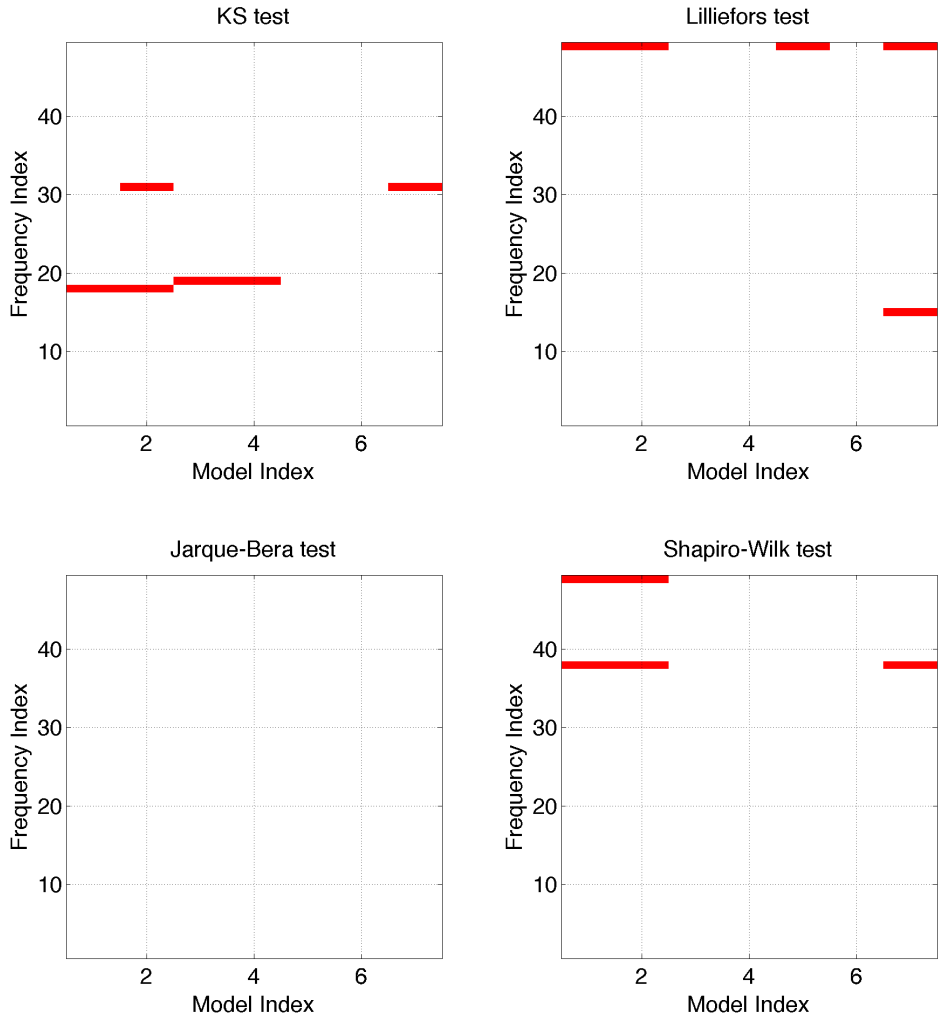

Figure 2.2: Gaussian distribution test of real part of Fourier transforms of 7 regression model residuals with four methods: KS test, Lilliefors test, Jarque-Bera test, and Shapiro-Wilk test. Red bars denote rejection of the null hypothesis.

Taking square on both sides of the two equations and multiplication of the two equations respectively yield

$$\hat{X}_k^2 = X_k^2 - 2X_k \sum_i \beta_i \operatorname{Re}(F_{ki}) + \sum_i \sum_j \beta_i \beta_j \operatorname{Re}(F_{ki}) \operatorname{Re}(F_{kj})$$

$$\hat{Y}_k^2 = Y_k^2 - 2Y_k \sum_i \beta_i \operatorname{Im}(F_{ki}) + \sum_i \sum_j \beta_i \beta_j \operatorname{Im}(F_{ki}) \operatorname{Im}(F_{kj})$$

$$\hat{X}_k \hat{Y}_k = X_k Y_k - X_k \sum_i \beta_i \operatorname{Im}(F_{ki}) - Y_k \sum_i \beta_i \operatorname{Re}(F_{ki}) + \sum_i \sum_j \beta_i \beta_j \operatorname{Re}(F_{ki}) \operatorname{Im}(F_{kj})$$

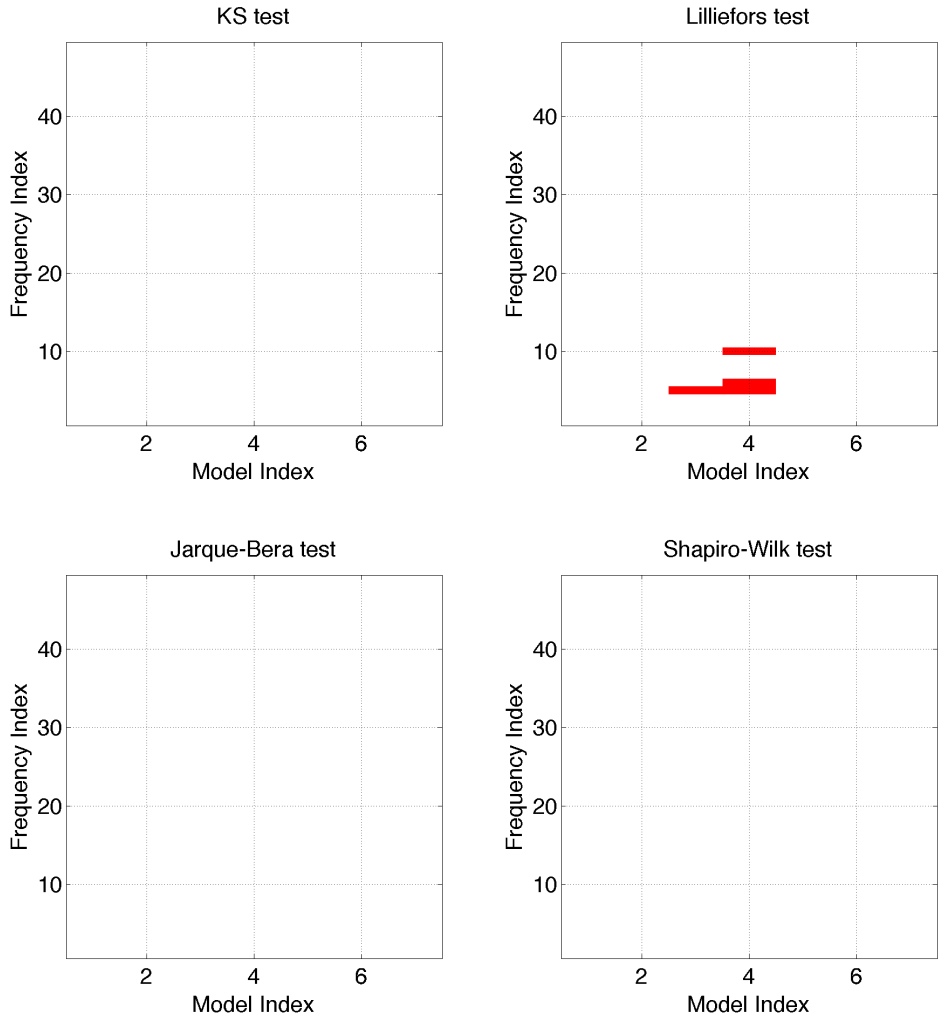

Figure 2.3: Same as Figure 2.2 but for imaginary part of Fourier transforms.

Expectation values, $E[\hat{X}_k^2]$, $E[\hat{Y}_k^2]$, and $E[\hat{X}_k\hat{Y}_k]$, are variance and covariance, i.e.

$$\sigma^2_{\hat{X}_k} = E[\hat{X}_k^2]$$
$$\sigma^2_{\hat{Y}_k} = E[\hat{Y}_k^2]$$
$$\sigma_{\hat{X}_k\hat{Y}_k} = E[\hat{X}_k\hat{Y}_k]$$

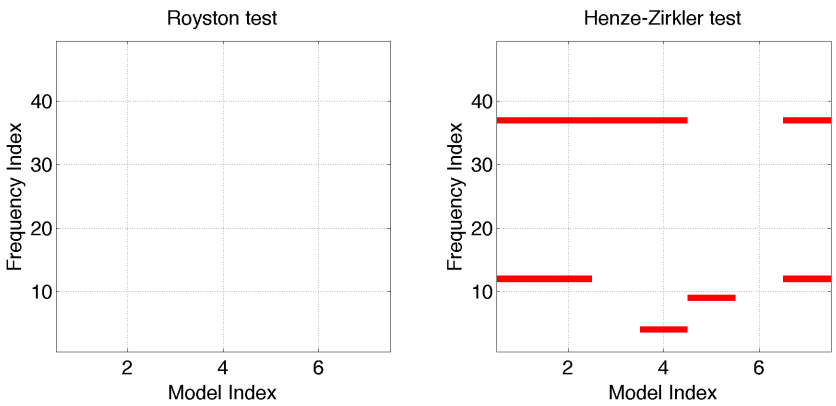

Figure 2.4: Multivariate normality test of Fourier transforms of 7 regression model residuals with two methods: Royston test, Henze-Zirkler test. Red bars denote rejection of the null hypothesis.

where $\sigma_{\hat{X}_k\hat{Y}_k}$ denotes the covariance, $cov(\hat{X}_k, \hat{Y}_k)$.

We have already known that

$$E[X_k^2] = E[Y_k^2] = \sigma_k^2 = \frac{S_k}{2}$$
$$E[X_k Y_k] = 0$$

By taking expectation for the three equations, it follows that

$$\sigma_{\hat{X}_k}^2 = \frac{S_k}{2} - 2\sum_i E[X_k\beta_i]\,\mathrm{Re}(F_{ki}) + \sum_i\sum_j E[\beta_i\beta_j]\,\mathrm{Re}(F_{ki})\,\mathrm{Re}(F_{kj})$$
$$\sigma_{\hat{Y}_k}^2 = \frac{S_k}{2} - 2\sum_i E[Y_k\beta_i]\,\mathrm{Im}(F_{ki}) + \sum_i\sum_j E[\beta_i\beta_j]\,\mathrm{Im}(F_{ki})\,\mathrm{Im}(F_{kj})$$
$$\sigma_{\hat{X}_k\hat{Y}_k} = -\sum_i E[X_k\beta_i]\,\mathrm{Im}(F_{ki}) - \sum_i E[Y_k\beta_i]\,\mathrm{Re}(F_{ki}) + \sum_i\sum_j E[\beta_i\beta_j]\,\mathrm{Re}(F_{ki})\,\mathrm{Im}(F_{kj})$$

According to Doran's derivation, the three following equations hold.

$$E[X_k\beta_i] = \frac{1}{N}S_k\,\mathrm{Re}(F_{ki})$$
$$E[Y_k\beta_i] = \frac{1}{N}S_k\,\mathrm{Im}(F_{ki})$$
$$E[\beta_i\beta_j] = \frac{1}{N^2}S_k S_k^{ij}$$

Substituting them into the variance and covariance equations gives

$$\sigma^2_{\hat{X}_k} = \frac{S_k}{2} - \frac{2}{N} S_k \sum_i \mathrm{Re}(F_{ki})\,\mathrm{Re}(F_{ki}) + \frac{1}{N^2}\sum_p S_p \sum_i \sum_j \mathrm{Re}(F_{ki})\,\mathrm{Re}(F_{kj}) S_p^{ij}$$

$$\sigma^2_{\hat{Y}_k} = \frac{S_k}{2} - \frac{2}{N} S_k \sum_i \mathrm{Im}(F_{ki})\,\mathrm{Im}(F_{ki}) + \frac{1}{N^2}\sum_p S_p \sum_i \sum_j \mathrm{Im}(F_{ki})\,\mathrm{Im}(F_{kj}) S_p^{ij}$$

$$\sigma_{\hat{X}_k\hat{Y}_k} = -\frac{2}{N} S_k \sum_i \mathrm{Re}(F_{ki})\,\mathrm{Im}(F_{ki}) + \frac{1}{N^2}\sum_p S_p \sum_i \sum_j \mathrm{Re}(F_{ki})\,\mathrm{Im}(F_{kj}) S_p^{ij}$$

Define $\sigma^2_{\hat{X}} \equiv [\sigma^2_{\hat{X}_1} \quad \sigma^2_{\hat{X}_2} \quad \cdots \quad \sigma^2_{\hat{X}_k}]^T$, $\sigma^2_{\hat{Y}} \equiv [\sigma^2_{\hat{Y}_1} \quad \sigma^2_{\hat{Y}_2} \quad \cdots \quad \sigma^2_{\hat{Y}_k}]^T$, $\sigma_{\hat{X}\hat{Y}} \equiv [\sigma_{\hat{X}_1\hat{Y}_1} \quad \sigma_{\hat{X}_2\hat{Y}_2} \quad \cdots \quad \sigma_{\hat{X}_k\hat{Y}_k}]^T$ as variance and covariance vectors. $C^{\hat{X}}$, $C^{\hat{Y}}$, $C^{\hat{X}\hat{Y}}$ are square matrices with elements

$$C^{\hat{X}}_{kp} = [\frac{1}{2} - \frac{2}{N}\sum_i \mathrm{Re}(F_{ki})\,\mathrm{Re}(F_{ki})]\delta_{kp} + \frac{1}{N^2}\sum_i\sum_j \mathrm{Re}(F_{ki})\,\mathrm{Re}(F_{kj}) S_p^{ij}$$

$$C^{\hat{Y}}_{kp} = [\frac{1}{2} - \frac{2}{N}\sum_i \mathrm{Im}(F_{ki})\,\mathrm{Im}(F_{ki})]\delta_{kp} + \frac{1}{N^2}\sum_i\sum_j \mathrm{Im}(F_{ki})\,\mathrm{Im}(F_{kj}) S_p^{ij}$$

$$C^{\hat{X}\hat{Y}}_{kp} = [-\frac{2}{N}\sum_i \mathrm{Re}(F_{ki})\,\mathrm{Im}(F_{ki})]\delta_{kp} + \frac{1}{N^2}\sum_i\sum_j \mathrm{Re}(F_{ki})\,\mathrm{Im}(F_{kj}) S_p^{ij}$$

Then we obtain

$$\sigma^2_{\hat{X}} = C^{\hat{X}} S$$

$$\sigma^2_{\hat{Y}} = C^{\hat{Y}} S$$

$$\sigma_{\hat{X}\hat{Y}} = C^{\hat{X}\hat{Y}} S$$

$\hat{X}$ and $\hat{Y}$ have a bivariate normal distribution with PDF

$$f(\hat{X}_k, \hat{Y}_k) = \frac{1}{2\pi\sigma_{\hat{X}_k}\sigma_{\hat{Y}_k}\sqrt{1-\rho_k^2}} exp\left\{\frac{-1}{2(1-\rho_k^2)}\left[\frac{\hat{X}_k^2}{\sigma^2_{\hat{X}_k}} + \frac{\hat{Y}_k^2}{\sigma^2_{\hat{Y}_k}} - 2\rho_k\frac{\hat{X}_k\hat{Y}_k}{\sigma_{\hat{X}_k}\sigma_{\hat{Y}_k}}\right]\right\}$$

where ρ_k is correlation

$$\rho_k = \frac{\sigma_{\hat{X}_k\hat{Y}_k}}{\sigma_{\hat{X}_k}\sigma_{\hat{Y}_k}}$$

The PDF also can be written as

$$f(\hat{X}_k, \hat{Y}_k) = \frac{1}{2\pi|\Lambda|^{\frac{1}{2}}} exp\left\{-\frac{1}{2}\begin{bmatrix}\hat{X}_k \\ \hat{Y}_k\end{bmatrix}\Lambda^{-1}\begin{bmatrix}\hat{X}_k & \hat{Y}_k\end{bmatrix}\right\}$$

where covariance matrix $\Lambda = \begin{bmatrix}\sigma^2_{\hat{X}_k} & \rho_k\sigma_{\hat{X}_k}\sigma_{\hat{Y}_k} \\ \rho_k\sigma_{\hat{X}_k}\sigma_{\hat{Y}_k} & \sigma^2_{\hat{Y}_k}\end{bmatrix}$ is positive definite, $|\Lambda|$ is its determinant, and $\sigma_{\hat{X}_k} > 0$, $\sigma_{\hat{Y}_k} > 0$, $|\rho| \leq 1$.

The minus log-likelihood based on the bivariate normal distribution is

$$\begin{aligned} l &= -\sum_k ln(f_k) - \sum_k ln(\Delta) \\ &= -\sum_k ln(\Delta) + \sum_k ln(2\pi) + \frac{1}{2}\sum_k \left\{ln(\sigma^2_{\hat{X}_k}\sigma^2_{\hat{Y}_k} - \sigma^2_{\hat{X}_k\hat{Y}_k}) + \frac{\hat{X}_k^2\sigma^2_{\hat{Y}_k} + \hat{Y}_k^2\sigma^2_{\hat{X}_k} - 2\hat{X}_k\hat{Y}_k\sigma_{\hat{X}_k\hat{Y}_k}}{\sigma^2_{\hat{X}_k}\sigma^2_{\hat{Y}_k} - \sigma^2_{\hat{X}_k\hat{Y}_k}}\right\}. \end{aligned}$$

Neglecting the first two terms that are constant and the constant factor of the last term on the right hand side, the minus log-likelihood is simplified as

$$l = \sum_k \left\{ln(\sigma^2_{\hat{X}_k}\sigma^2_{\hat{Y}_k} - \sigma^2_{\hat{X}_k\hat{Y}_k}) + \frac{\hat{X}_k^2\sigma^2_{\hat{Y}_k} + \hat{Y}_k^2\sigma^2_{\hat{X}_k} - 2\hat{X}_k\hat{Y}_k\sigma_{\hat{X}_k\hat{Y}_k}}{\sigma^2_{\hat{X}_k}\sigma^2_{\hat{Y}_k} - \sigma^2_{\hat{X}_k\hat{Y}_k}}\right\}.$$

Substituting the equations of $\sigma^2_{\hat{X}_k}$, $\sigma^2_{\hat{Y}_k}$, and $\sigma_{\hat{X}_k\hat{Y}_k}$ related to noise spectrum into the equation of l yields

$$l = \sum_k \left\{ln([C_k^{\hat{X}}S][C_k^{\hat{Y}}S] - [C_k^{\hat{X}\hat{Y}}S]^2) + \frac{\hat{X}_k^2[C_k^{\hat{Y}}S] + \hat{Y}_k^2[C_k^{\hat{X}}S] - 2\hat{X}_k\hat{Y}_k[C_k^{\hat{X}\hat{Y}}S]}{[C_k^{\hat{X}}S][C_k^{\hat{Y}}S] - [C_k^{\hat{X}\hat{Y}}S]^2}\right\}. \quad (2.1)$$

This result is a generalization of section 2.2.2.1 in the sense that, if there is no fitting, i.e. X_k and Y_k have the same variance equal to $\frac{S}{2}$ and correlation between them is zero, then one retrieves the result of log-likelihood of log-spectrum in section 2.2.2.1.

2.3 Procedures of maximum likelihood estimation of noise spectrum and simulation tests

First, a parametric model that combine white noise, power-law noise, and AR(1) noise is described by a function with six parameters:

$$S_t = S_0(r1 * S_w + r2 * S_{pl}(\nu) + r3 * S_{ar1}(\rho)) \tag{2.2}$$

where S_0 is amplitude, $r1$, $r2$, $r3$ are proportion parameters for each component, ranging from 0 to 1 and constrained by $r1+r2+r3 = 1$; S_t is the true spectrum; S_w is the normalized white noise spectrum; S_{pl} is the normalized power-law spectrum as a function of log-spectrum slope, ν; S_{ar1} is the normalized AR(1) spectrum as a function of first order parameter, ρ.

This parametric model 2.2 is used to generate six types of noise (Table 2.1). Additionally, the parametric model 2.2, anticipated to be capable of comprehensively characterize the generated noise, will be fitted to these realizations to estimate the true spectrum. A new nonparametric model of spectrum is proposed and will be compared with the parametric one. Details of the two spectrum models and their fitting procedures will be described in the following sections.

If no regression model is involved, noise spectrum is estimated by minimizing the merit function with $C^{\hat{X}}$, $C^{\hat{Y}}$ being 0.5 times identity matrix, and $C^{\hat{XY}}$ being zero matrix. If one regression model is fitted to a time series, noise spectrum is estimated from the residual of regression model with matrix C, $C^{\hat{X}}$, $C^{\hat{Y}}$, and $C^{\hat{XY}}$ in the merit function determined by the regression matrix. Because zero variance of periodogram is not allowed in the merit function, the frequencies at which nearly no energy is left are not considered in the fitting procedure. As a result, the frequencies where

$$\left| \sum_p C_{kp} \right| < 10^{-6}$$

are not considered in the merit function.

In practice, it is common to preprocess raw data, for example, by smoothing, which tends to change spectrum features. The scenario that data is smoothed with 7-point moving average is considered to examine how smoothing changes model performance. Goodness of fitted spectrum with respect to the true spectrum are measured by root mean squared error (RMSE), which is defined by:

$$RMSE = \sqrt{\left\langle \left\{ \frac{S_{fit}(k) - S_t(k)}{S_t(k)} \right\}^2 \right\rangle}$$

where angle bracket denotes taking average over realizations. RMSE represents the extent to which fitted spectrum deviates from true spectrum.

Table 2.1: Noise types for simulation tests

Noise type	Noise parameters
Random	$r1, r2, r3, \nu, \rho$ are randomly drawn from uniform distribution for each realization. $0 <= r1, r2, r3 <= 1, \quad -1.5 <= \nu <= -0.5, \quad 0.8 <= \rho <= 0.95$
White	White noise $r1 = 1, \quad r2 = r3 = 0$
PL05	Power-law noise $r1 = r3 = 0, \quad r2 = 1, \quad \nu = -0.5$
PL15	Power-law noise $r1 = r3 = 0, \quad r2 = 1, \quad \nu = -1.5$
AR108	AR(1) noise $r1 = r2 = 0, \quad r3 = 1, \quad \rho = 0.8$
AR1095	AR(1) noise $r1 = r2 = 0, \quad r3 = 1, \quad \rho = 0.95$

2.3.1 Nonparametric model

A nonparametric model with monotonic and smooth shape is presented, and detailed procedures of estimating noise spectrum with the nonparametric model are described in this section.

2.3.1.1 Genetic algorithm

Since no analytical solution of spectrum exists, noise spectrum will be estimated by minimizing the merit function with genetic algorithm in natural logarithm space. The nonparametric model is a monotonic cubic spline calculated with Fritsch and Carlson's algorithm (1980) [59]. Spectrum values at spline knots are unknown parameters bounded by assigned upper and lower boundaries. Upper boundary is the maximum value of periodogram, and lower boundary is the minimum value of periodogram smoothed by five-point moving average. If regression model is involved, these upper and lower boundaries are from the residual periodogram corrected for overfitting with Doran's (2010) [53] iteration method. 5000 guesses of monotonic spline values at the spline knots are randomly generated from a uniform distribution within the given boundaries to yield spline function values at all frequencies. They are used in the calculation of the merit function, keeping the 20% guesses possessing the least merit function values. Then a new upper and lower boundary of spectrum are determined from these survived guesses. This process is repeated until spline values at the knots reach the criteria that ranges of spline values are less than 1‰of initial ranges. The final estimated noise spectrum is the one that minimize the merit function.

2.3.1.2 Knots selection

To find a proper knot number of spline, one million spectrum curves with 50 and 500 frequencies are generated using function 2.2 by randomly drawing parameters, $r1$, $r2$, $r3$ between 0 and 1, ν between -2 and 0, ρ between 0.5 and 0.99, from a uniform distribution. Monotonic cubic splines with 2 to 6 knots evenly located at log-frequency are fitted to these monotonically descending curves. Because the spline with more knots has a more flexible shape to match the true curve, the mean fitting error over all frequencies decreases with knot number. When the spline comprises two knots taking a shape of straight line in logarithmic space, most of the fitted curve have an error larger than 10% of the true. When the knot number is equal to or larger than 5, the error is smaller than 10% for all the curves with 50 frequen-

cies, and for more than 99% of the curves with 500 frequencies. To compromise between a smooth curve with small degree of freedom and small fitting error, five knots are chosen for this nonparametric model.

Although the five evenly spaced knots at log-frequency are able to account for spectrum variations at low frequency part, only two and four Fourier frequencies are located between the first two knots for spectrum curves with 50 frequencies and 500 frequencies, respectively. Knot positions should be adjusted to include an appropriate number of Fourier frequencies in the low frequency band for a more accurate spectrum estimation. One knot position scheme at log-frequency space, with a parameter δ, is designed as

$$knot = ln(\frac{N}{2}) * [0, \quad 0.25 + \delta, \quad 0.5 + \frac{\delta}{2}, \quad 0.75 + \frac{\delta}{4}, \quad 1] - ln(N)$$

where δ represents deviation of inner knots from the evenly spaced inner knots, and will be determined by a set of numerical simulations.

1000 realizations of time series are generated for each type of noise listed in Table 2.1. In this numerical experiment, no regression model is involved with $C^{\hat{X}}$, $C^{\hat{Y}}$ equal to 0.5 times identity matrix, and $C^{\hat{XY}}$ being zero matrix. A set of δ value, [0, 0.05, 0.1, 0.15, 0.2, 0.25], representing the amount of adjustment of the second knot position that varies from the second to third evenly spaced knot, is explored for the knot position scheme. Figure 2.5 and 2.6 show RMSE at the first frequency for cases with data length of 100 and 1000, respectively. RMSE decreases with increasing value of δ for some noise types like white and power-law noise, stays nearly unchanged with δ value larger than 0.15 for the AR(1) noise with data length of 100, or increases with δ for AR1095 noise with data length of 1000. Based on these results, a moderate value of δ, 0.125, is chosen for the knot position scheme.

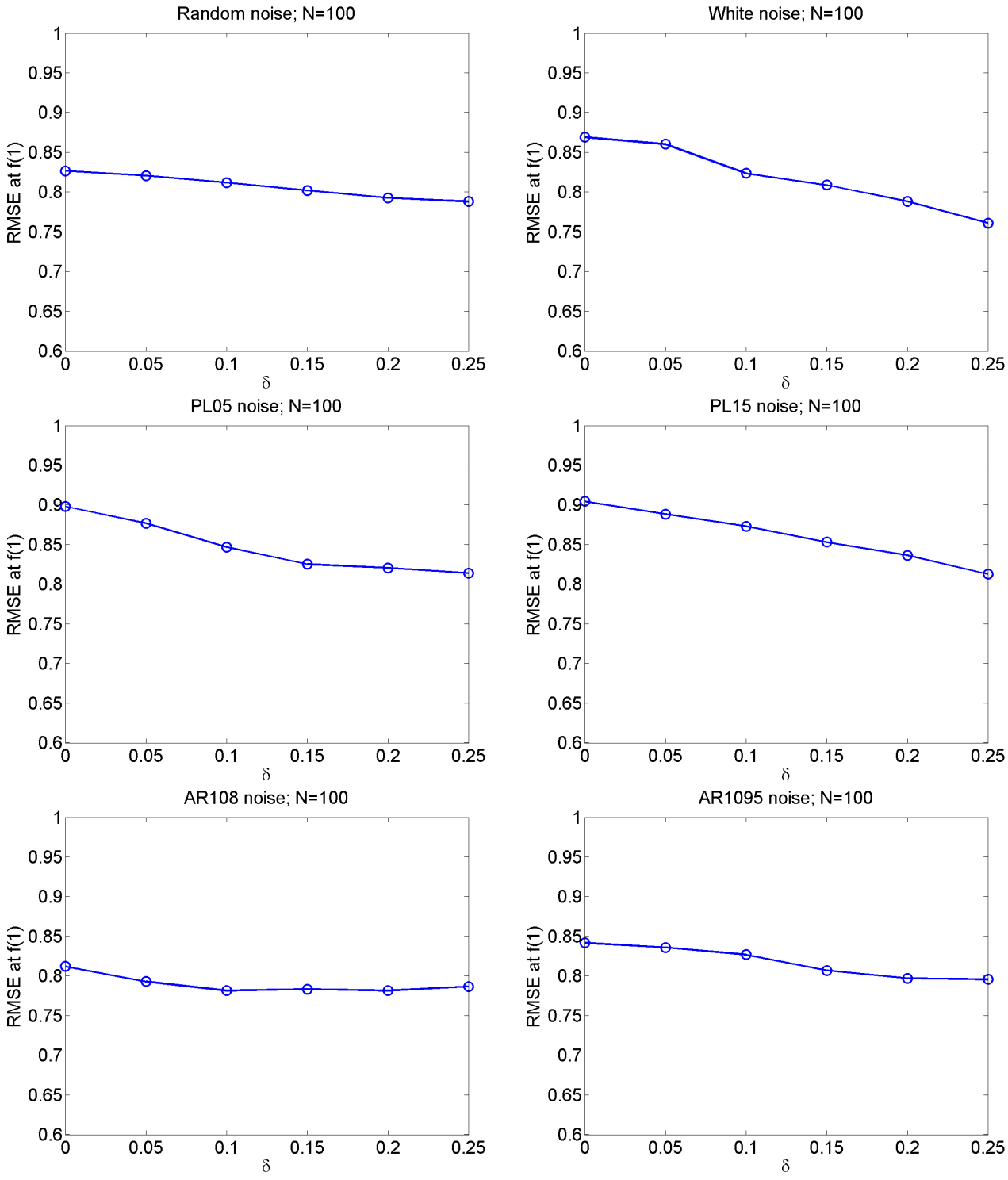

Figure 2.5: RMSE at the first frequency with different δ value representing different knot schemes; data length is 100.

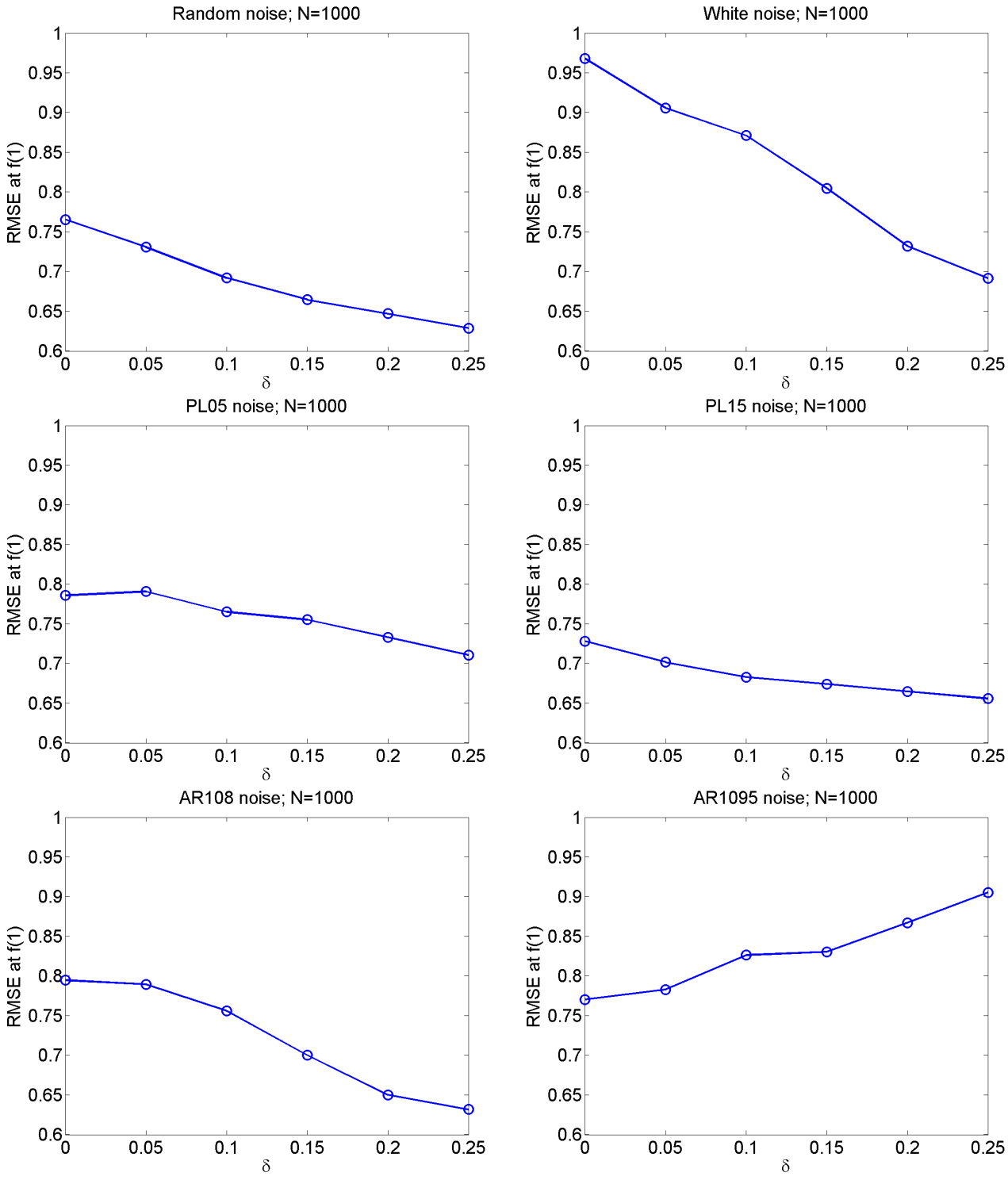

Figure 2.6: Same as Figure 2.5, but data length is 1000.

2.3.2 Parametric model

The fitting procedure of the parametric model is described as follows. Similar to the non-parametric model, five unknown parameters in the parametric model are solved by genetic algorithm with the searching range of $r1$, $r2$, $r3$ from 0 to 1, ν from -2.5 to 0, and ρ from 0 to 1. By solving the normal equation,

$$\frac{\mathrm{d}l}{\mathrm{d}S_0} = 0$$

we can obtain

$$S_0 = 0.5 * \sum_k w(k) \left\{ \frac{\hat{X}_k^2[C_k^{\hat{Y}} S1] + \hat{Y}_k^2[C_k^{\hat{X}} S1] - 2\hat{X}_k\hat{Y}_k[C_k^{\hat{X}\hat{Y}} S1]}{[C_k^{\hat{X}} S][C_k^{\hat{Y}} S] - [C_k^{\hat{X}\hat{Y}} S]^2} \right\} \Big/ \sum_k w(k).$$

where $S1 = r1 * S_w + r2 * S_{pl}(\nu) + r3 * S_{ar1}(\rho)$, $w(k)$ is a weight function described below. To be consistent with the nonparametric model, spectrum obtained by fitting parametric model is constrained by the upper and lower boundary of periodogram.

2.3.3 Weighted fitting

As low frequency bands are most critical, the merit function in 2.2.2.2 is multiplied by a weight function defined by

$$w(k) = ln(\frac{k+1}{k})$$

where k is frequency index. The weight function is designed to give more weight to low frequency band and less weight to high frequency band. This weight function gives approximately equal weight to each log-frequency bin evenly split. The merit function to be minimized for spectrum estimation follows

$$l = \sum_k w(k) \left\{ ln([C_k^{\hat{X}} S][C_k^{\hat{Y}} S] - [C_k^{\hat{X}\hat{Y}} S]^2) + \frac{\hat{X}_k^2[C_k^{\hat{Y}} S] + \hat{Y}_k^2[C_k^{\hat{X}} S] - 2\hat{X}_k\hat{Y}_k[C_k^{\hat{X}\hat{Y}} S]}{[C_k^{\hat{X}} S][C_k^{\hat{Y}} S] - [C_k^{\hat{X}\hat{Y}} S]^2} \right\}. \tag{2.3}$$

The impact of weighting on spectrum fitting is illustrated in a number of simulations. Realizations of the six types of noise are generated, and spectrum is estimated by minimizing merit function 2.1 and 2.3 respectively with both parametric and nonparametric model. Weighting has more influence on the parametric model for all types of noise. Figure 2.7 shows error comparison for the case of AR1095 noise, demonstrating smaller error at low frequencies and higher error at high frequencies when weighted merit function 2.3 is used. The performance of the parametric model changes because more weights are put at low frequencies and the parametric model is likely sensitive to weight changes. Because the noise energy is larger at low frequencies, the low frequencies are more important and are the focus of this study. So we still prefer the weighted fitting of spectrum that gives smaller error at low frequencies even though higher errors are found at high frequencies in some noise cases. The error of fitted spectrum changes less than 0.1 at all the frequencies for the nonparametric model. The scenarios that data smoothing or regression is involved are also investigated. Regression models are listed in table 2.2 in the next section. Figure 2.8 and 2.9 shows similar error reduction at low frequency part except the first frequency for the parametric model when either smoothing or regression model is used for data processing. When both smoothing and regression are applied to time series, the nonparametric model with imposed weight has smaller error at low frequencies than the fitting without weighting (Figure 2.10). The large spikes in Figure 2.8 and 2.10 are related to the average smoothing because the average smoothing causes spectrum wiggles at some high frequencies but the modeled spectrum is monotonic. Since our focus is on the low frequencies in this study, the spectrum estimation in the following sections is based on minimizing the weighted merit function 2.3.

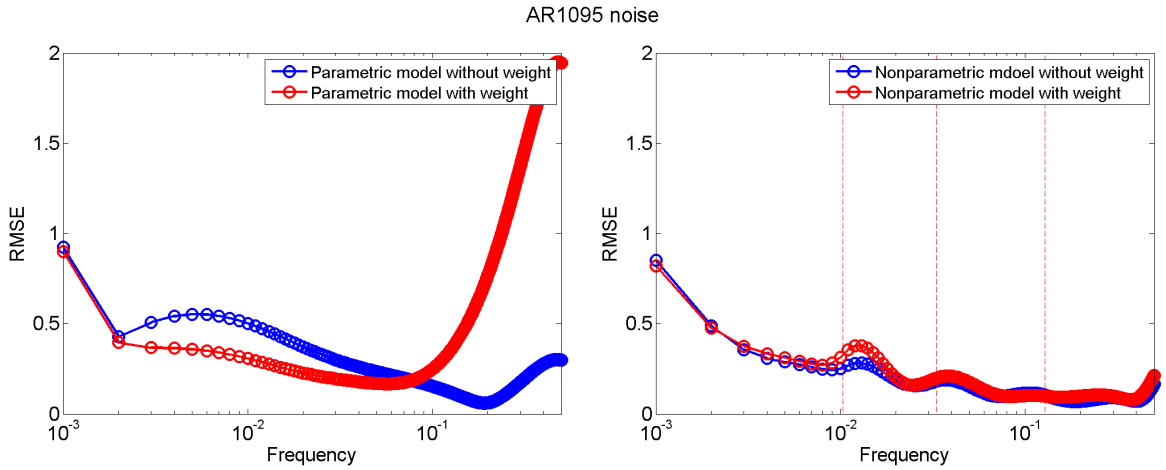

Figure 2.7: RMSE of fitted spectrum using merit function without (Blue) and with (Red) weight for parametric and nonparametric model. Dashed red line denotes knot position.

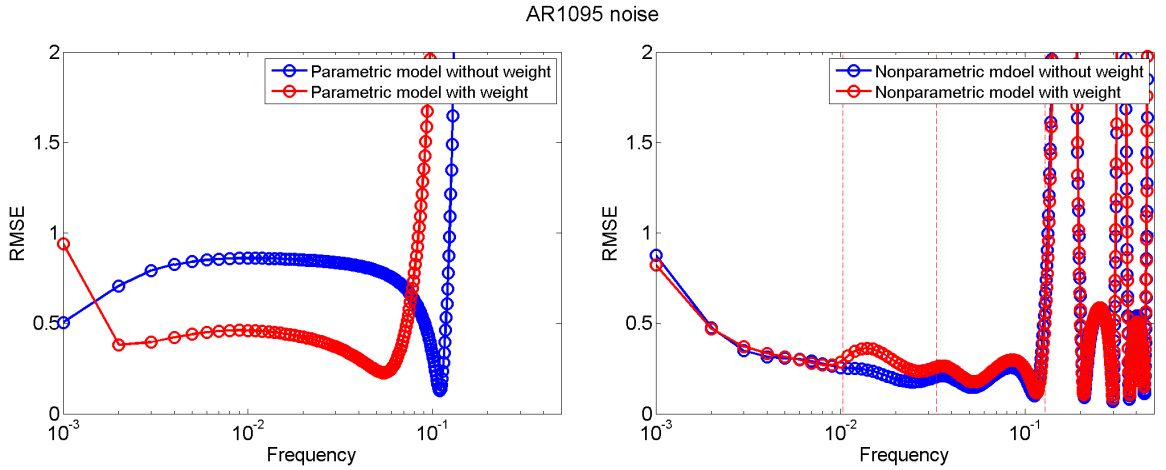

Figure 2.8: Same as Figure 2.7, but time series is smoothed with 7-point moving average.

2.3.4 Simulation tests of spectrum models

The new nonparametric model is going to be tested and compared with the parametric model by means of Monte Carlo simulations. Both parametric and nonparametric models are fitted to the Fourier coefficients of time series in cases without and with regression.

2.3.4.1 Cases without regression

If no regression model is involved, $C^{\hat{X}}$, $C^{\hat{Y}}$ are 0.5 times identity matrix, and $C^{\hat{X}\hat{Y}}$ is zero matrix in the merit function 2.3, which is equivalent to that described in section 2.2.2.1.

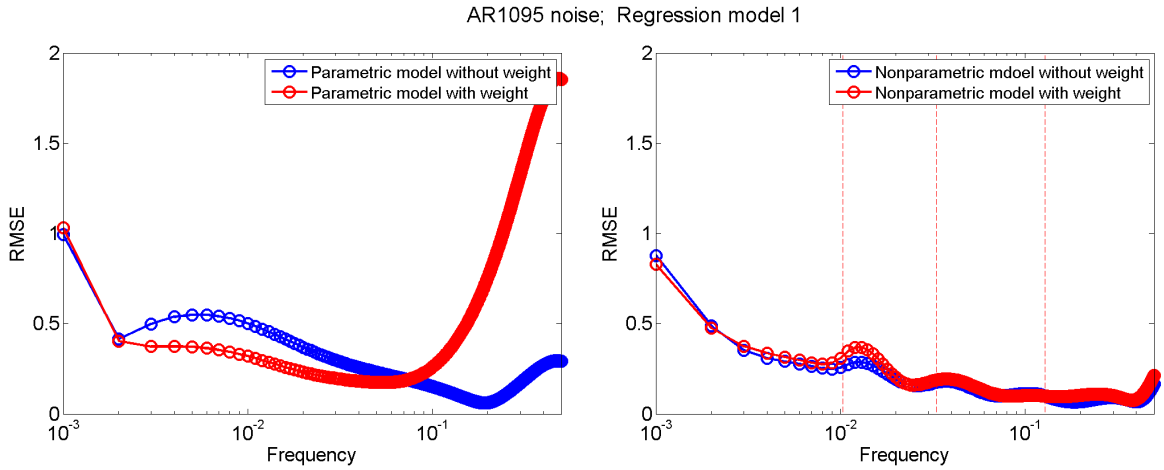

Figure 2.9: Same as Figure 2.7, but spectrum is estimated from residual of linear trend model.

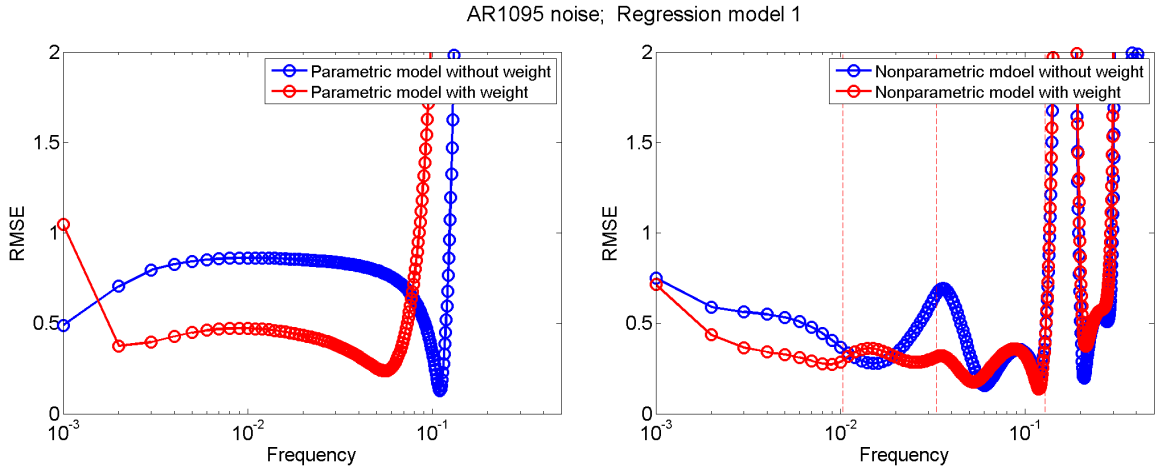

Figure 2.10: Same as Figure 2.7, but time series is smoothed with 7-point moving average and spectrum is estimated from residual of linear trend model.

Few nonparametric noise models are available, one of which is Ebisuzaki model [60]. The error and mean value of spectrum estimated by the parametric and nonparametric model are exhibited together with those of periodogram used by Ebisuzaki for the six types of noise. Periodogram has error as big as true noise spectrum itself, which is expected from the fact that periodogram follows χ^2_2 distribution.

When no smoothing is applied to data, the nonparametric model exhibits error less than 50% except at the first frequency where error could reach as large as 80%. Error of

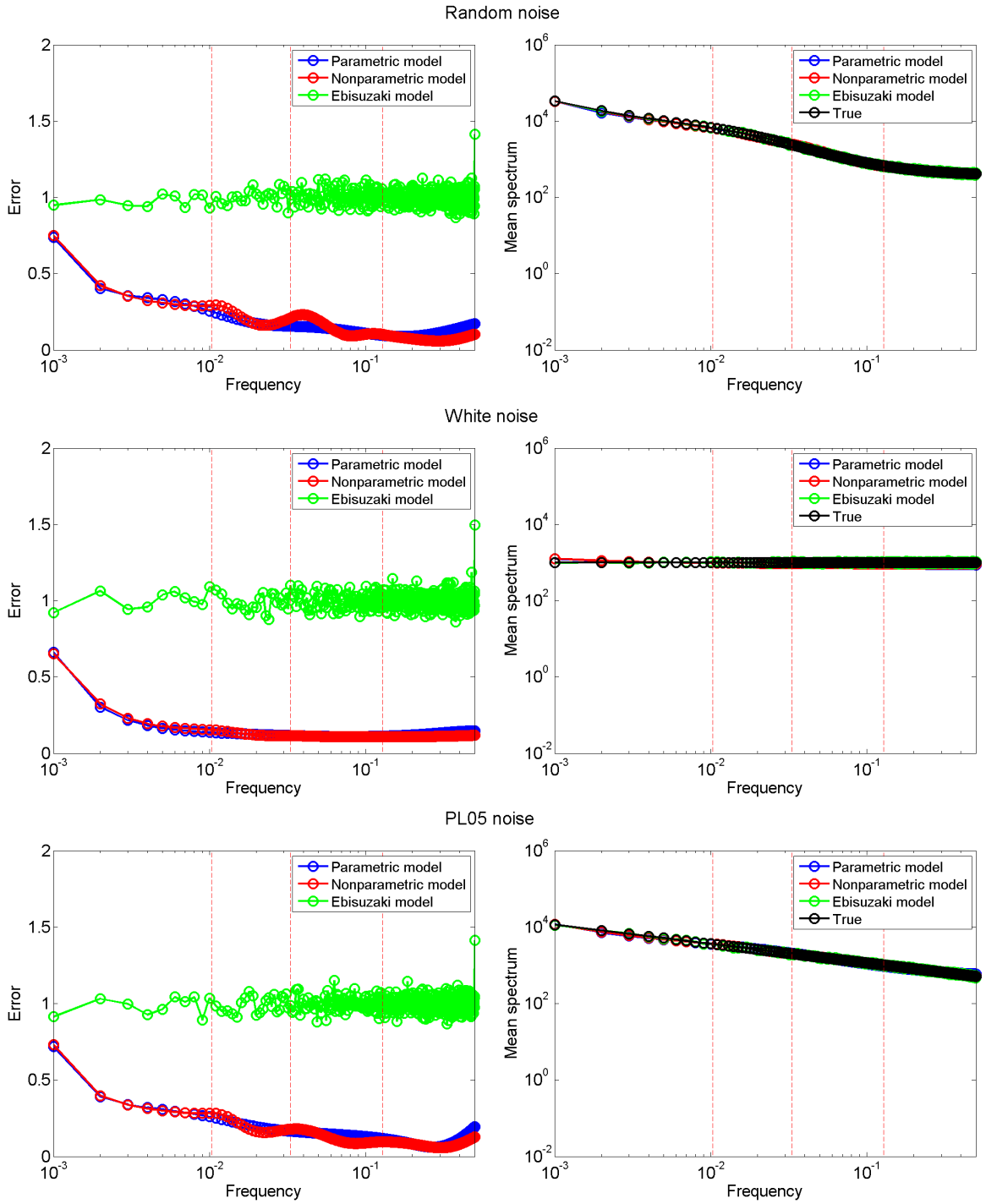

Figure 2.11: RMSE and mean spectrum from parametric (Blue), nonparametric model (Red), and Ebisuzaki model (Green). The mean value of true spectrum is represented by black line. Dashed red line denotes knot position.

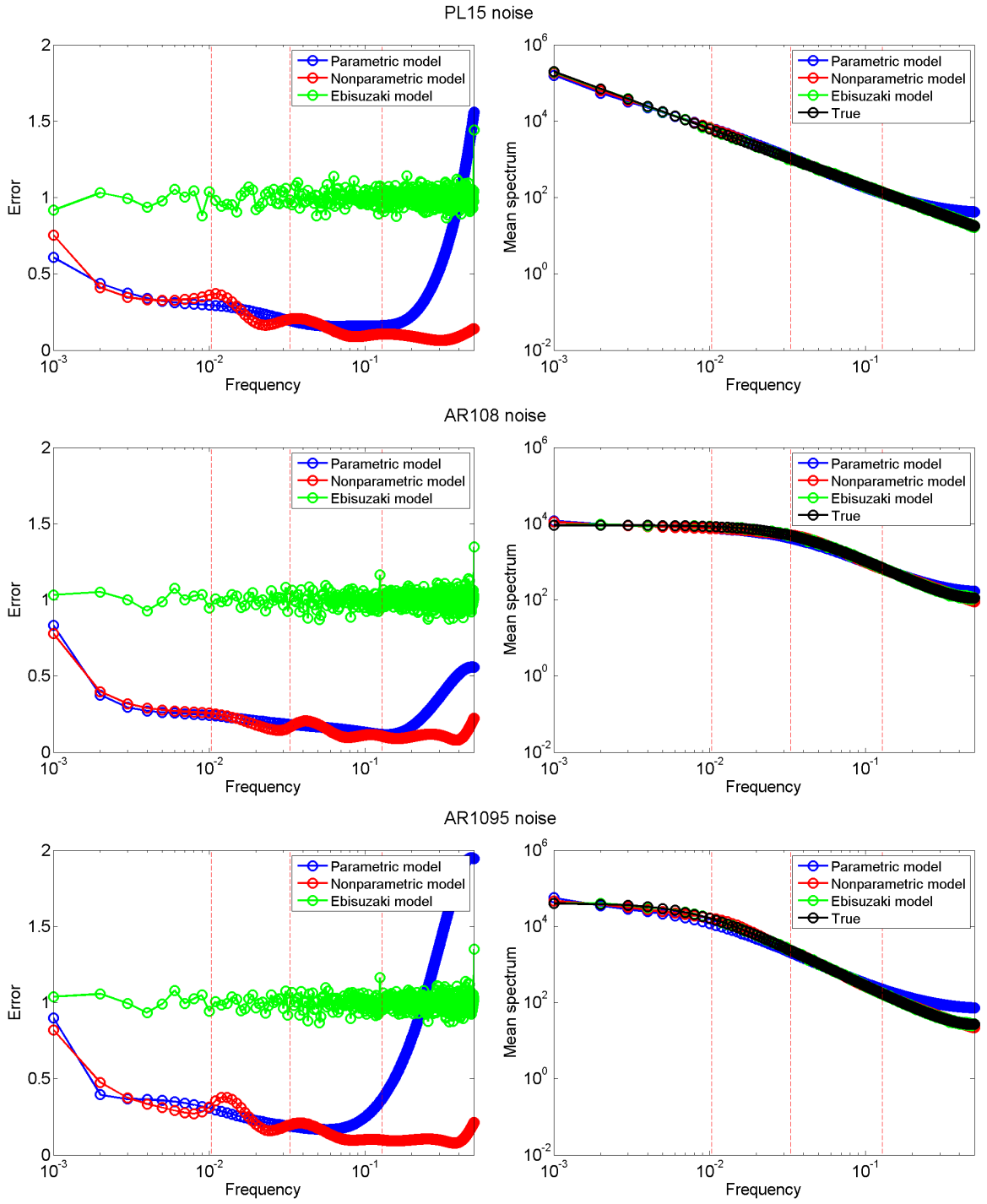

Figure 2.11: Continued.

the nonparametric model is consistent among all types of noise, having a decreasing trend from low to high frequency with wiggles around spline knots (Figure 2.11). The difference between the mean fitted spectrum and the true spectrum is an estimate of the bias error. The parametric model has comparable performance as the nonparametric model at the low frequency band and provides a level of model performance that the nonparametric model can achieve at best. Nevertheless, the parametric model is more sensitive to the weighting function of merit function in that, spectrum fitting at high frequencies is greatly affected by the merit function value at low frequencies, and vice versa. Large error and bias appear at high frequencies in cases of extremely red noise such as PL15 and AR1095. This experiment indicates that, at low frequencies, the nonparametric model is as good as the parametric model from which time series of noise are drawn, and have better performance for some types of noise at high frequencies in the situation when less weight is assigned to high frequencies.

When smoothing is used in data processing, spectrum characteristics are modified, with reducing variance at high frequencies. The Ebisuzaki model still has a uniform error of approximately 100% at all frequencies. As the spectrum response function of the 7-point smoothing fluctuates at high frequencies and is close to zero at some frequencies, the non-parametric and parametric models that are monotonic gives large error at frequencies larger than about 0.1 (Figure 2.12). Since the low frequency part is most critical for statistical analysis and is the focus of this study, the error at high frequencies is not regarded as a serious concern. In this experiment, our attention is on the relatively low frequencies smaller than around 0.1. Because the shape of spectrum is modified by smoothing, error of the parametric model gets larger than those in cases without data smoothing. In contrast, the nonparametric model can deal with shape change of spectrum with a performance as good as that in cases without data smoothing and have smaller error than parametric model in many frequencies, for example, between the second and third knot. This experiment shows

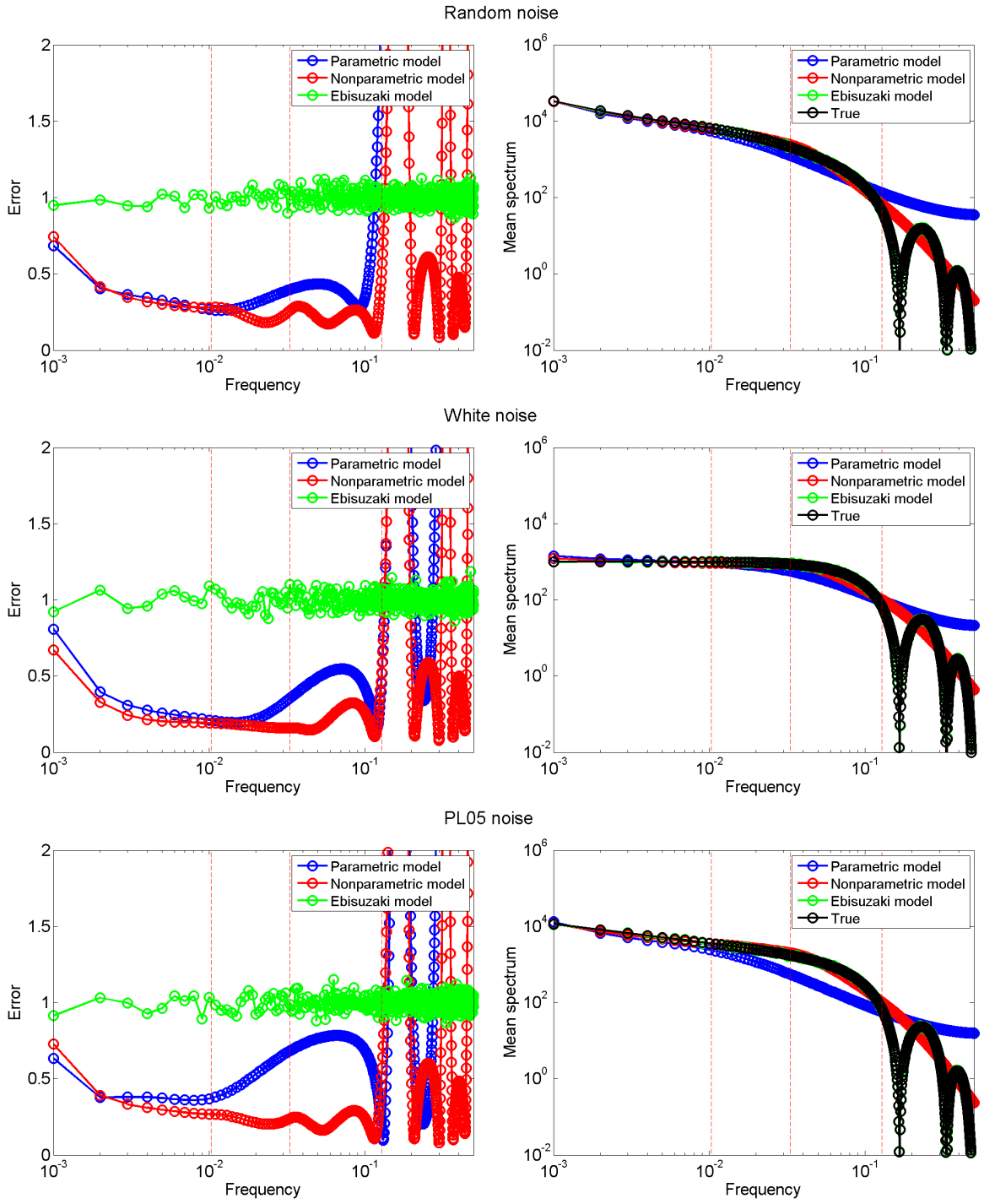

Figure 2.12: Same as Figure 2.11, but time series is smoothed with 7-point moving average.

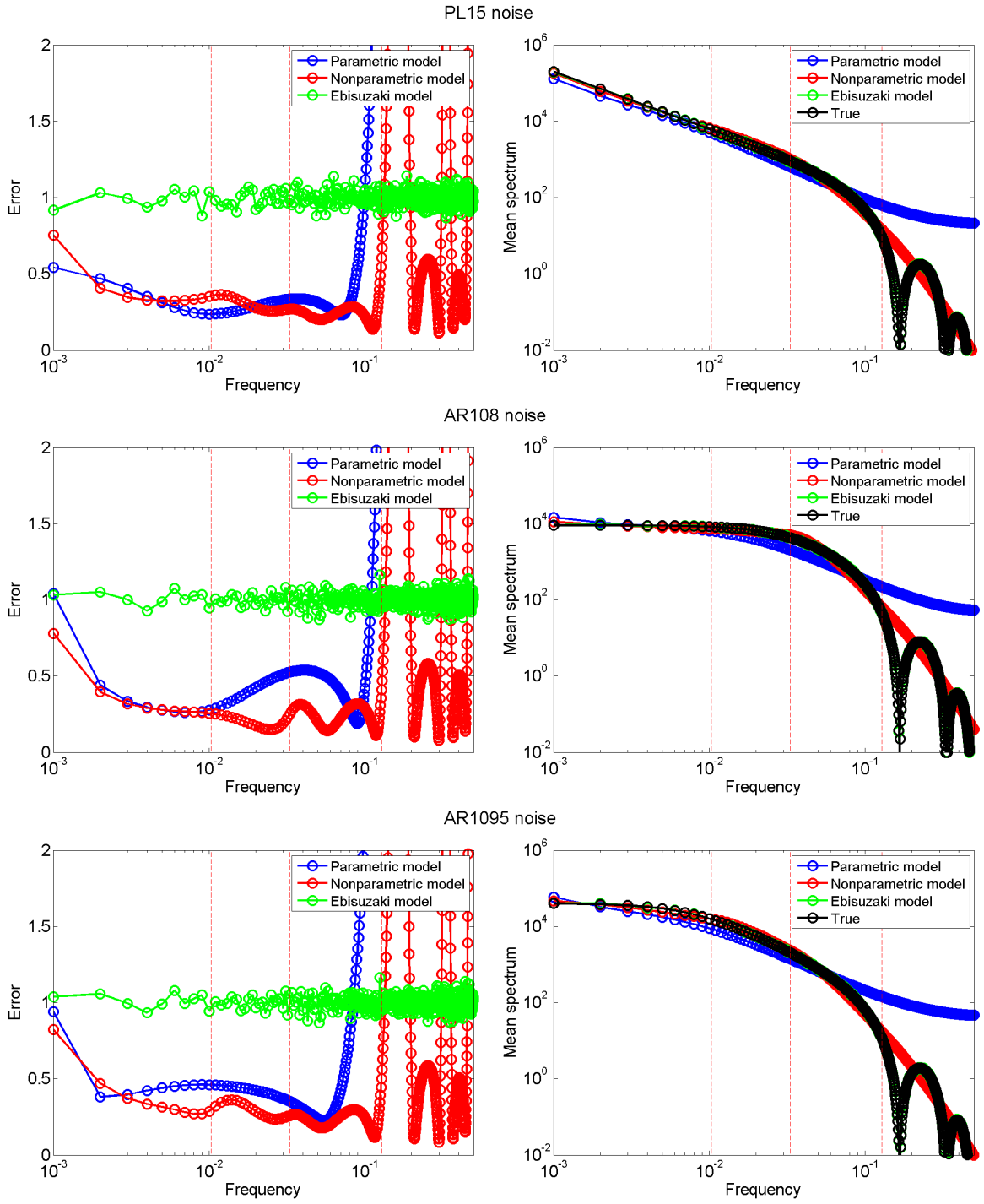

Figure 2.12: Continued.

the advantage of nonparametric model against the parametric model in the ability of flexibly adjusting spectrum shape in a frequency bin without greatly affecting fitting in other bins.

2.3.4.2 Cases with regression

In experiments with regression, two regression models listed in Table 2.2 are fitted to noise realizations. The nonparametric and parametric model are fitted to Fourier coefficients of residual of regression model.

Table 2.2: Two regression models for the test

Model 1	$y = a + bt$
Model 2	$y = a + bt + ct^2$

Residual periodogram used in Ebisuzaki model shows reduced energy at the first frequency (Figure 2.13, 2.14), which is the overfitting by regression model. Residual periodogram error at the first few frequencies is smaller than 1 in all cases with regression, confirming the change of periodogram distribution. The new noise models taking into account the change of periodogram distribution can recover the lost energy back, although it gives rise to larger error at the first frequency that can reach more than 100%. Without data smoothing, the nonparametric model is as good as the parametric model at the low frequency part. When data smoothing is involved, the nonparametric model outperforms parametric model for most types of noise with the evidence of smaller RMSE and better match between fitted and true spectrum at some low frequencies(Figure 2.15; 2.16).

Noise spectrum plays an important role in statistical analysis, for instance, in estimating uncertainties of regression coefficients. One traditional way of calculating variance of regression coefficients is through Monte Carlo simulations, specifically, by fitting regression model to time series that is generated based on noise spectrum and taking variance of these obtained coefficients. A new way was proposed by Doran (2010) [53] who derived a formula relating variance of regression coefficients of orthonormal basis functions to Fourier transform

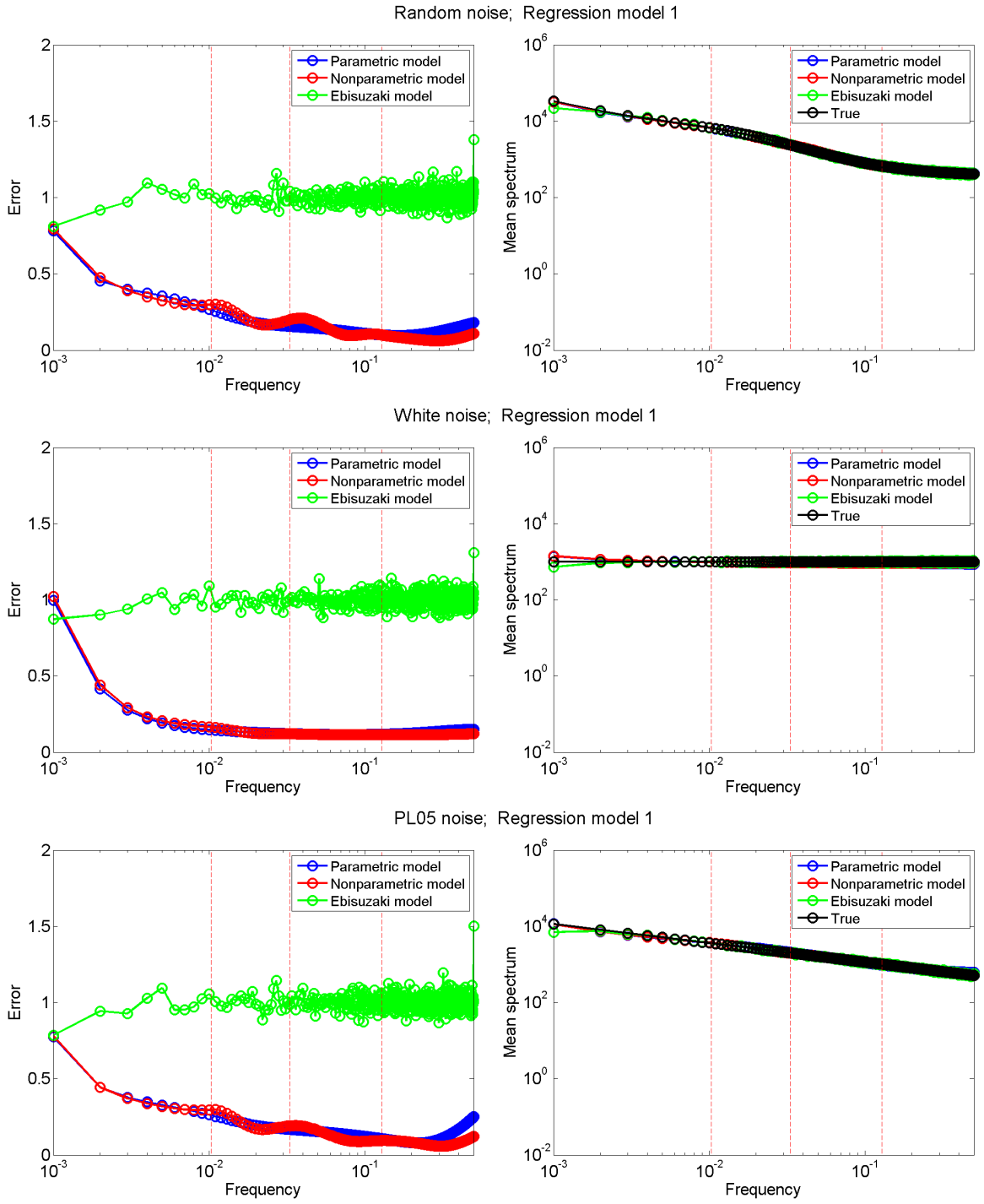

Figure 2.13: Same as Figure 2.11, but regression model 1 is fitted to time series.

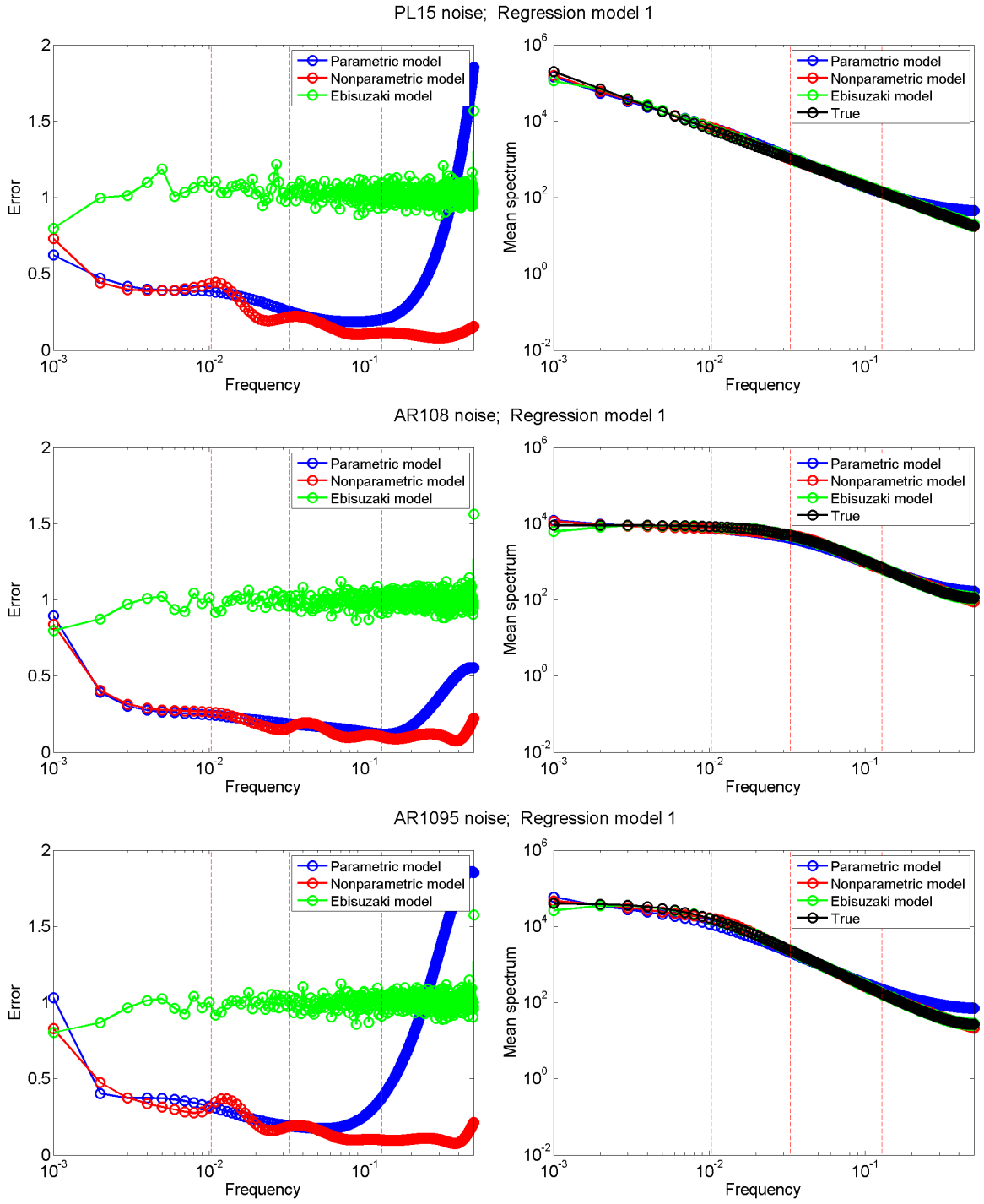

Figure 2.13: Continued.

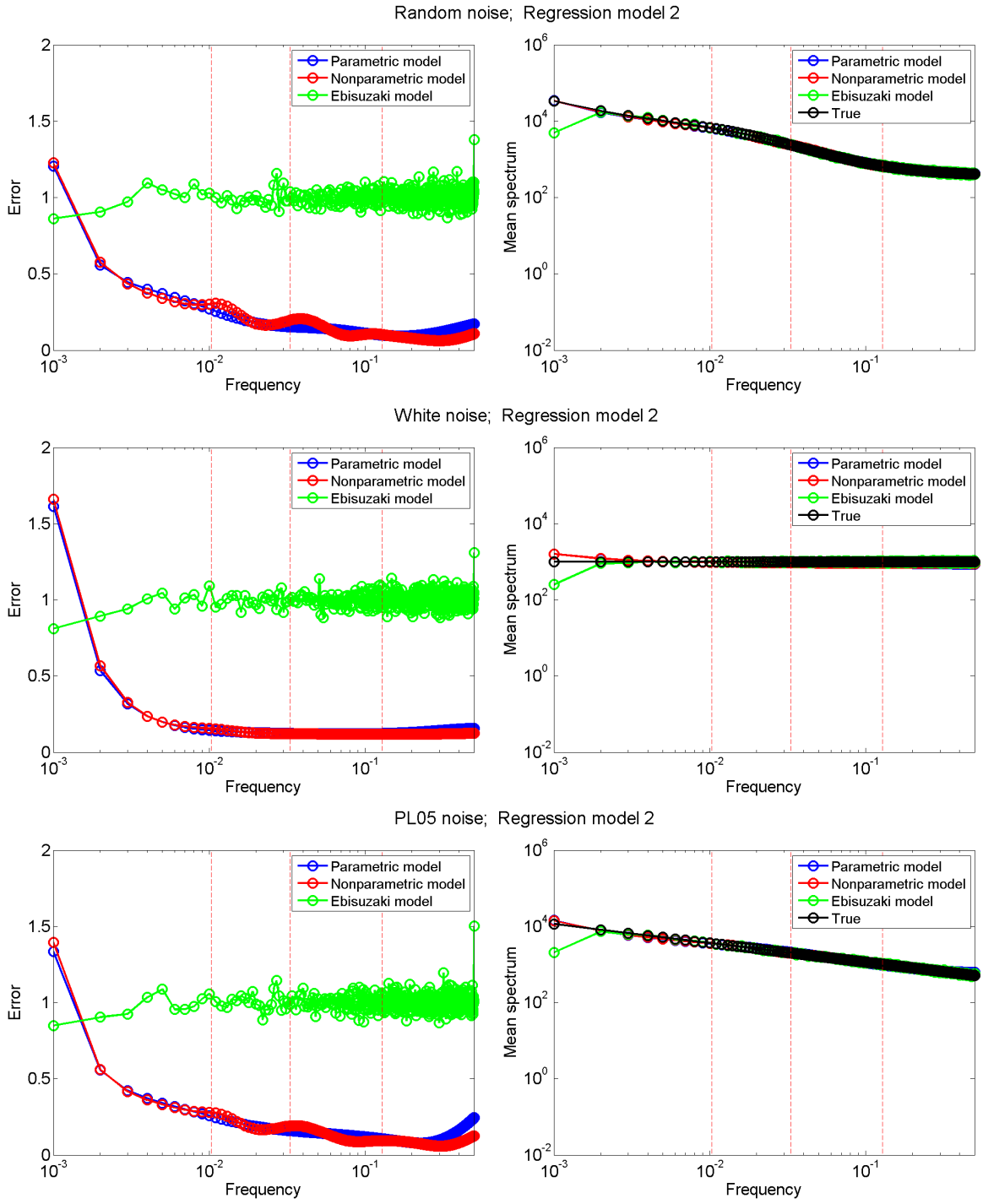

Figure 2.14: Same as Figure 2.11, but regression model 2 is fitted to time series.

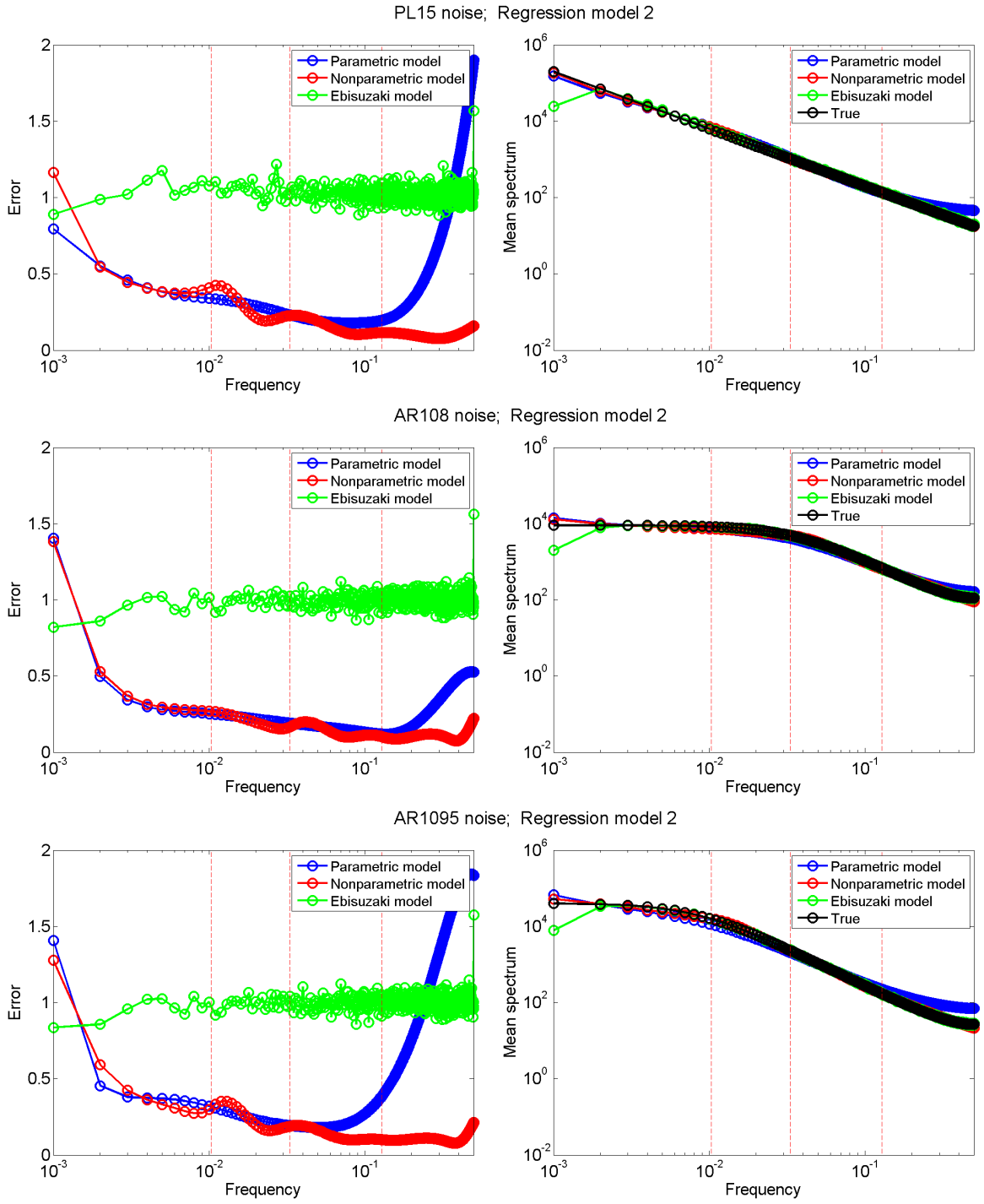

Figure 2.14: Continued.

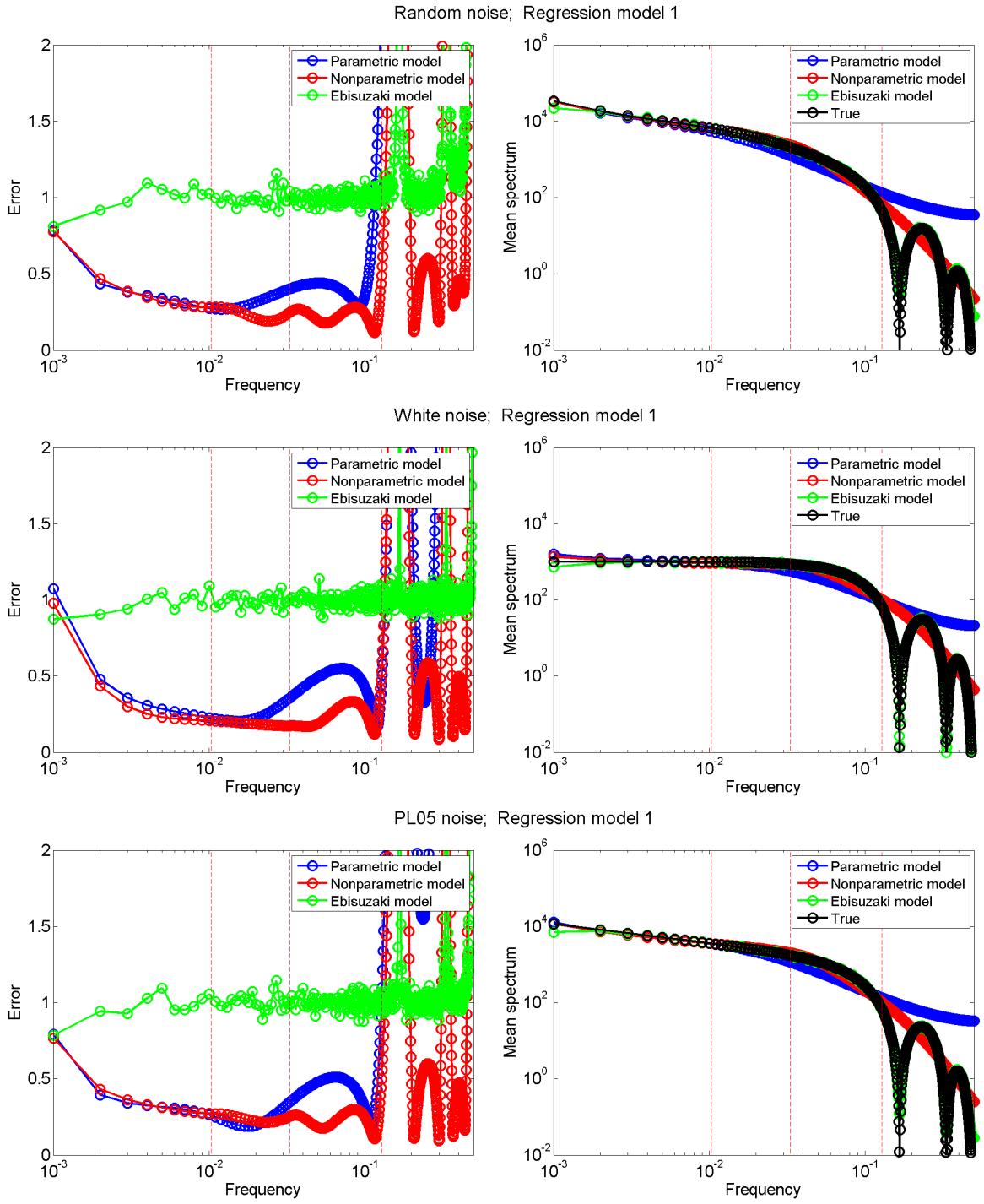

Figure 2.15: Same as Figure 2.11, but regression model 1 is fitted to smoothed time series.

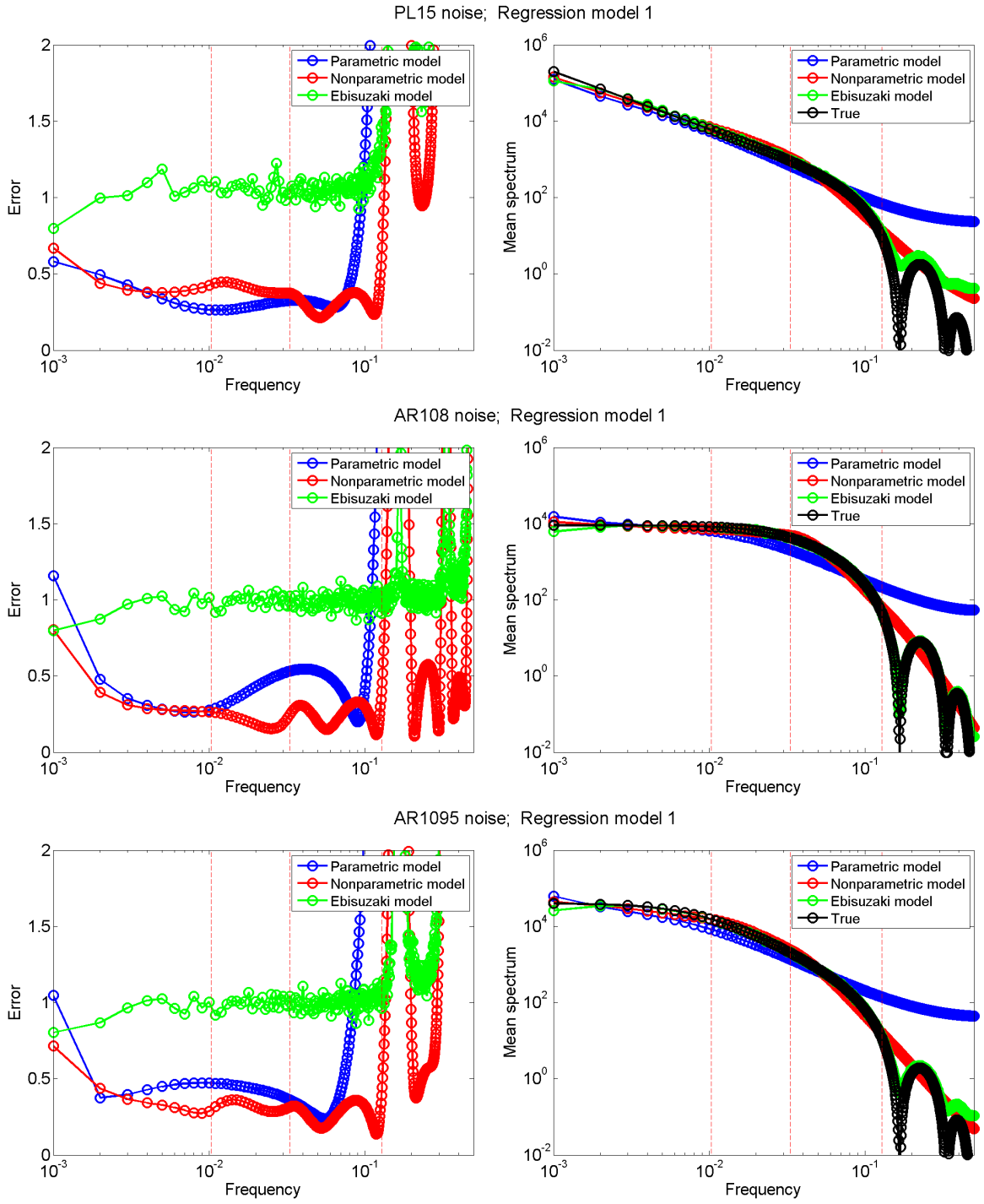

Figure 2.15: Continued.

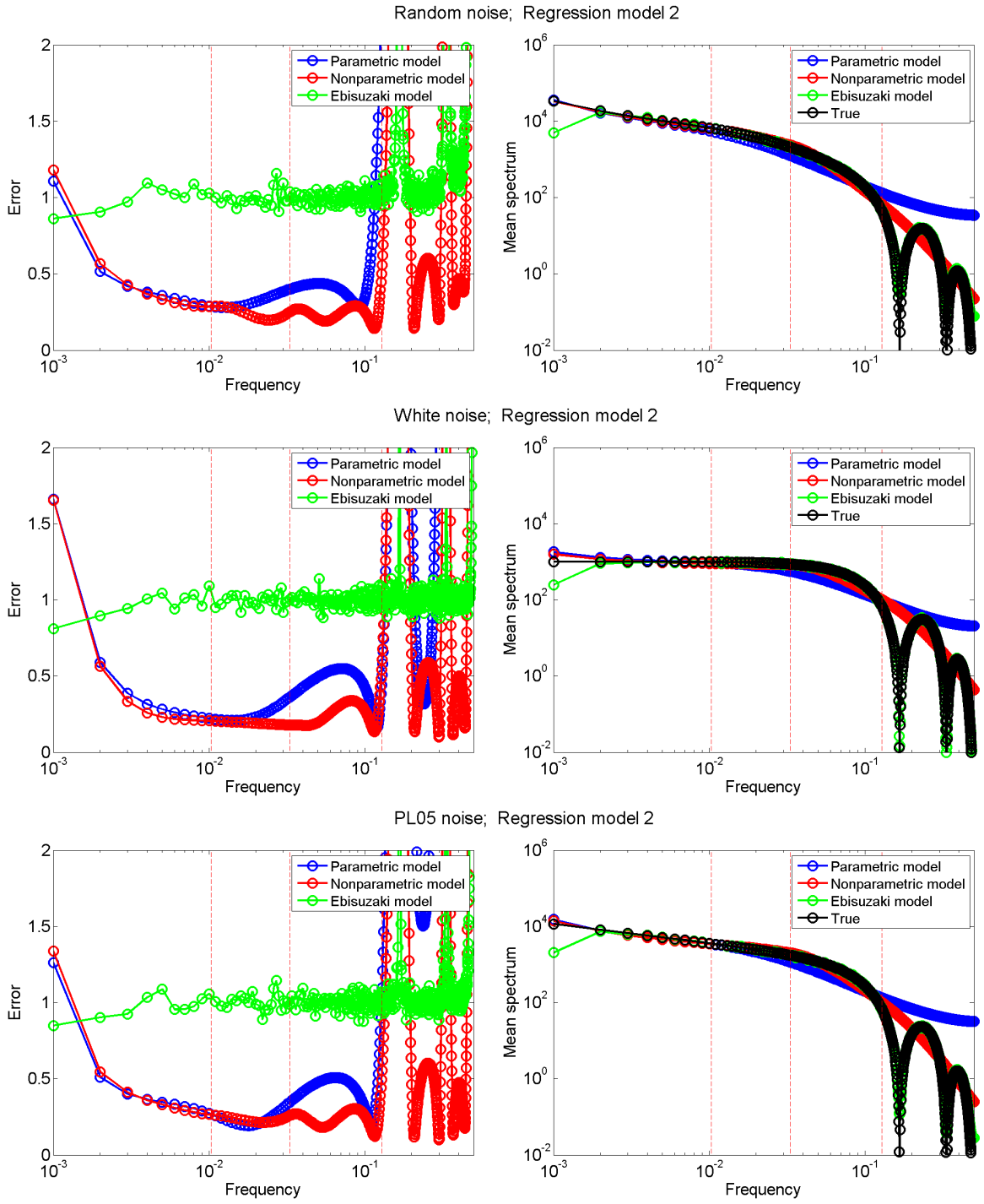

Figure 2.16: Same as Figure 2.11, but regression model 2 is fitted to smoothed time series.

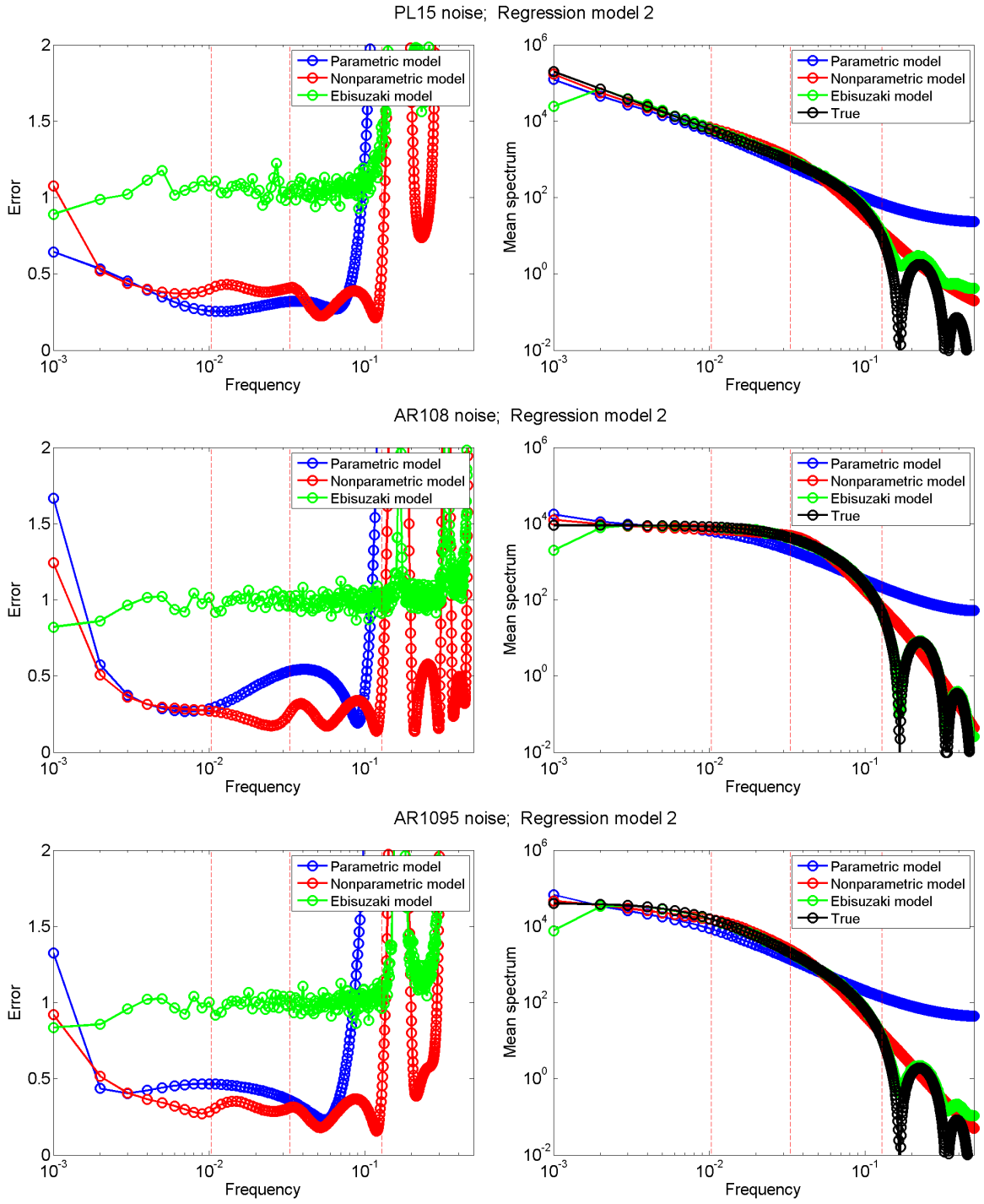

Figure 2.16: Continued.

of basis functions and noise spectrum. Variance of coefficients for regular linear regression is transformed back from that for orthonormal regression model by

$$\begin{aligned} E[(L-\bar{L})(L-\bar{L})^T] &= E[(R^{-1}B - R^{-1}\bar{B})(R^{-1}B - R^{-1}\bar{B})^T] \\ &= E[(R^{-1}(B-\bar{B})(B-\bar{B})(R^{-1})^T] \\ &= R^{-1}E[\beta_i\beta_j](R^{-1})^T \\ &= \frac{1}{N^2}R^{-1}(\sum_k S_k S_k^{ij})(R^{-1})^T \end{aligned}$$

where R is the triangular matrix produced during orthogonalization of regression matrix as shown in section 2.2.2.2; S_k is spectrum at each frequency; S_k^{ij} is the term related to Fourier transform of the orthonormal basis functions; the variance of coefficient is obtained when $i = j$ and the covariance between coefficients is obtained when $i \neq j$.

In this simulation test, coefficient variances of two linear models listed in Table 2.2 are calculated by substituting spectrum estimated with the nonparametric and parametric model into this formula. For the purpose of comparison, two conventional spectrum models, power-law and AR(1) model, are fitted to the residual of regression model, and the coefficient variances are estimated by means of Monte Carlo simulations. Standard deviation of coefficient that is square root of variance is examined in the following analysis. Logarithm of RMSEs of coefficient standard deviation derived from the new and traditional noise models are displayed for the six types of noise in Figure 2.17. Power-law model only has good performance for power-law and white noise, while gives large error for AR(1) noise. In contrast, AR(1) model has good performance for AR(1) and white noise, but gives large error for power-law noise. Performances of power-law and AR(1) noise model depend on true noise type that is not known in most circumstances. The new parametric, nonparametric and Ebisuzaki model show a stable error regardless of noise type. When smoothing is used before fitting a regression model, power-law and AR(1) model have worse performances

for most cases because the noise features have already been modified by smoothing (Figure 2.18). The new noise models and Ebisuzaki model still stay at a relatively stable error level.

Error ratio of nonparametric model to parametric model is close to one, suggesting a comparable performance (Figure 2.19). With data smoothing, nonparametric model is still as good as and even better than parametric model in some cases. Error ratio of nonparametric model to Ebisuzaki model is smaller than 1 for all cases (Figure 2.20), implying that the nonparametric model gives more accurate estimate of coefficient uncertainty owing to smaller error of spectrum at most frequencies and the ability of taking into account the reduced variance by overfitting.

In summary, although the spectrum estimated with the nonparametric model has relatively large error at the first frequency, the nonparametric model shows its advantage over conventional models in better dealing with different noise characteristics and recovering the reduced energy induced by regression's overfitting. This nonparametric model will be applied to distinguish regression models predicting the reconstructed GMSL.

2.4 Distinguishing between regression models used for reconstructed GMSL

GMSL reconstructed from historical tide gauge data has shown a rising sea level since the late 19th century but with a possibly nonuniform rate across this period. A number of regression models have been chosen in previous studies for detecting sea level rising signals, making different conclusions on how sea level changed in the long term (e.g. Church and White, 2011 [1]; Chambers et al., 2012 [40]; Woodworth et al., 2009 [38]). Here, six different models, including a linear trend (Model 1), quadratic trend (Model 2), linear trend plus a harmonic oscillation (Model 3), stepwise trends (Model 4, 5), and exponential trend (Model 6) are explored to investigate the GMSL time series (Table 2.3). In model 3, T is unknown period ranging from 5 to 80 years. In model 4, T1 and T2 are unknown times when sea level trend could change, and are bounded between 1920 and 1940, between 1970 and 2000, respectively. In model 5, three rate changes happen at T1, T2, and T3 that are unknown

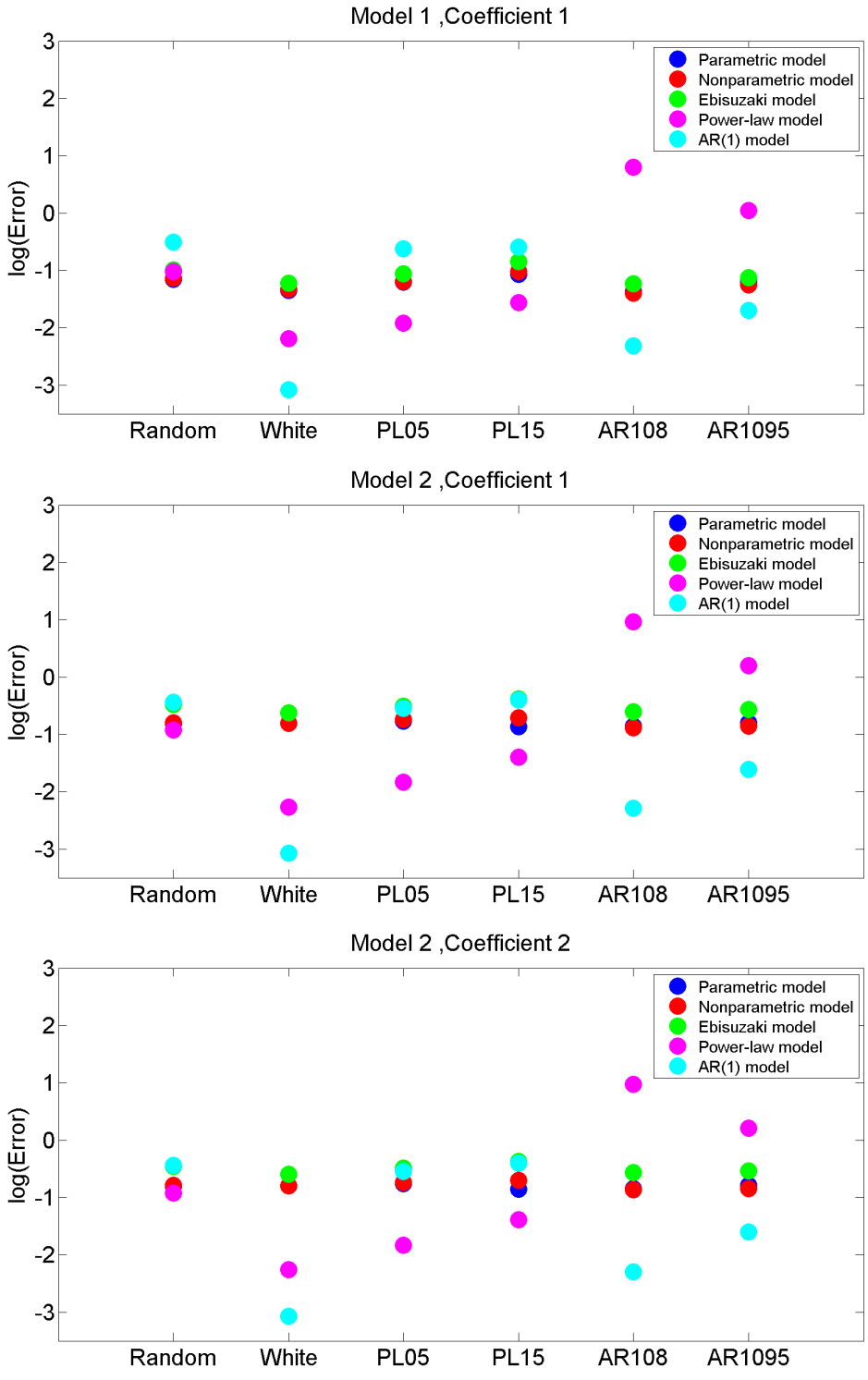

Figure 2.17: Logarithm of RMSE of coefficient standard deviation estimated from five noise spectrum models for six types of noise.

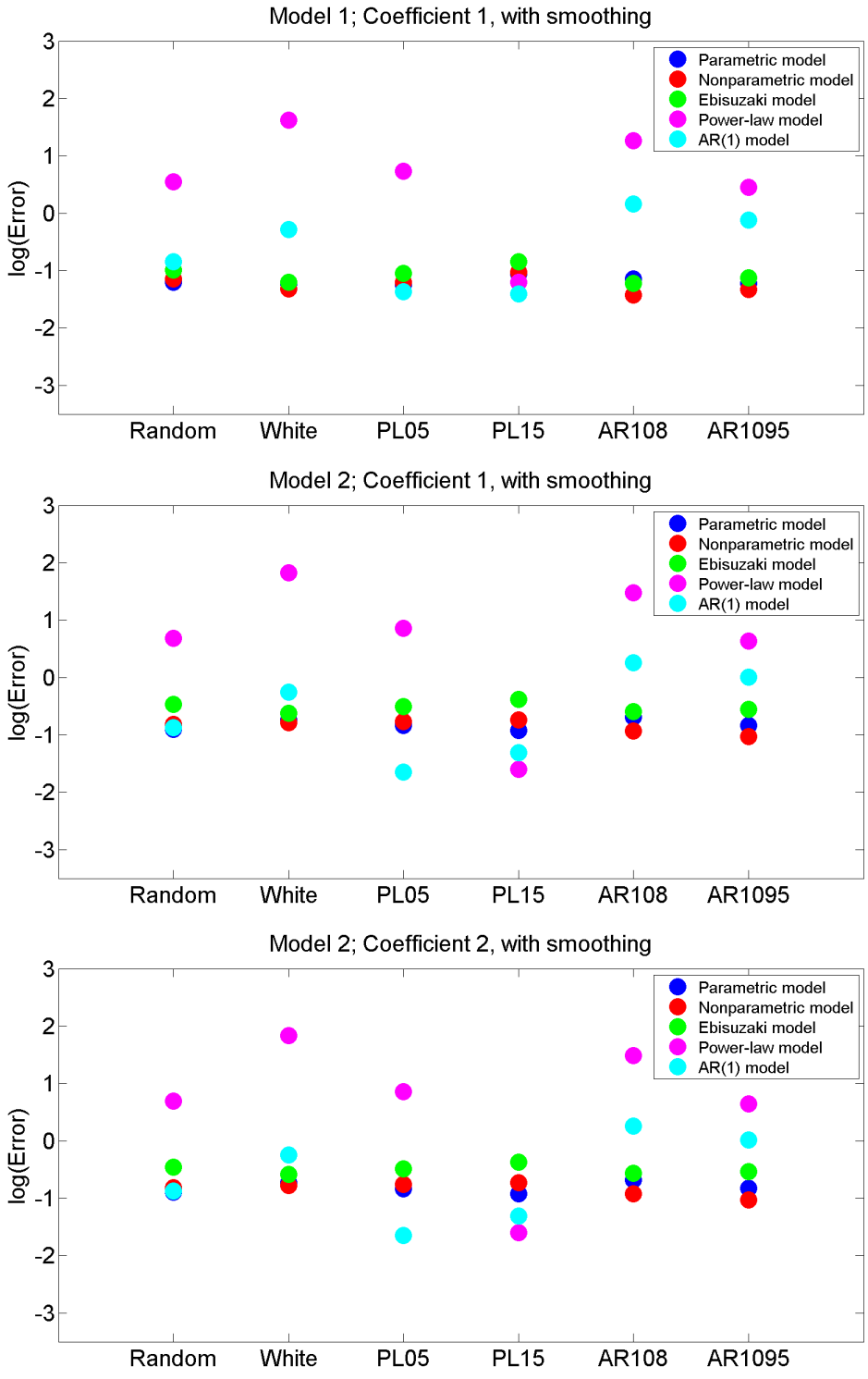

Figure 2.18: Same as Figure 2.17, but time series is smoothed with 7-point moving average.

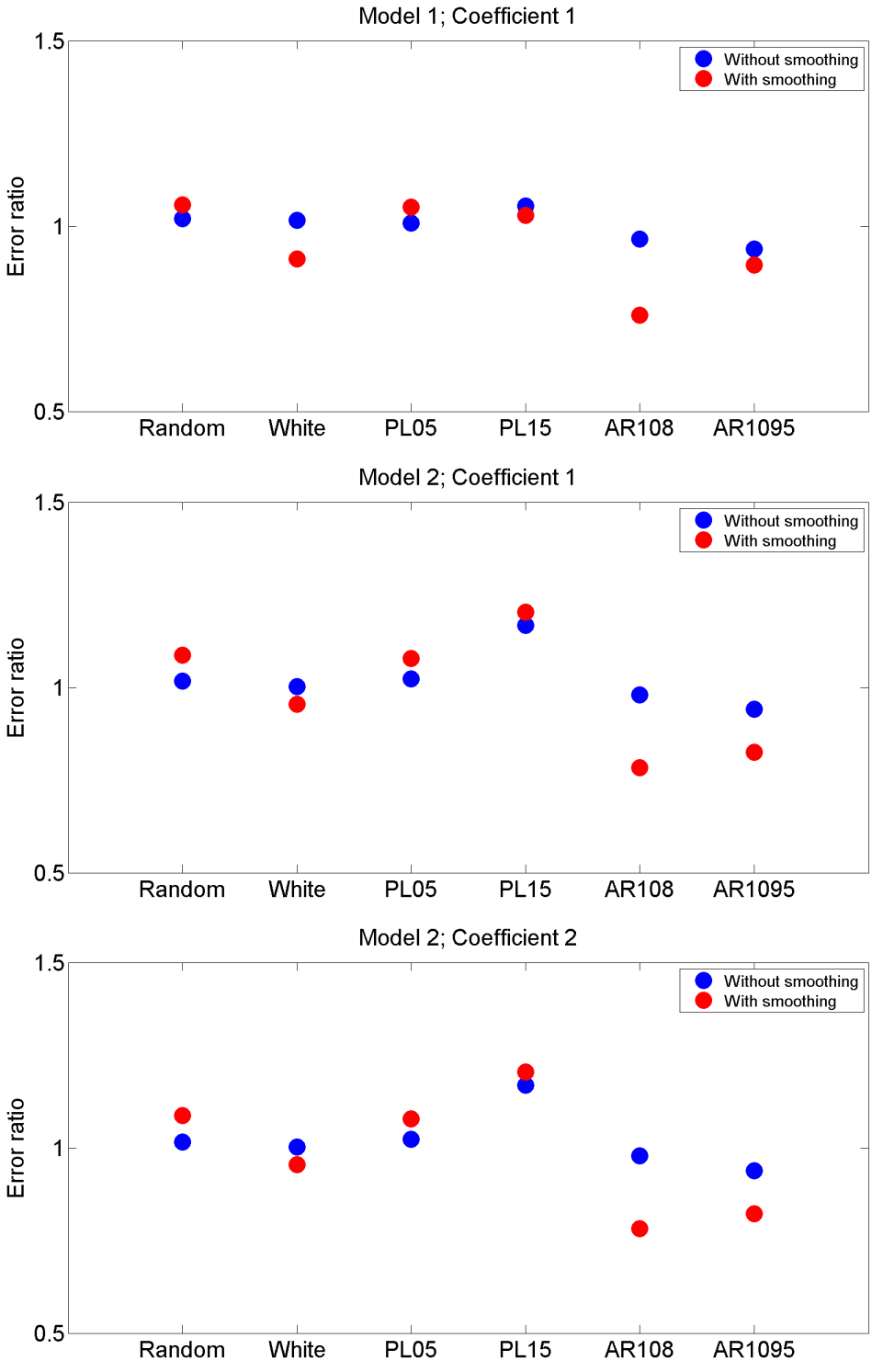

Figure 2.19: RMSE ratio of nonparametric model to parametric model.

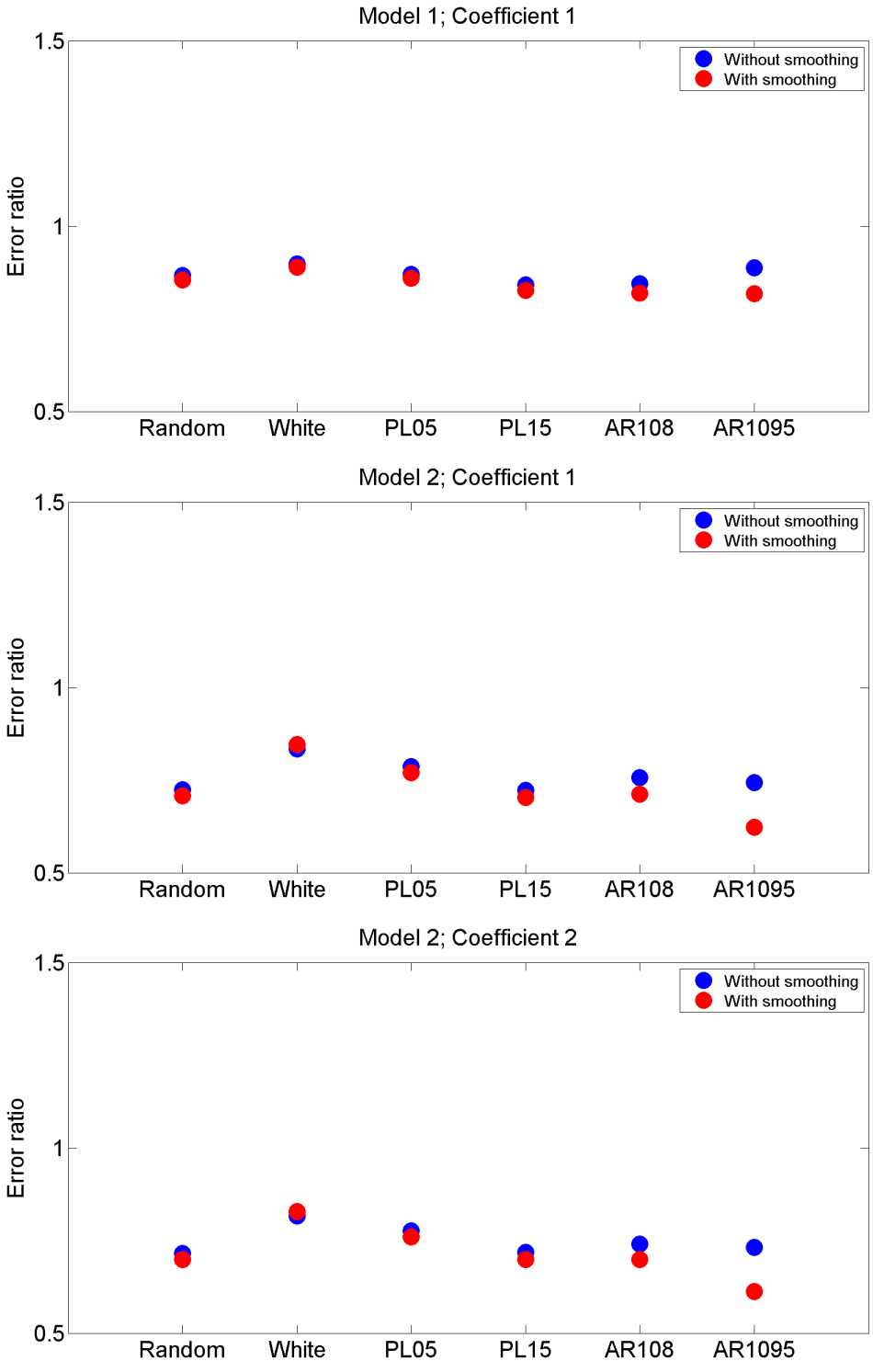

Figure 2.20: RMSE ratio of nonparametric model to Ebisuzaki model.

but between 1920 and 1940, between 1950 and 1970, between 1980 and 2000, respectively. Every temporal segment separated by T1, T2, or T3 in model 4 and 5 is designed to be equal to or larger than 15 years. The six models are fitted to the GMSL reconstructed by Church and White (2011) [1], as shown in Figure 2.21. These models capture the rising trend but differ in how the rising rate changes with time. Model 2 gives an acceleration of 0.012 mm/yr^2; model 3 shows an oscillation with period of 57 years superimposed on a linear trend; In model 4, sea level trend changed from 1.1 mm/yr to 1.7 mm/yr at 1933 and then to 3.9 mm/yr at 1999; model 5 shows an increased rate at 1937, a decreased rate at 1952, and an increased rate at 1998; model 6 demonstrates an acceleration as well. The residual variance from model 1 to 6 is 136.6 mm^2, 66.2 mm^2, 112.1 mm^2, 49.8 mm^2, 48.4 mm^2, and 63.6 mm^2 respectively, showing that model 5 accounts for the most variance of long-term sea level change and is close to model 4, that model 2 is as good as model 6, and that model 1 (linear trend) is the worst among the six models. Different models will have considerably different predictions of future sea level. It is therefore critical to ask whether these model differences are significant. We address this question using the novel noise model that we have developed.

The nonparametric noise model that we have developed in the previous sections has been shown to have advantages over conventional methods. It can therefore serve to provide an accurate estimate of background noise for comparisons of sea level models and to help us identify which model accounts for the most variance. Nevertheless, one caveat of this noise model is that regression models when involved in data processing should be linear. Model 3, 4, 5, and 6 used in our study are, however, nonlinear models. Here, we first estimate regression coefficients, and then make the nonlinear regression model linear by substituting fitted parameters into it, so that noise spectrum can be estimated in cases with either linear or nonlinear regression models. This is essentially a generalization of our noise model from linear to nonlinear regression models.

Noise spectra estimated from the residuals of all six models are displayed in Figure 2.22. Model 1 and 3 show similar spectrum, while model 2, 4, 5 and 6 give similar estimates. Consistent with the smaller residual variances, spectra estimated from the residuals from models 2, 4, 5 and 6 have smaller variances than those derived from the residual of model 1 and 3. The reason is that models 1 and 3 may treat part of the signal as noise, resulting in an overestimation of the true noise.

Table 2.3: Regression models for GMSL

Model 1	$y = a + bt$
Model 2	$y = a + bt + ct^2$
Model 3	$y = a + bt + c\cos\left(\frac{2\pi t}{T}\right) + d\sin\left(\frac{2\pi t}{T}\right)$
Model 4	$y = \begin{cases} a + bt; & t \le T1 \\ a + bt + c(t - T1); & T1 < t < T2 \\ a + bt + c(t - T1) + d(t - T2); & t \ge T2 \end{cases}$
Model 5	$y = \begin{cases} a + bt; & t \le T1 \\ a + bt + c(t - T1); & T1 < t < T2 \\ a + bt + c(t - T1) + d(t - T2); & T2 < t < T3 \\ a + bt + c(t - T1) + d(t - T2) + e(t - T3); & t \ge T3 \end{cases}$
Model 6	$y = y_0 + a\exp(bt)$

A total of 15 model pairs from the six sea level models are compared via Monto Carlo simulations. For any two models being compared, the noise spectrum with the least residual variance of the two models is used to generate noise realizations. Choosing the noise spectrum in this way reduces the potential of underestimating the underlying true signal. Since our noise model can consider the overfitting but not the underestimation of the regression signal, the noise spectrum with the least residual variance should be closer to the true one. The two models in any given pair are fitted to the noise realizations, and then the variance of model difference obtained from each noise realization is computed. Histogram of variances of the model difference obtained by simulations is shown with the observed value (Figure 2.23). Model 1 is significantly different from other models except model 3, suggesting the existence of an acceleration in the long-term GMSL rate. Model 2 is significantly different from all

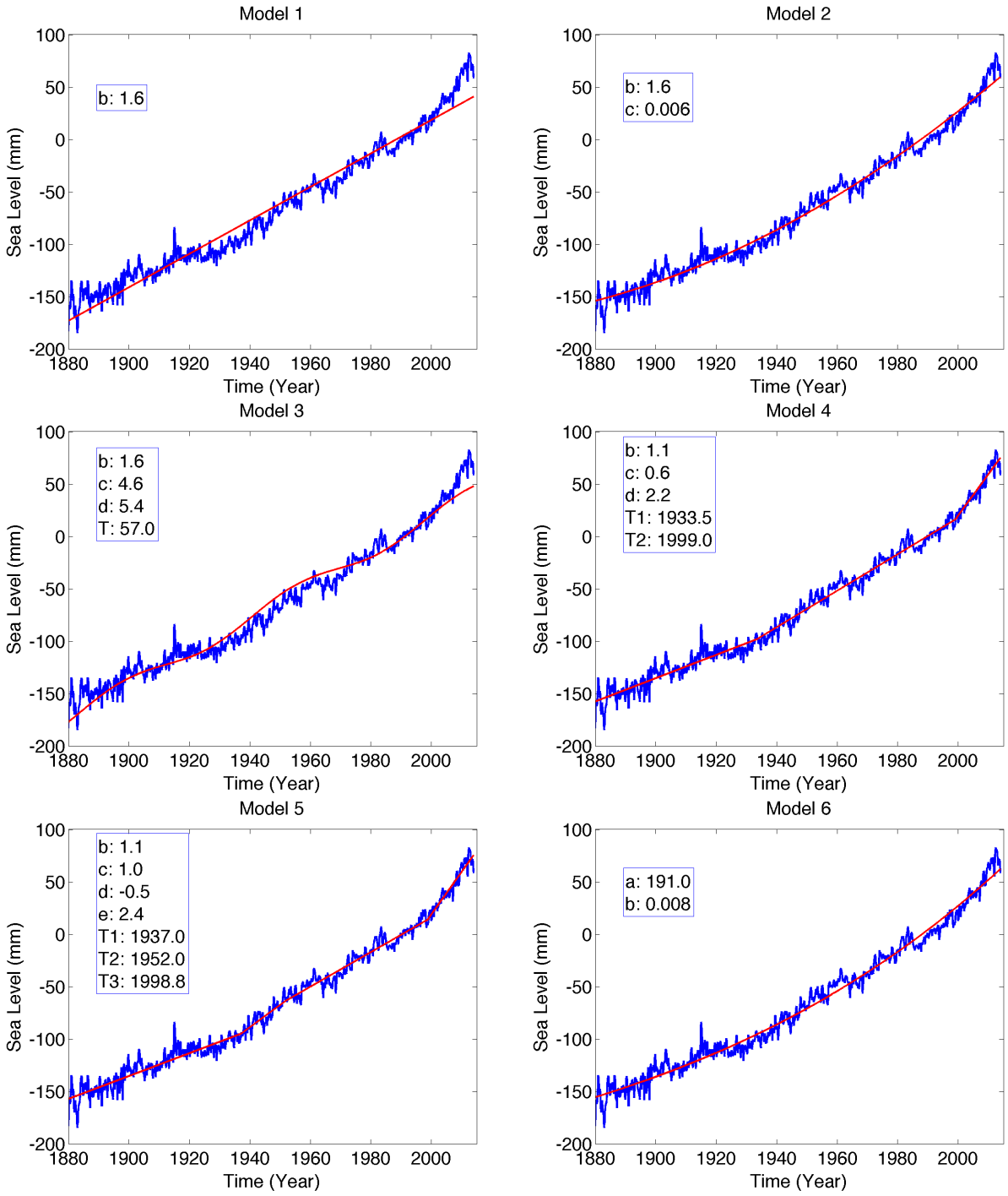

Figure 2.21: Reconstructed GMSL and fitted sea level with six models.

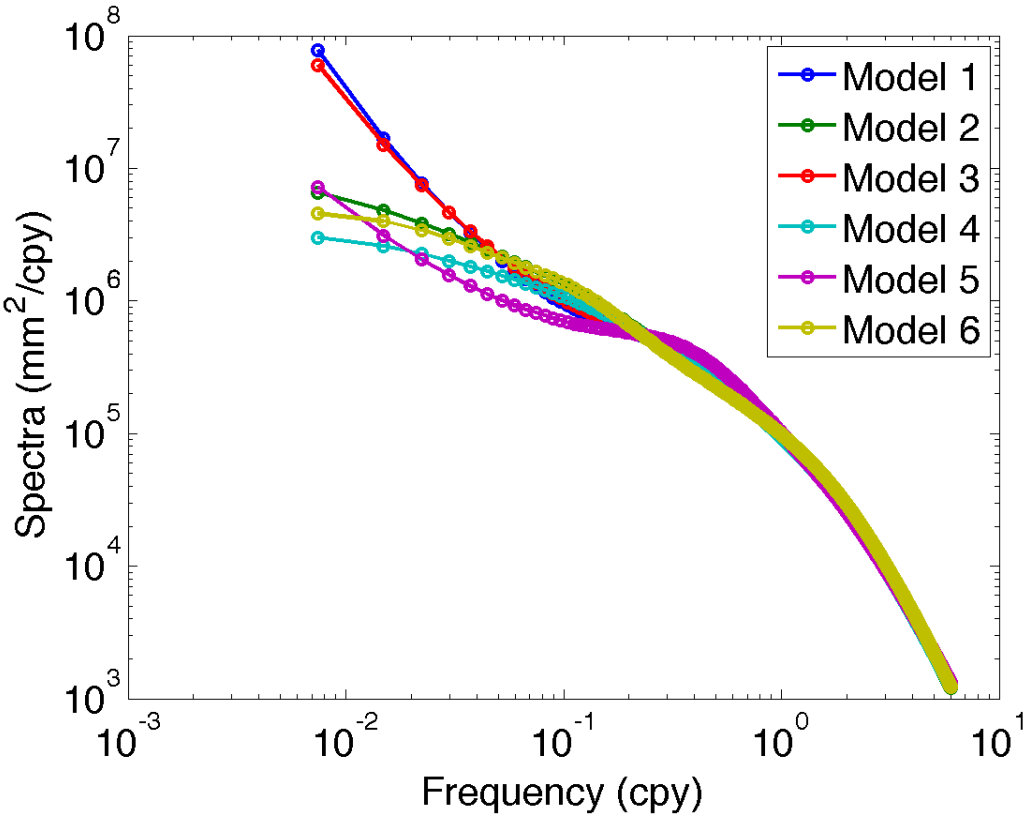

Figure 2.22: Noise spectrum estimated from the residual of six sea level models.

other models except model 6, indicating that we can not distinguish between quadratic and exponential change in the reconstructed GMSL. The quadratic and exponential models account for nearly the same sea level variance but deviate away from each other in the future prediction. Longer time series are needed to distinguish the two models. Model 3 is significantly different from other models except model 1, showing that the reconstructed GMSL may not have a harmonic oscillation. Model 4 with two rate changes is not significantly different from model 5 with three rate changes, but is different from other models. Stepwise change of sea level rising rate can significantly explain more sea level variance than other models. Model 5 and 6 can not be distinguished at the 5% significance level.

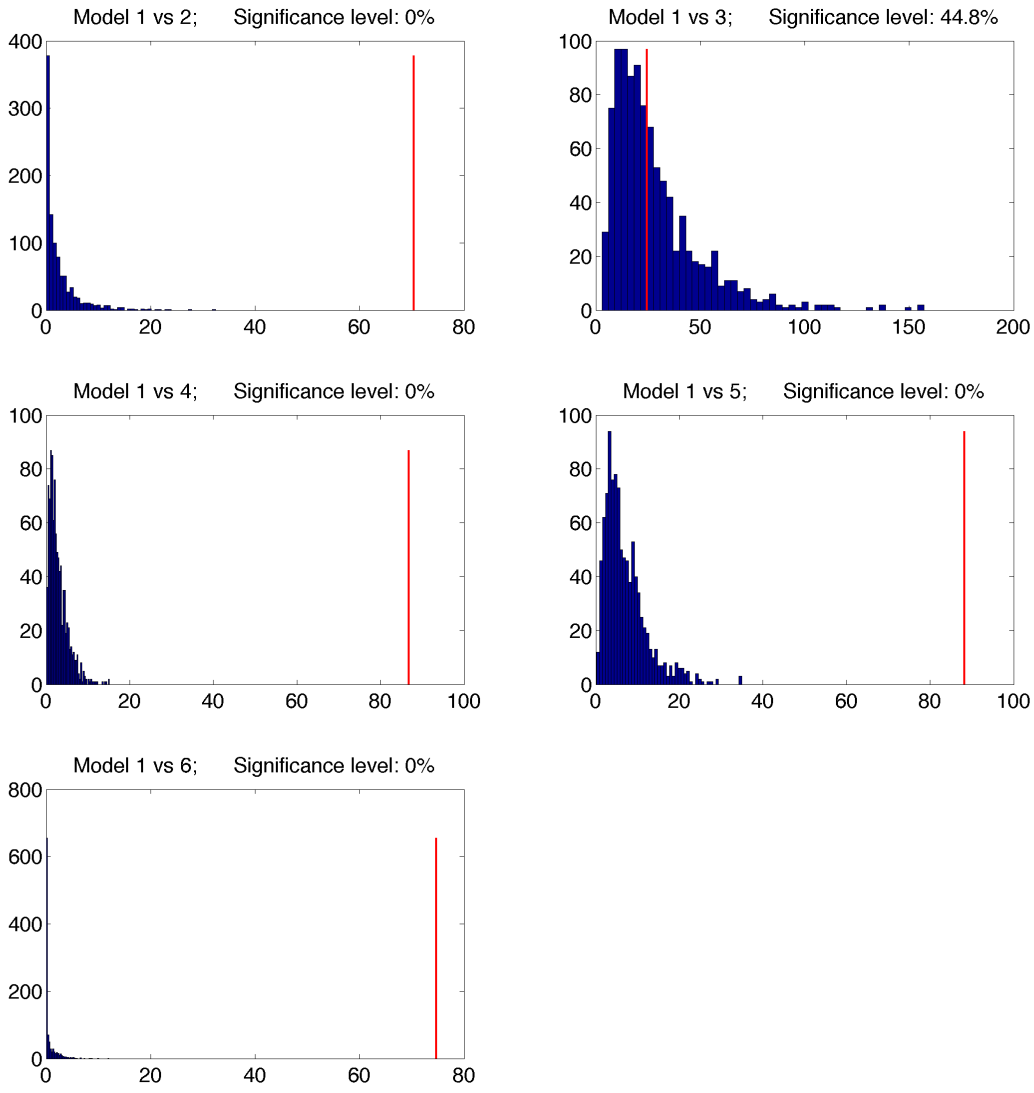

Figure 2.23: Histogram of simulated variances of model difference between every model pair; the observed value is denote by red line.

2.5 Conclusion and Discussion

GMSL has been rising since the late 19th century, owing to increased heat content stored in the ocean and water transfer from glaciers and ice sheets to the ocean. The rising rate is probably not constant through the period with instrumental sea level observation, but

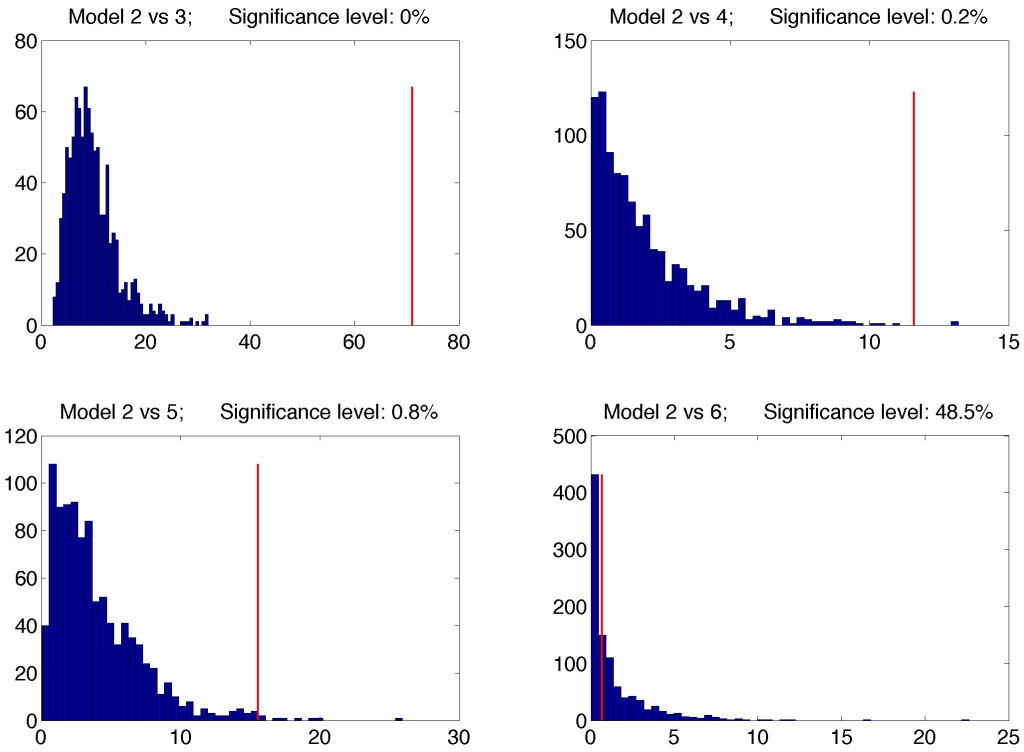

Figure 2.23: Continued.

determining this from data and models is not established. Different models implicate distinct physical processes and would lead to dramatically different predictions of future sea level change. Hence, distinguishing between these different sea level models is necessary, but this depends on an accurate estimation of the background noise.

In most circumstances, noise characteristics are unknown and may be modified by data processes such as regression or smoothing. When no regression model is fitted to time series, the noise periodogram follows a χ^2_2 distribution. When a regression model is involved, we show that the Fourier coefficients of the model residual follow a bivariate normal distribution, which allows us to derive a maximum likelihood estimator for the noise spectrum. A more general form of merit function incorporating the influence of regression model is derived with the noise spectrum being the only unknown parameter. A nonparametric noise model is proposed to estimate the noise spectrum by minimizing the weighted merit function.

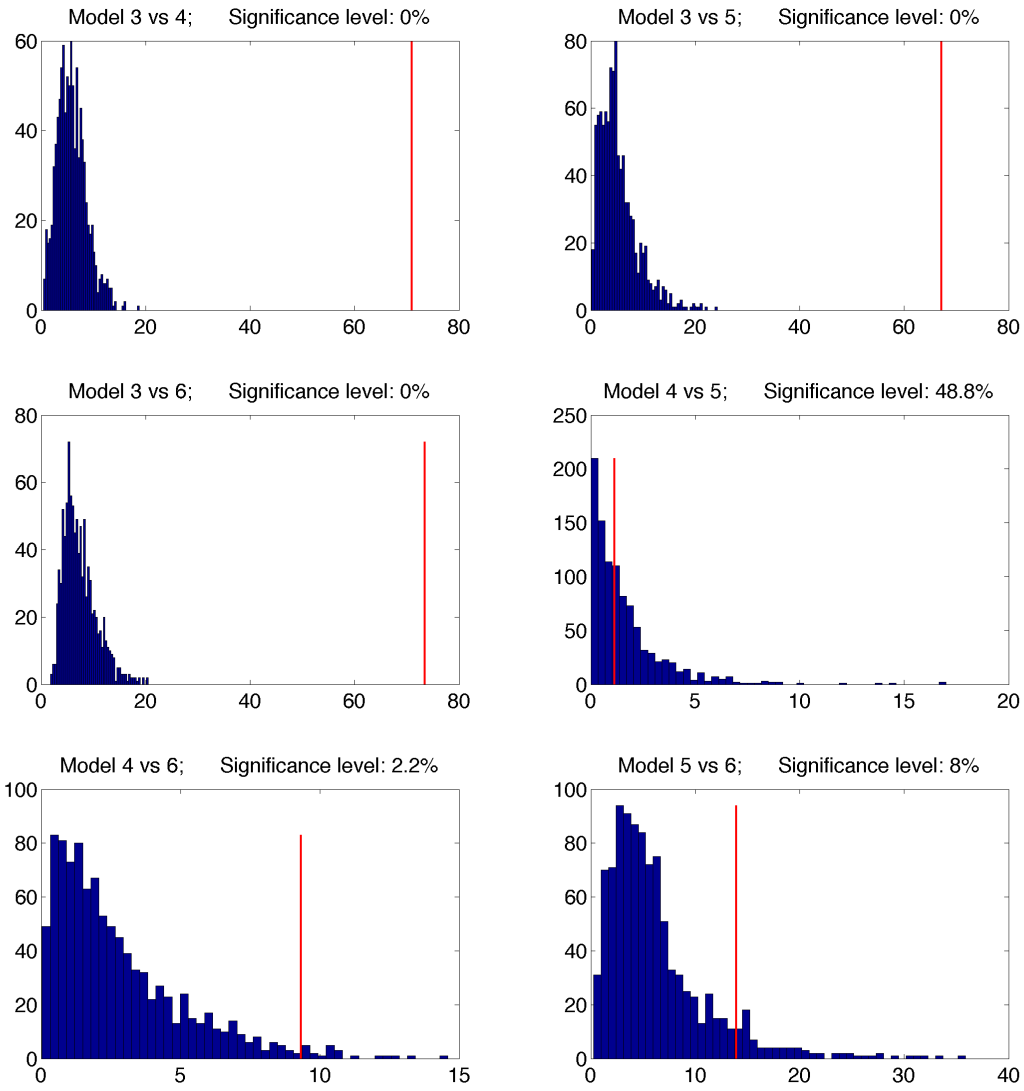

Figure 2.23: Continued.

The (simplified) result of these calculations is that these results indicate that we can distinguish between accelerating and non-accelerating solutions, with the accelerating solution being better fits to the data, but we cannot distinguish between different accelerating models.

Although the nonparametric model outperforms the parametric and other conventional models on average, the error at the the first few frequencies is still large and in some cases can

reach more than 100% at the first frequency. The relatively large error may come from several sources. First, the spectrum fitting in the first frequency bin depends on a limited number of Fourier frequencies. Another possible error source comes from the distorted estimation of the covariance matrix Λ embodied in the probability density function described in section 2.2.2.2. The covariance matrix of the Fourier coefficients is related to the noise spectrum and has two dimensions and one sample size at each frequency, giving rise to a ratio of dimension over sample size equal to 2. At the frequencies significantly affected by the regression model, the maximum likelihood estimate of Λ tend to have large error when the ratio of dimension over sample size is high (e.g. Won et al., 2013 [61]). More effort is needed to reduce the large error at the first frequency, but this is left for future work. With a more accurate estimate of the background noise, we will have an improved ability to distinguish between regression models of GMSL.

Chapter 3

Comparison of Coastal and Open Ocean Sea Level Trends

3.1 Introduction

Sea level records from tide gauges are the data source used to estimate global mean sea level (GMSL) over roughly the last one hundred years. Tide gauges are mostly distributed along the continental coasts and ocean islands and have limited spatial sampling, which raises a debate about whether coastal mean sea level (CMSL) derived from tide gauges can represent GMSL. Holgate and Woodworth (2004) [9] showed that the CMSL trend was significantly in excess of GMSL trend calculated from altimeter sea level over the period of 1993 to 2002. White et al. (2005) [10] presented a similar result that decadal trends of CMSL were bigger than those of GMSL calculated from sea level reconstructions around 1970 and during the 1990s and were smaller during the late 1970s and 1980s, but their trends over a whole 51-year period were nearly consistent. Over the time span from 1993 to 2007, the CMSL trend was found to be in good agreement with altimetry derived GMSL trend (Prandi et al. 2009 [62]). The trend difference between CMSL and GMSL in short records was attributed to the biased trend estimation resulting from the interannual variabilities. Despite a smaller difference between CMSL and GMSL trend over longer time span, model projections of sea level rise in the 21th century suggest that water mass redistribution is the dominant effect for rising sea level over the coast region, while steric changes are largest over the deep ocean, and that the sea level rise on shallow shelf area in the 21th century may be 5-6% larger than the global mean (Richter et al., 2013 [63]; Yin et al., 2010 [64]). It is therefore essential to

thoroughly examine the global and regional sea level trend differences between the coastal and open ocean.

Coastal sea level can differ from the nearby open-ocean sea level on multiple time scales because the mechanisms responsible for sea level change over the coastal and open ocean can be different (Bingham and Hughes, 2009 [65]; Hughes and Williams ,2010 [54]; Vinogradov and Ponte, 2010 [66]; Vinogradov and Ponte 2011 [67]; Bingham and Hughes, 2012 [68]; Calafat et al., 2012 [69]; Andres et al., 2013 [70]; Woodworth et al., 2014 [71]). Linear trend differences in sea level between the coastal and nearby open ocean are the primary concern in this study. On the one hand, sea level change on the coast is largely controlled by coastal ocean dynamics (Enfield and Allen, 1980 [13]), while in the open ocean steric effects induced by wind stress curl, buoyancy flux anomalies prevail (Suzuki and Ishii, 2011 [14]; Forget and Ponte, 2015 [15]). Offshore mean sea level can only represent the coastal sea level in areas where the shelf is narrow, such as the Florida Straits, and the relationship varies with the shelf geometry (Higginson et al., 2015 [72]). On the other hand, large-scale ocean circulation variations in the open ocean can induce sea level changes along the coast. Sallenger et al. (2012) [12] identified a hotspot of sea level rise along the Northeast American coast that was possibly caused by the slowdown of Atlantic Meridional Overturning Circulation (AMOC). Some model studies have showed that global sea level derived from tide gauges can substantially overestimate the true global mean value due to dynamic adjustment (Hsieh and Bryan, 1996 [73]; Zhai et al., 2011 [74]). More observational evidence is needed to determine whether the difference is significant.

Instrumental observations of sea level by altimeters and tide gauges have been used in previous studies to examine global and regional variations in sea level rise (e.g. Holgate and Woodworth (2004) [9]; Uchida and Imawaki, 2008 [75]; Sterlini et al., 2017 [76]), but they have their own advantages and drawbacks. Sea level in the open ocean can only be observed by altimeters, but it is likely contaminated by land when approaching to the coast. Sea level on the coast can be measured by tide gauges that, however, are subject to vertical land

motion (VLM). The land where tide gauges sit undergoes vertical motions caused by many phenomena including postglacial rebound, tectonic and volcanic activities, underground fluid pumping, and so on. To obtain coastal sea level changes related to ocean processes, VLM must be estimated and subtracted from tide gauge data. If the main geological process is Glacial Isostatic Adjustment (GIA) due to ice melting at the end of last ice age, the numerical estimate of GIA is a good approximation for VLM (Peltier 2004 [77]), which is a typical way of correcting land motions of tide gauges (Holgate and Woodworth 2004 [9]; White et al., 2005 [10]; Prandi et al., 2009 [62]). However, in locations where other geological processes, such as tectonics, are important, then GIA is no longer a useful VLM estimate.

Two independent and reliable VLM estimation methods were adopted by Mitchum (2000) [78], and these were referred to as the internal and external estimates. The internal method employs only the tide gauge data to estimate VLM, while the external method uses Global Positioning System (GPS) data to directly estimate VLM. The internal VLM is calculated as the true GMSL trend minus the relative sea level trend of each tide gauge record over the overlapping period. For such reason as paucity of data, estimated GMSL may deviate from the true GMSL, causing biased error of the internal land motion. Besides, sea level change at each tide gauge differs from the global mean value as regional change has geographic variation, which also contributes to the internal land motion error. Another method of making land motion estimate is the external method by using direct measurements of vertical position with GPS or Doppler Orbitography and Radiopositioning Integrated by Satellite (DORIS). Wöppelmann et al. (2009) [30] presented that GPS analysis has reached the maturity to provide useful information for separating VLM from changes of ocean volume recorded by tide gauges. As the number of GPS stations colocated with tide gauges is increasing and data records are lengthening, VLM of more and more tide gauges can be estimated from GPS data, so the external method is used in this study.

We will compare linear trends of sea level at tide gauges with and without VLM correction to trends at nearby altimeter points in the open ocean and ask whether there are

significant differences in global ocean and regional areas. To illustrate the importance of accurate estimation of VLM, VLM estimated by GPS and modeled GIA are both used for sea level correction at tide gauges. The data and methods are described in section 3.2. Comparisons of global and regional sea level trends are performed in section 3.3. Where we find significant trend differences, possible ocean processes responsible for them are investigated using simplified models in section 3.4. The last section presents our conclusions.

3.2 Data and method

3.2.1 Data

The tide gauge sea level data are from the monthly revised local reference (RLR) dataset of Permanent service for mean sea level (PSMSL). There are 1508 records that were downloaded from http://www.psmsl.org/data (Holgate et al., 2013 [79]; PSMSL, 2018). VLM derived from position data at GPS stations and model estimates of GIA are used for VLM correction of sea level trend at tide gauges, respectively. The vertical GPS velocities and their uncertainties for 493 stations are from University la Rochelle and were downloaded from http://www.sonel.org (Santamaría-Gómez et al., 2017 [80]). The GPS series are required to have at least 3 years length without discontinuities and data gaps are not allowed to exceed 30%. For the purpose of comparison, GIA induced VLM estimated with model ICE-6G_C (VM5a) (Peltier et al., 2015 [81]) are used in this study and downloaded from http://www.atmosp.physics.utoronto.ca/~peltier/data.php. Altimeter along-track data are from Brian Beckley's MEaSUREs (Making Earth Science Data Records for Use in Research Environments) record with 9.9 days interval, located at https://podaac.jpl.nasa.gov/dataset/MERGED_TP_J1_OSTM_OST_CYCLES_V42?ids=Platform&values=Jason-3, DOI: 10.5067/ALTCY-TJ142. A 7-point moving average is applied to the altimeter sea level time series to remove energy in a narrow frequency band centered on a 60-day period. There is a well-known error in the altimeter series with nearly this periodicity, but the cause is not entirely clear. In a recent review, Zawadzki et al. (2016 [82]) examined multiple non-tidal effects and concluded

that while they could not rule out these causes, the most likely cause was errors in the models used to remove tides from the altimetry data.

Tide gauges that have a GPS station within 10 km and have at least 80% of data over the period from September 1992 to December 2017 are selected and shown as filled circles in Figure 3.1. The distance scale of 10 km between a tide gauge and GPS station is determined according to the correlation of internal and external VLM rates (Doran, 2010 [53]). For later study, they are classified into groups based on their locations and are denoted by different colors. Specifically, red filled circles represent island stations and other filled circles are coastal stations along the continents. If multiple GPS stations are within 10 km away from a tide gauge, the GPS station nearest to the tide gauge is selected. Each tide gauge is paired with altimeter along-track points in the nearby open ocean that are less than 500 km away, have at least 80% valid data over the period of September 1992 to December 2017, and have a water depth exceeding 2000 m. The paired satellite along-track points are represented by black dots as shown in Figure 3.1. Any tide gauge whose number of paired altimeter points is less than 30 is rejected. One tide gauge at South America, Antofagasta, has vertical GPS velocity exceeding 30 mm/yr that is not found in nearby stations and is an extreme outlier in the GPS rates. When corrected with this GPS land motion rate estimate, the sea level trend at this tide gauge is close to 30 mm/year which is not found either in the altimeter data or the tide gauges around it, so the GPS rate at this station is believed to be unrealistic, and this tide gauge is also rejected. This selection procedure ultimately results in a total of 109 tide gauges for following studies.

For diagnostic studies of the ocean processes in section 3.4, monthly wind stress at the sea surface is derived from the Cross-Calibrated Multi-Platform (CCMP) gridded product (V2.0) with a temporal resolution of six hour and a spatial resolution of 0.25°, which is provided by Remote Sensing Systems (RSS) (www.remss.com). Linear trends of wind stress and Ekman vertical velocity derived from the wind stress are computed. Sea level pressure is used to calculate the inverse barometer response to atmosphere pressure at the tide gauges,

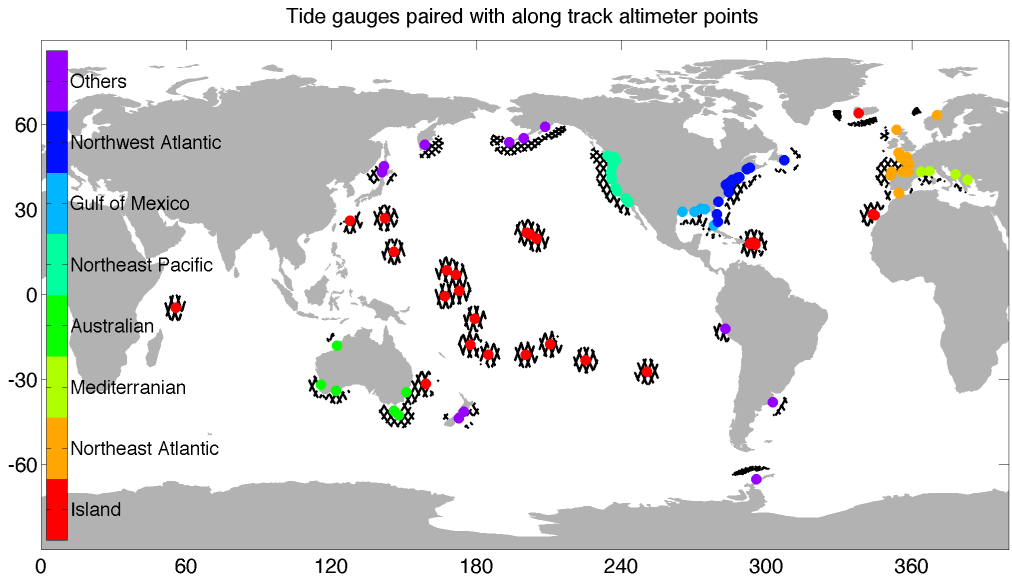

Figure 3.1: Selected tide gauges (filled and colored circles) and nearby satellite along-track points(black dots).

but the trend of this quantity is only used in the calculation of meridional gradient of sea level trend on the coast in section 3.4. The monthly sea level pressure with a spatial resolution of 2.5° from NCEP reanalysis derived products is provided by the NOAA/OAR/ESRL PSD and downloaded from https://www.esrl.noaa.gov/psd/.

3.2.2 Method

The sea level difference between one tide gauge and the nearby open ocean is expressed as:

$$\Delta\eta = \eta_{ALT} - \eta_{TG} = \delta_o + \lambda$$

where $\Delta\eta$ is the difference between sea level in the nearby open ocean from satellite altimeter, η_{ALT}, and at the paired tide gauge, η_{TG}. The difference is therefore composed of the sea level differences due to ocean processes, δ_o, and VLM of tide gauge, λ, as shown in the second

equality. Rearranging the above equation yields

$$\delta_o = \eta_{ALT} - \eta_{TG} - \lambda \tag{3.1}$$

A regression model that includes mean, trend, annual and semiannual cycle is fitted to the sea level at the selected tide gauges and the associated altimeter points. The uncertainty of tide gauge trend, σ_{TG}, is determined by model residual and its lag-1 autocorrelation ρ:

$$\sigma_{TG} = \sigma_f \sqrt{\frac{1+\rho}{1-\rho}}$$

where σ_f is the trend uncertainty for independent data commonly referred to as the formal error. The altimetry trend and its uncertainty, σ_{ALT}, are respectively calculated as the average and standard deviation of trends at the altimeter points surrounding the tide gauge. Sea level trend differences with and without VLM correction are used to investigate the influence of VLM on the trend difference, to investigate whether there is a significant global mean trend difference, and to determine which regions, if any, have large trend differences.

By propagation of error and neglecting correlation between the trend uncertainties, the uncertainty of $\Delta\eta$ trend is calculated as

$$\sigma_{\Delta\eta} = \sqrt{\sigma_{TG}^2 + \sigma_{ALT}^2}$$

Similarly, the uncertainty of δ_o trend is calculated as

$$\sigma_{\delta_o} = \sqrt{\sigma_{TG}^2 + \sigma_{ALT}^2 + \sigma_{VLM}^2}$$

where σ_{VLM} is the uncertainty of the VLM trend. The trend uncertainty of the GPS VLM is provided in the dataset, but the GIA uncertainty is not available and is assumed to be

zero here. These uncertainties are used in significance tests of the trend difference via Monto Carlo simulations.

3.3 Global and regional mean sea level trend difference between the coast and the open ocean

VLM is a significant component of relative sea level measured by tide gauges, so the absolute sea level caused by ocean processes must be estimated by using a VLM correction. GIA due to the last deglaciation is one of the most commonly applied estimates of VLM, but it does not necessarily measure VLM since other processes can be larger on the time scales that we are interested in. So we should first compare VLM observed by GPS with these due to GIA at the selected tide gauges. Figure 3.2 demonstrates that GPS VLM rates are more scattered with a larger variance than those of GIA VLM although the mean values of -0.27 mm/year and -0.48 mm/year, respectively, are close to the 1:1 line. The discrepancies between the two sets of VLM rates that were also described by previous studies (King et al., 2012 [83]; Ostanciaux et al., 2012 [84]; Hamlington et al., 2016 [85]) may lead to opposite conclusions on sea level trend comparisons. Differences between GPS and GIA VLM will be shown to have remarkably different consequences for the trend comparisons on the regional scale, such as along the Northeast Pacific coast.

Figure 3.3 shows altimetry trends versus tide gauge trends, most of which range from 0 to 10mm/year. Regressing tide gauge trends without VLM correction, with GPS VLM correction, and with GIA VLM correction on altimetry trends, respectively, give regression coefficient of 1.02, 0.87, and 0.86, implying a linear correspondence between altimetry and tide gauge sea level trends of similar magnitude.

Global average of sea level trends from tide gauges and altimeters, as well as their correlations, are calculated (Table 3.1; Table 3.2). The tide gauge and altimetry trends have similar global average of about 3mm/year with a slight difference. Altimetry mean trend is lower than tide gauge mean trend without VLM correction, but is higher after applying VLM

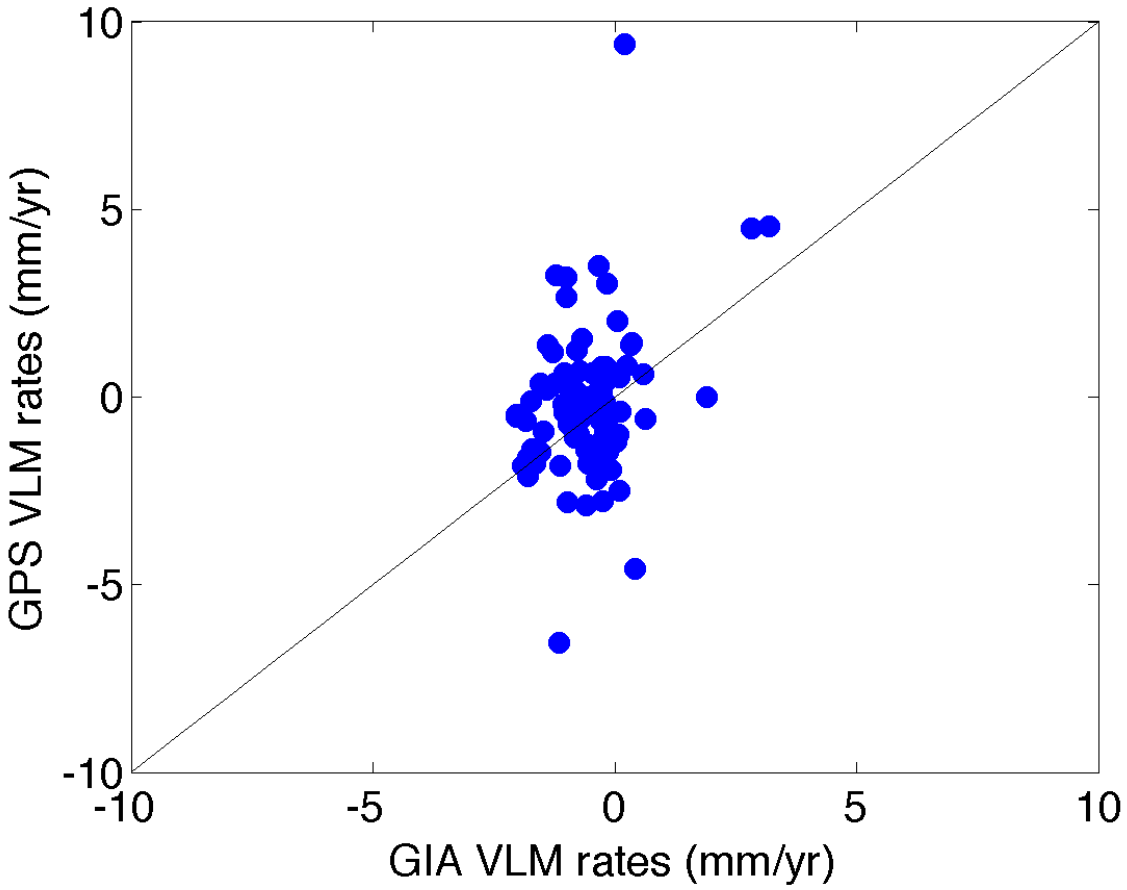

Figure 3.2: GIA VLM rates versus GPS VLM rates (mm/year).

corrections to tide gauge trends. The absolute value of global mean difference decreases as tide gauge trends are corrected for GPS VLM but increases as GIA VLM are applied. The statistical significance of the mean trend difference will be tested via Monte Carlo simulations. Given the large degree of freedom of trend pairs, tide gauge and altimetry sea level trends are significantly correlated, although the correlation is not high. It's interesting to note that, as VLM corrections are applied, the correlation is decreased. Our focus in this study is on sea level trend differences as defined by formula 3.1.

Distributions of trend differences for cases with and without VLM corrections generally show a Gaussian pattern, but demonstrate some changes from the blue to red one (Figure 3.4). Application of GPS VLM corrections results in a narrower histogram with a smaller

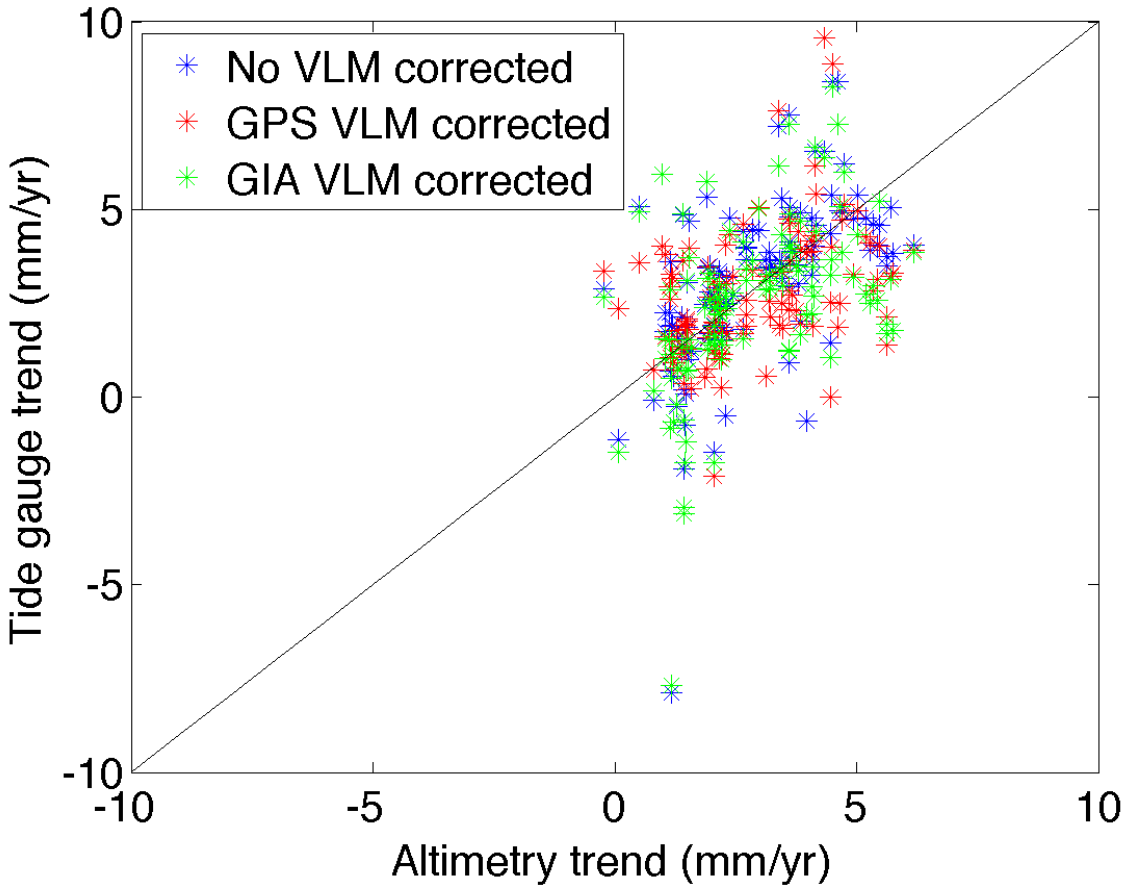

Figure 3.3: Altimetry trends versus tide gauge trends (mm/year). Cases where tide gauge trends are without, with GPS, and GIA VLM correction are denoted by blue, red and green asterisk, respectively.

Table 3.1: Global mean and scatter of sea level trends (mm/yr)

	Alimetry	Tide gauge w/o VLM	Tide gauge w/ GPS VLM	Tide gauge w/ GIA VLM
Mean	2.86	3.04	2.77	2.55
Scatter	1.46	2.28	1.71	2.27

standard deviation and mean. In contrast, applying GIA VLM corrections to tide gauge trends makes the distribution shift toward right with more positive values and less negative values, which is consistent with the change of global mean trend as shown in table 3.1. Given the scatter of the histogram, is the global mean value significantly different from zero?

Table 3.2: Correlation and difference scatter (mm/yr) between sea level trends from altimetry and tide gauges

	Tide gauge w/o VLM	Tide gauge w/ GPS VLM	Tide gauge w/ GIA VLM
Altimetry (Correlation)	0.55	0.4	0.46
Altimetry (Difference scatter)	1.92	1.75	2.06

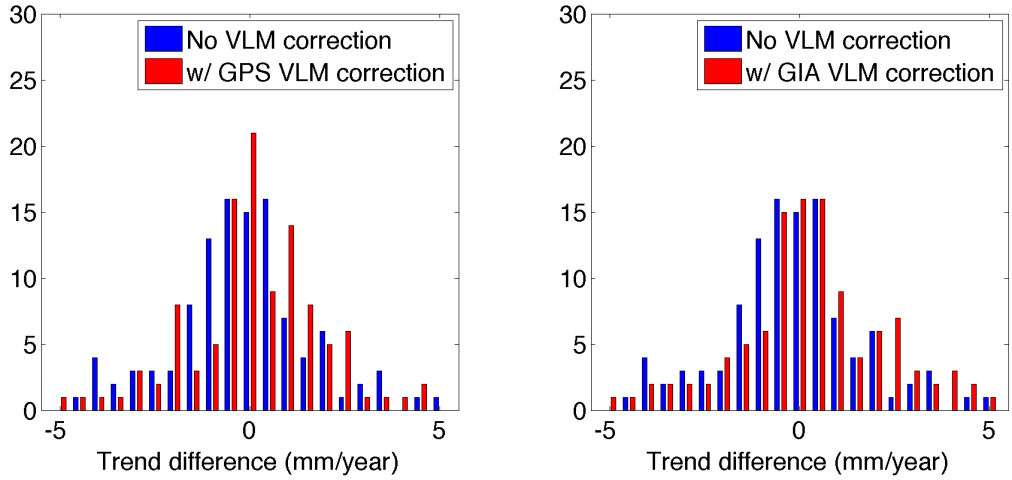

Figure 3.4: Histograms of sea level trend differences for cases without VLM correction denoted by blue bars, with GPS (left panel) and GIA (right panel) VLM correction denoted by red bars.

The significance is tested by Monte Carlo simulations. Ten thousands of random numbers are generated for each station with zero mean, and with standard deviation equal to $\sigma_{\Delta\eta}$ and σ_{δ_o} for cases without and with VLM correction, respectively. By taking average over all stations, ten thousands simulated global mean trend difference are obtained.

Figure 3.5 shows the distribution of simulated global mean trend differences together with the observed value. Mean trend difference of sea level in three cases are not significant, one of which with GIA VLM correction has an elevated trend difference resulting from more negative GIA rates. Tide gauges paired with altimeter points are presumed independent,

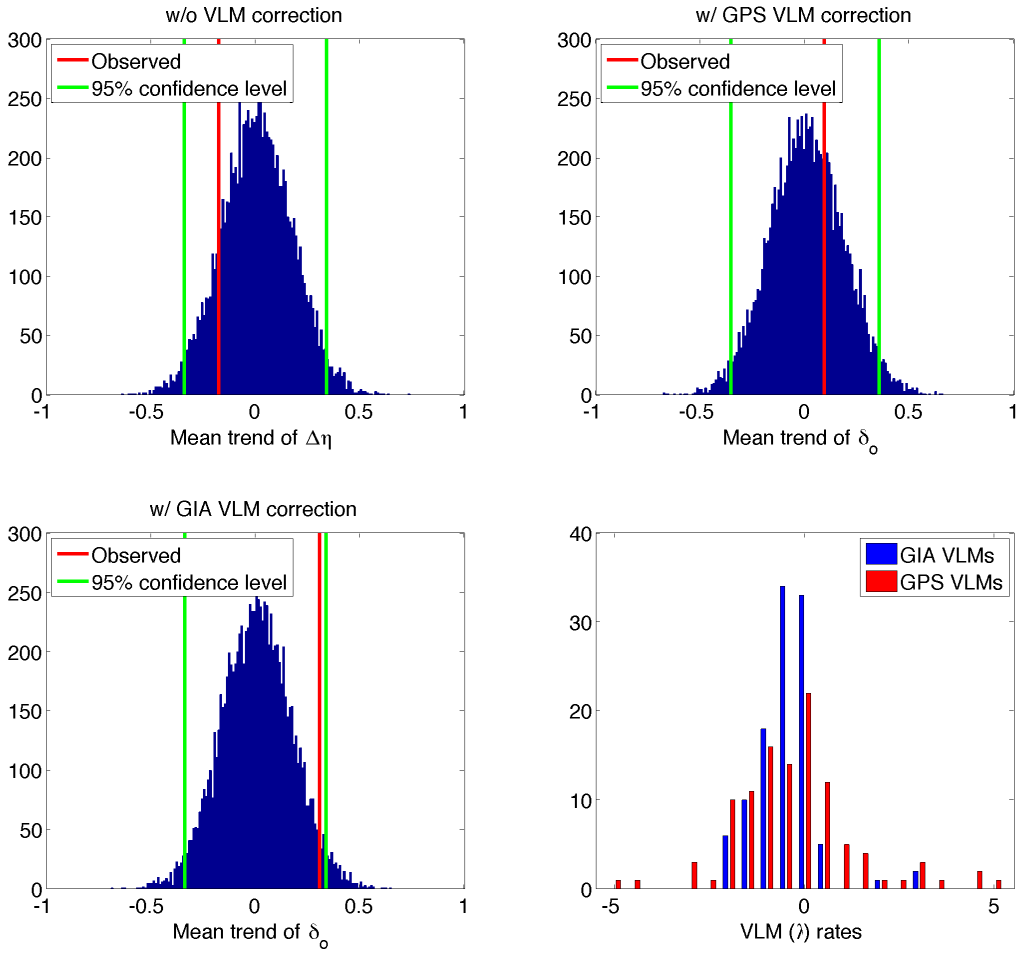

Figure 3.5: Histogram of simulated global mean trend difference (mm/year). The red line is the real observed global mean trend difference. Green lines give 95% confidence interval. The lower right panel shows histogram of VLM rates from GPS (red) and GIA (blue) respectively.

which is not always true. If we take into account correlation between them, 95% confidence interval would get wider. Although global mean trend difference with GIA VLM correction is close to 95% confidence level, it is safe to say there is no significant mean trend difference between global tide gauges and points in the nearby open ocean. The average VLM rates from GPS and GIA is -0.27 mm/year and -0.48 mm/year, respectively, indicating an overall subsidence of the selected tide gauges. Even though no significant mean difference is found over the selected global tide gauges, selection of tide gauges could impact conclusions because both regional sea level rising rates and VLM rates have geographic variations. Reconstructed

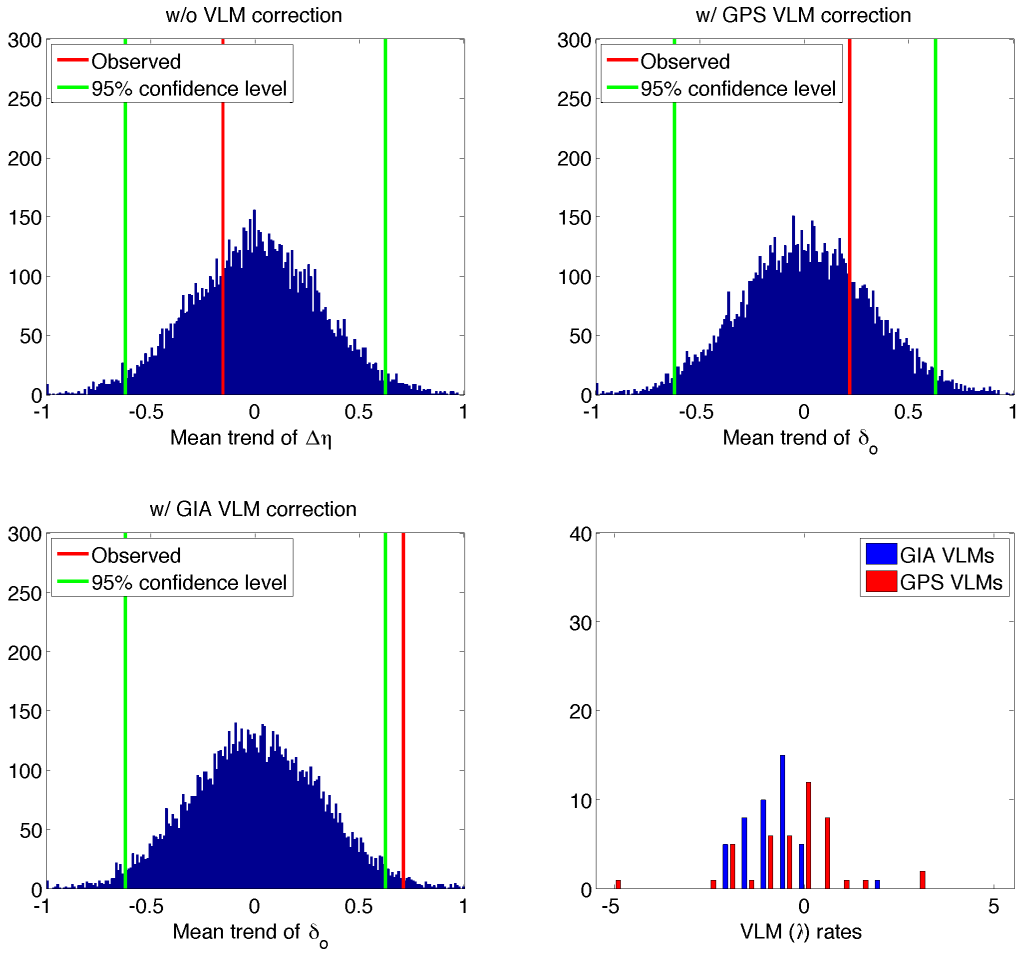

Figure 3.6: Same as Figure 3.5, but only using gauges with record of 60 years or more.

GMSL in the last century relies on long sea level records from tide gauges that are mainly located along North America and West Europe coasts. Additional examinations of mean trend difference obtained from gauges with record of 60 years or more show that mean trend difference is not significant for the case without VLM correction or with GPS VLM correction but is significant for the case with GIA VLM correction (Figure 3.6). At the tide gauges with long records, GIA VLM have more negative values than GPS VLM, that is, more gauges are experiencing subsidence induced by GIA. When comparing global mean sea level trend between coastal and open ocean using long records, this case underscores the

importance of non-GIA geological processes that have been highlighted by a recent study of GMSL (Hamlington et al., 2016 [85]).

Trend difference averaged over the global stations is not significant, but may demonstrate regional patterns because ocean processes controlling the coastal and open ocean might vary from region to region. Now we turn our attention to regional mean of trend difference. There are some worries about sea level variation across coast that is different around islands. As shown in Figure 3.1, tide gauges are split into coastal and island stations for separate investigations. Mean trend difference at islands is calculated and shown in Figure 3.7. Without VLM correction, sea level trend is significantly lower in the open ocean than at the island gauges at the 95% confidence level. Applying VLM correction gives rise to nonsignificant trend difference. Histogram of GPS VLM reveals that islands undergoing subsidence are more than those undergoing uplift. Land subsidences at Hawaii islands and other Pacific islands like Easter island have been reported in previous studies (Caccamise et al., 2005 [86]; Bouin and Wöppelmann, 2010 [87]; Becker et al., 2012 [88]). VLM predicted by GIA model are close to zero at most islands, which results in large though nonsignificant mean trend difference in the case with GIA VLM correction. Unlike island stations, the mean trend difference for coastal stations without VLM correction is not significantly different from zero (Figure 3.8). GPS VLM at coastal gauges are distributed around zero contributing little to the mean trend difference, while GIA VLM are predominantly negative at coastal gauges, which once corrected to tide gauge sea level result in a significantly larger trend in the open ocean than in the coastal ocean. Compared to island stations, using GIA to correct tide gauge sea level has a more significant impact at coastal stations where most long sea level records are from, in agreement with the test for the case using long record stations (Figure 3.6). Mean trend difference at coastal and island stations are further compared by taking difference using trend differences as shown in Figure 3.8 and 3.7. The case with GIA VLM corrections implies a substantial difference, while the case with GPS VLM correction indicates no significant difference between island and coastal stations (Figure 3.9). It's also noted

that island and coastal stations are mostly located in low and high latitude respectively. As anticipated, the mean trend differences at low latitudes (equatorward of 30°) and high latitudes (poleward of 30°) resemble these at island and coastal stations, respectively (Figure 3.10 and 3.11). The difference between island and coastal stations could be interpreted as latitudinal variation as well. Taking difference between mean trend difference at high latitudes and low latitudes still yields a contrasting result for the cases with GPS and GIA VLM correction (Figure 3.12). Based on observed VLM, no significant variation of mean trend difference between coastal and island stations or between high and low latitudes is found in our simulation tests. An opposite conclusion is drawn with GIA VLM correction, potentially resulting from model errors of GIA and large contributions from non-GIA processes.

Among these coastal regions (Figure 3.1), the mean trend difference along the Northeast Atlantic, the Northwest Atlantic and the Northeast Pacific coasts with enough tide gauges for statistical analysis are examined as well. On the Northeast Atlantic coast, where a slight subsidence on average is seen in both GPS and GIA VLM, the mean trend difference in all the cases with or without VLM correction is not significantly different from zero (Figure 3.13). In the Northwest Atlantic, the mean trend difference gets larger though nonsignificant after applying GPS VLM correction, but it becomes significant by applying GIA VLM correction (Figure 3.14). The larger trend difference is attributed to taking into account the subsidences at most of tide gauges which are consistent with the GPS observation and GIA modeling by Frederikse (2017 [89]). GIA is able to explain part of VLM along the Northwest Atlantic coast. In contrast, VLM estimated from GIA and GPS yield opposite sign for most of the stations along the Northeast Pacific coast (Figure 3.15). Correcting land subsidence induced by GIA gives rise to a significantly larger trend in the open ocean than on the coast, while correcting land uplift measured by GPS results in a significant lower mean trend in the open ocean which is opposite to that in the Atlantic coast. The discrepancy between GIA and GPS observation is possibly related to underestimation of the uplift of the western North America by GIA model and due to the active tectonics across the Cascadia subduction zone

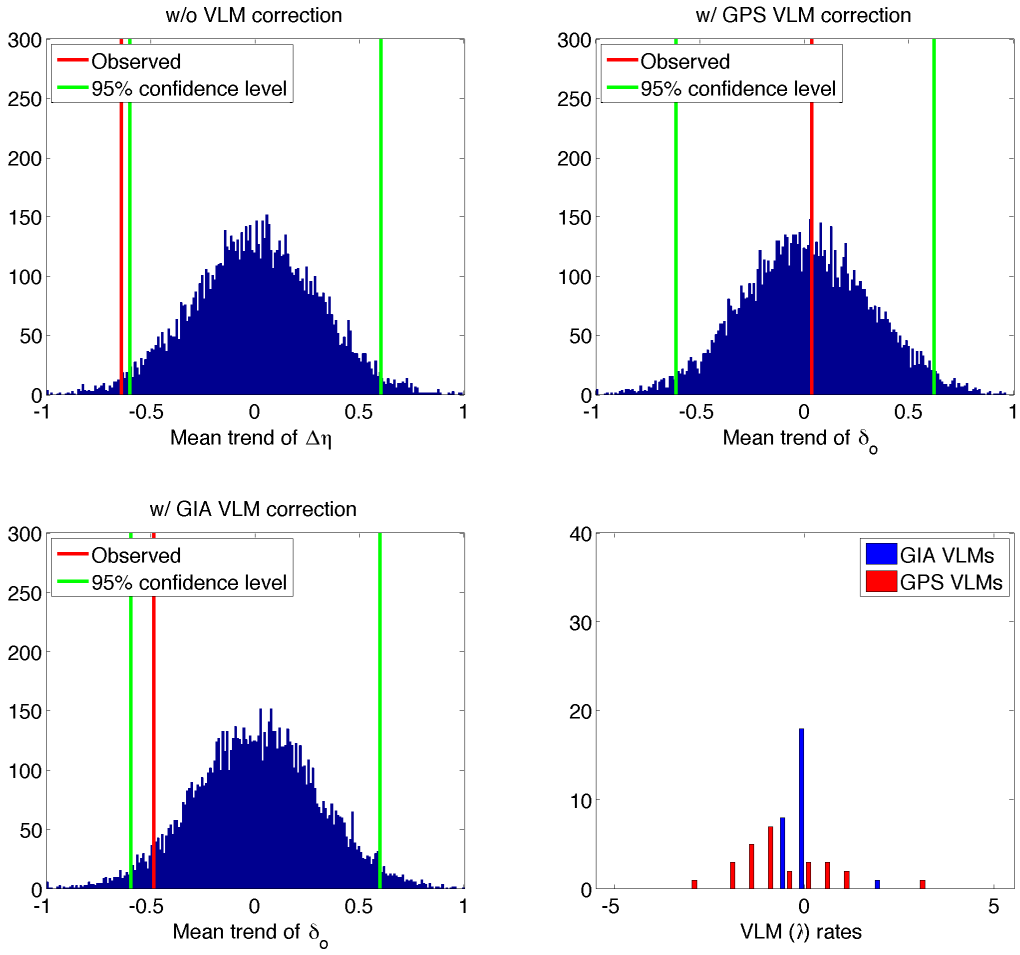

Figure 3.7: Same as Figure 3.5 but only using island stations.

(Bouin and Wöppelmann, 2010 [87]; Montillet et al., 2018 [90]). VLM estimated by GIA model and GPS measurements lead to different understandings of sea level trend, illustrating the importance of VLM at tide gauges in either global or regional sea level study. These large mean trend differences with VLM corrections observed in the Northwest Atlantic and Northeast Pacific may reflect physical processes acting between coastal and open ocean, which will be investigated in the next section.

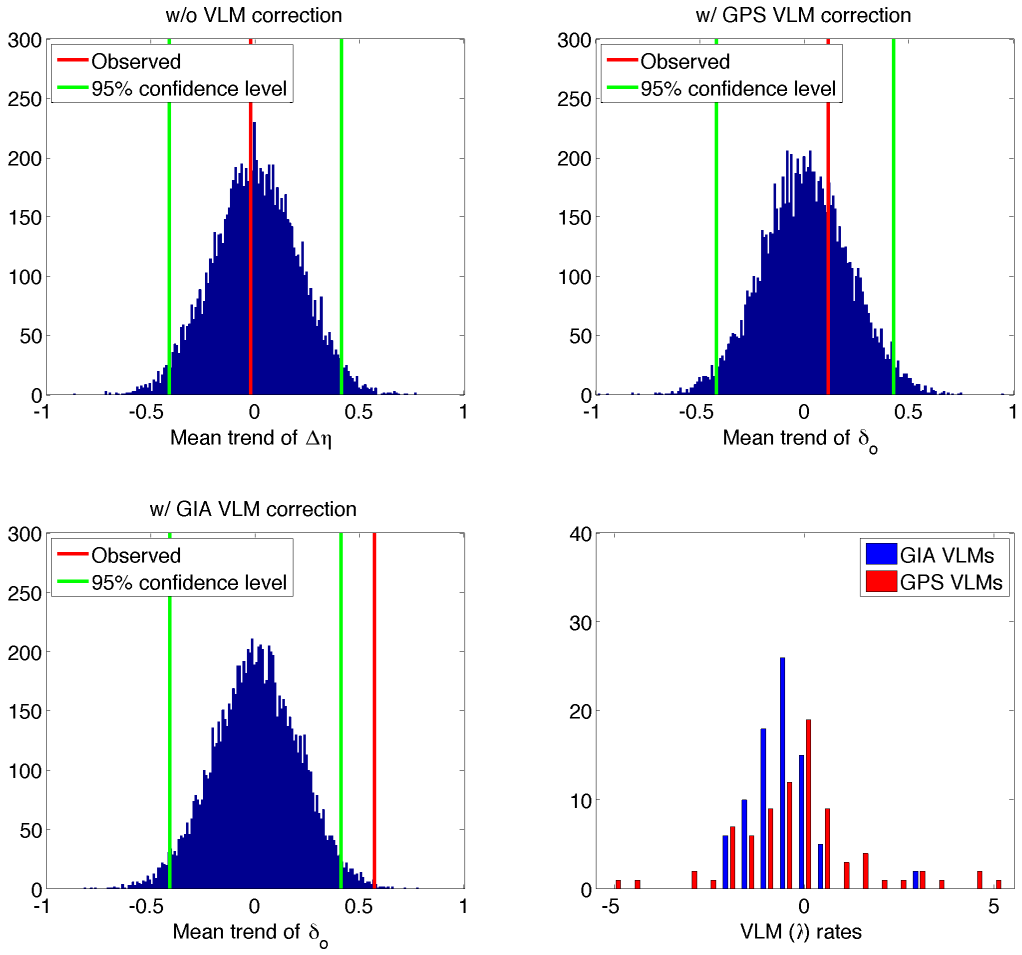

Figure 3.8: Same as Figure 3.5 but only using coast stations.

3.4 Ocean processes causing trend difference along the North America coast

Along the North America coasts, large and even significant trend difference between the coast and nearby open ocean is observed by correcting tide gauge sea level for VLM. The median position of altimeter points paired for each tide gauge is found and shown with the tide gauges along the North America coast in Figure 3.16, implying that the sea level difference between the tide gauge at the continental coast and the nearby open ocean is largely in the across-shore direction. Both local ocean processes, including alongshore wind stress and density variation, and remote ocean processes, such as Rossby and coastal wave

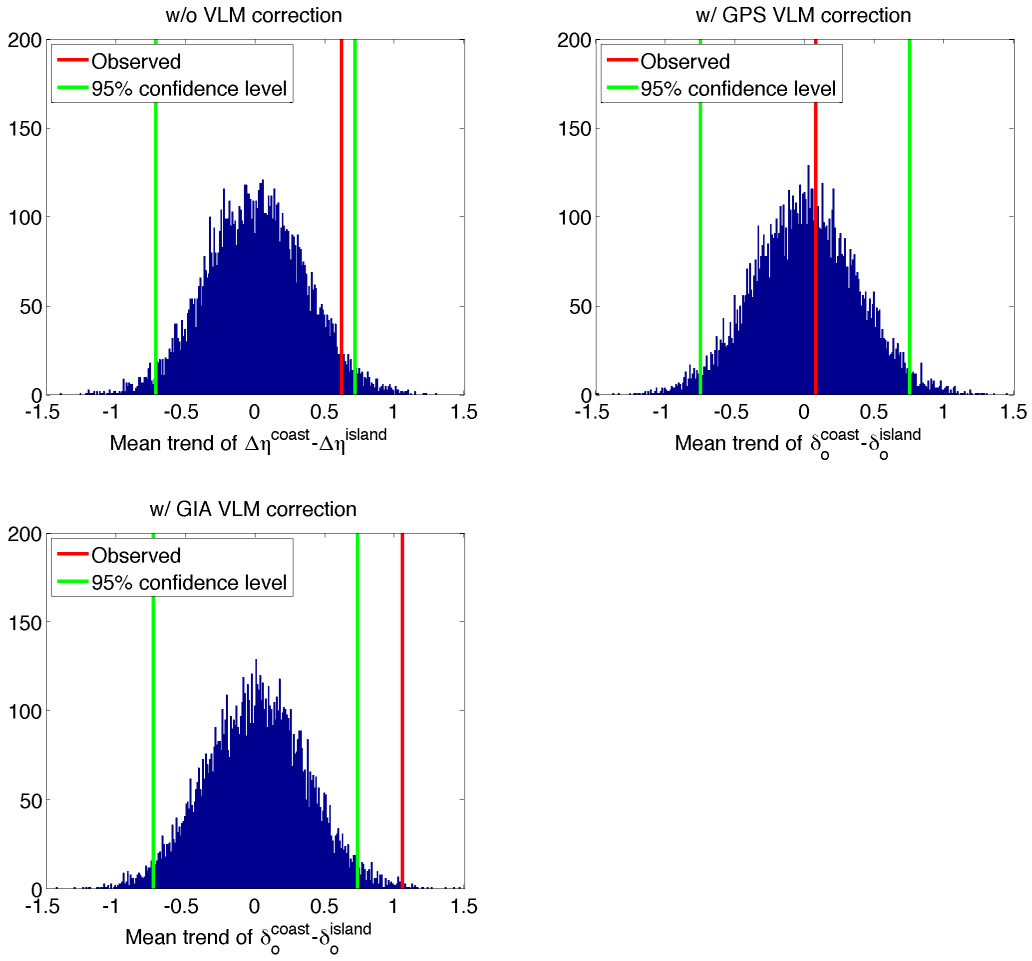

Figure 3.9: Histogram of simulated mean trend difference at coastal stations minus that at island stations (mm/year). The red line is the real observed value. Green lines give 95% confidence interval.

propagations, can lead to sea level difference in the across-shore direction. Although other dynamics such as boundary current variation that is closely related to forcing in the interior ocean play important roles in the western and eastern boundary, two local and one remote ocean processes are explored in an attempt to qualitatively diagnose the possible mechanisms responsible for sea level difference between the coastal and open ocean.

First, alongshore wind stress gives rise to Ekman transport across the coast, forming alongshore current with high sea level on the right-hand side when facing downstream in the Northern Hemisphere. Geostropic balance holds in across-shore direction, while alongshore

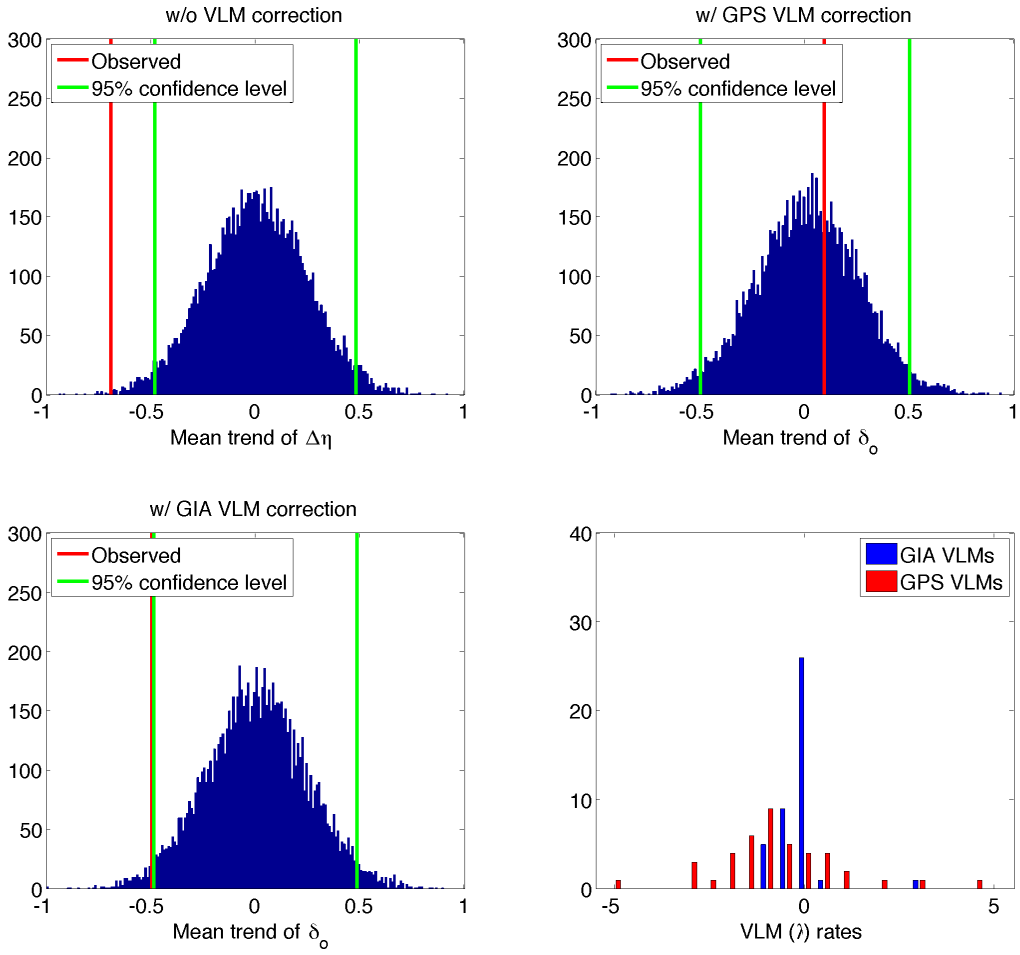

Figure 3.10: Same as Figure 3.5 but only using stations equatorward of 30°.

wind stress is approximately balanced by bottom friction in alongshore direction (Sandstorm, 1980 [91]; Hong et al., 2000 [11]; Li and Clarke, 2005 [92]; Andres et al., 2013 [70]; Piecuch et al., 2016 [93]). One such simplified barotropic model in the across-shore and alongshore direction follows

$$-fv = -g\frac{\partial \eta}{\partial x}$$
$$\frac{\tau_w^y}{\rho H} = \frac{\tau_{bot}^y}{\rho H}$$

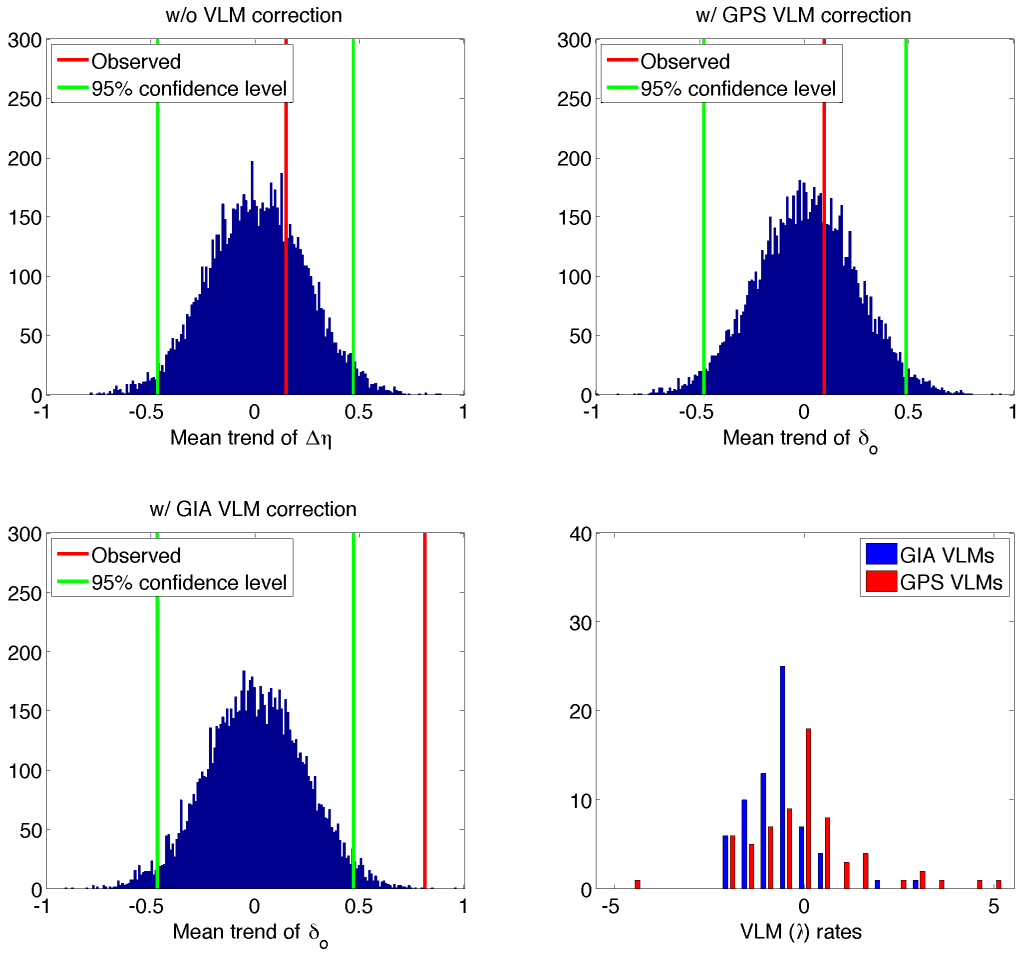

Figure 3.11: Same as Figure 3.5 but only using stations poleward of 30°.

where f is the Coriolis parameter, v is alongshore velocity, g is the gravity acceleration, τ_w^y and τ_{bot}^y are alongshore wind stress and bottom stress respectively, ρ is sea water density, H is water depth. τ_{bot}^y is parameterized as $\tau_{bot}^y = \rho r v$ where r is friction coefficient with a typical value of 4×10^{-4} m/s (Gill, 1982 [94]). Sea level difference between coast and offshore is derived as

$$\delta_{o1} = \frac{f}{\rho g r} \int_{coast}^{offshore} \tau_w^y dx$$

which relates the sea level trend difference to the trend of alongshore wind stress.

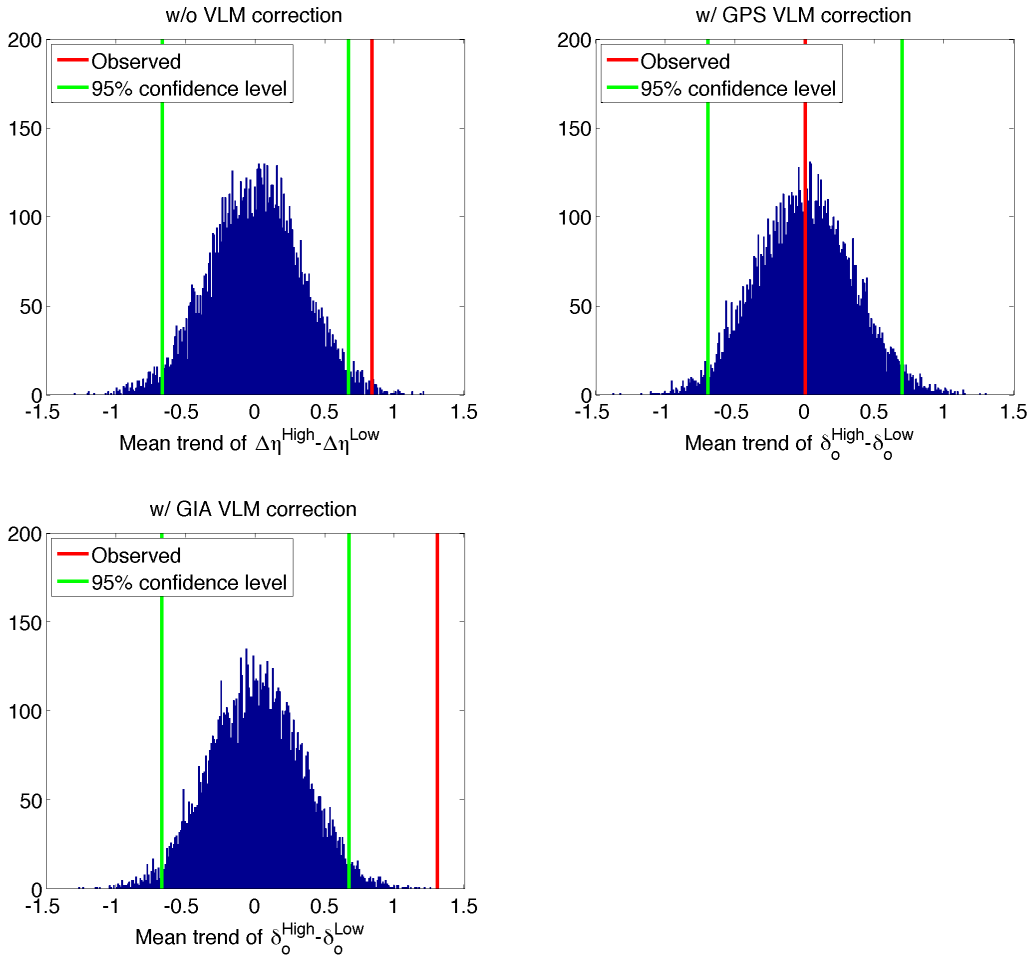

Figure 3.12: Histogram of simulated mean trend difference in the region poleward of 30° minus that in the region equatorward of 30° (mm/year). The red line is the real observed value. Green lines give 95% confidence interval.

Second, baroclinic processes causing density variation from coast to offshore can contribute to across-shore sea level difference (e.g. Liu and Weisberg, 2007 [95]). At tide gauges, water is too shallow for obvious sea level changes to be generated by density variations. As water becomes deeper in the open ocean, the density variation may take effect in changing sea level. Since no long-term hydrographic observations over the vast boundary regions are available, Ekman pumping in the open ocean is used to represent the local baroclinic process with the impact of density variation to sea level change at tide gauges neglected.

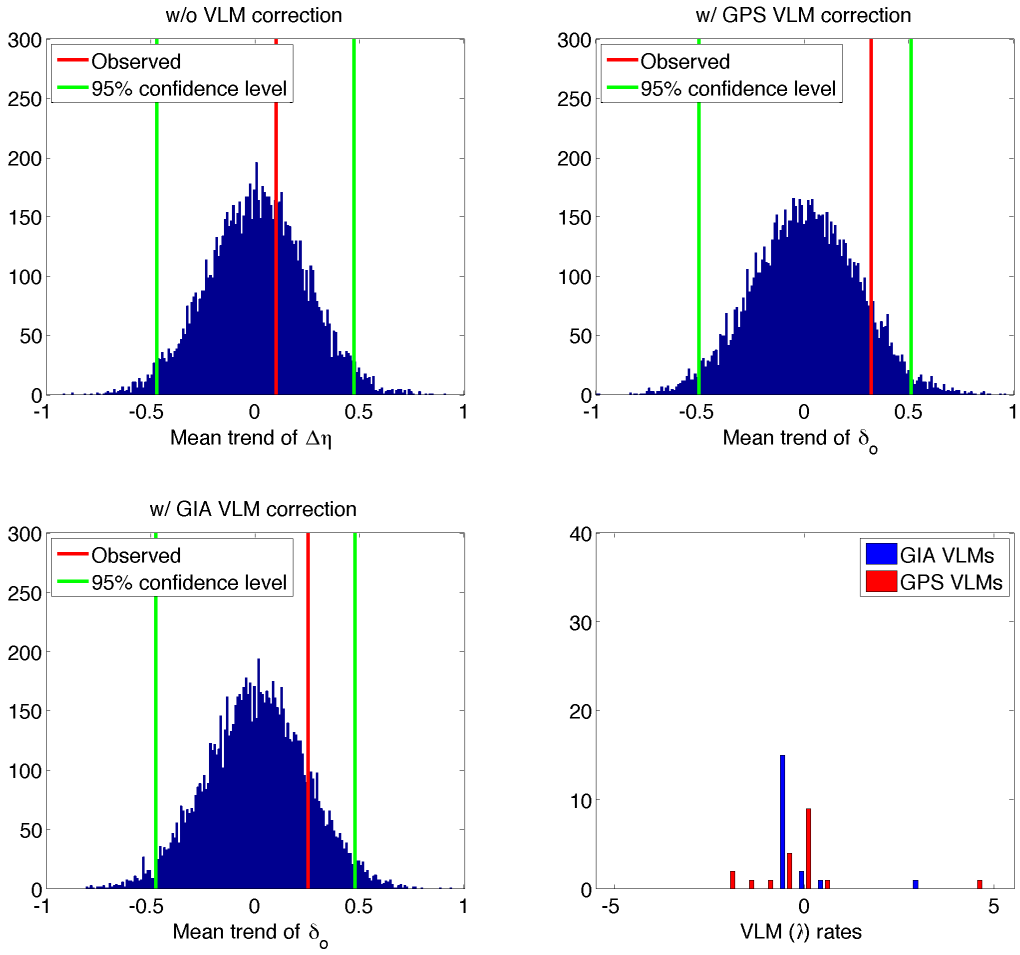

Figure 3.13: Same as Figure 3.5 but only using the Northeast Atlantic stations.

Third, Rossby waves propagating from the open ocean to the western boundary and subsequent propagation of coastal waves can lead to sea level difference between the western boundary and interior ocean (Hong et al., 2000 [11]; Minobe et al., 2017 [96]). By this mechanism, the sea level difference across the western boundary is linked to sea level gradient along the coast (Minobe et al., 2017 [96]).

$$\eta_W - \eta_I = \frac{f}{\beta}\frac{\partial \eta_W}{\partial y}$$

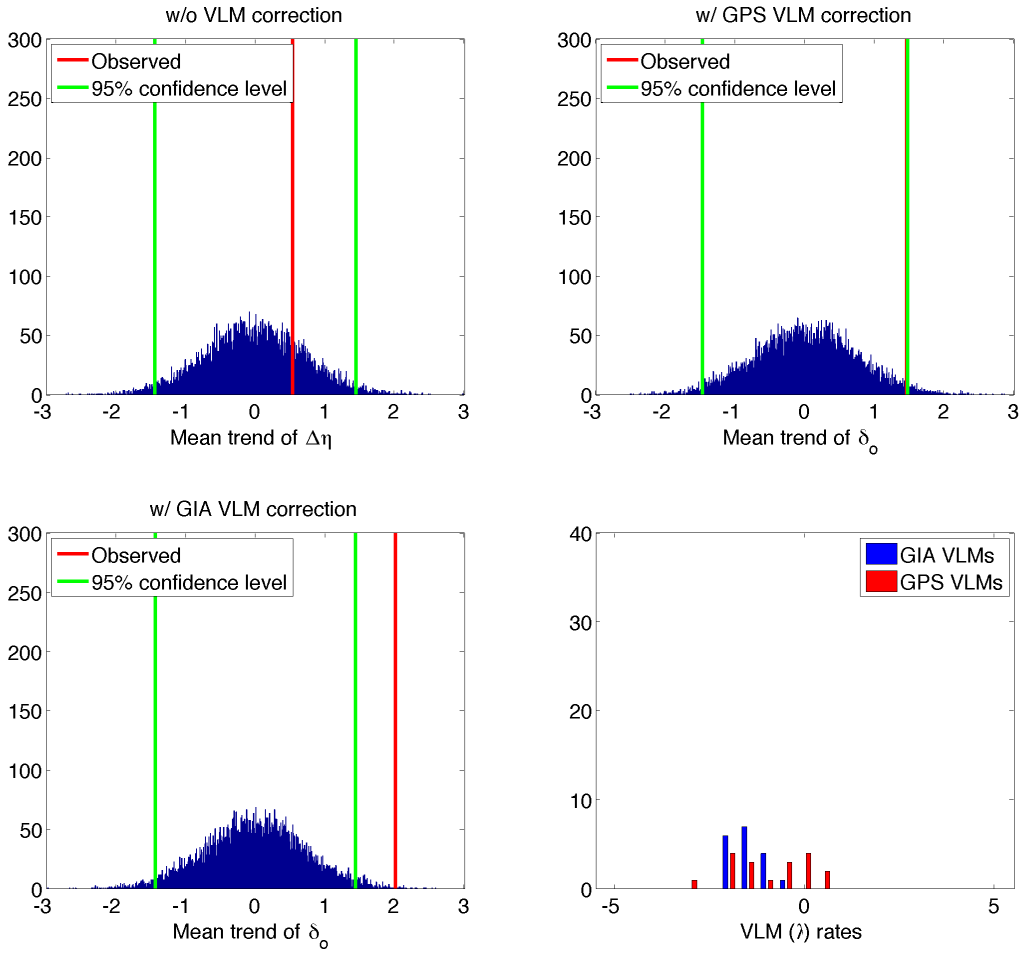

Figure 3.14: Same as Figure 3.5 but only using the Northwest Atlantic stations .

where η_W and η_I are sea level in the western boundary and interior ocean, respectively, β is meridional derivative of the Coriolis parameter.

Similarly, as sea level variation at the eastern coast generated locally or remotely radiates westward, a sea level difference between the eastern boundary and interior ocean can emerge. By comparing contributions from local and remote wind forcing, Thompson et al., (2014 [97]) suggested that the decreased rate of sea level on the northeast Pacific coast is largely determined by tropical variability that is communicated poleward through coastal waveguides. Based on the derivations by Minobe et al., (2017 [96]) using a reduced gravity model in the western boundary, the mass conservation equation is integrated westward from

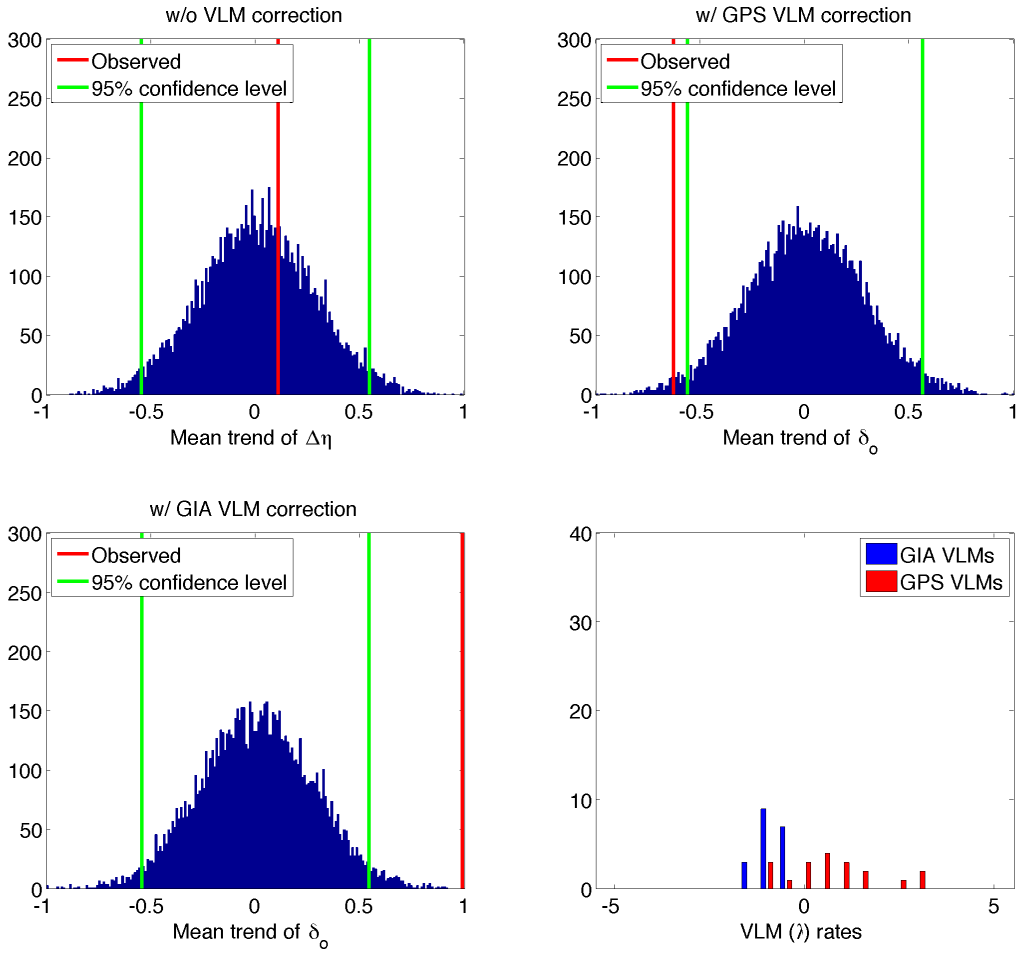

Figure 3.15: Same as Figure 3.5 but only using the Northeast Pacific stations.

the eastern coast to the eastern end of interior ocean. Same derivation procedures for boundary sea level applied by Minobe et al., (2017 [96]) are followed in this study except that the boundary being used is the eastern boundary. Consequently, sea level at one location on the eastern coast can be expressed as

$$\eta_E(x_E(y), y, t) = \frac{f}{f(y_S)}\eta(x_E, y_S, t) - f\int_{y_S}^{y}\frac{\beta}{f^2}\eta(x_I(y'), y', t)dy'$$

where $x_E(y)$, $x_I(y)$ are the point on the eastern boundary and in the interior ocean, respectively; y_S is coastal point to the south of $x_E(y)$; η_E is sea level on the eastern boundary,

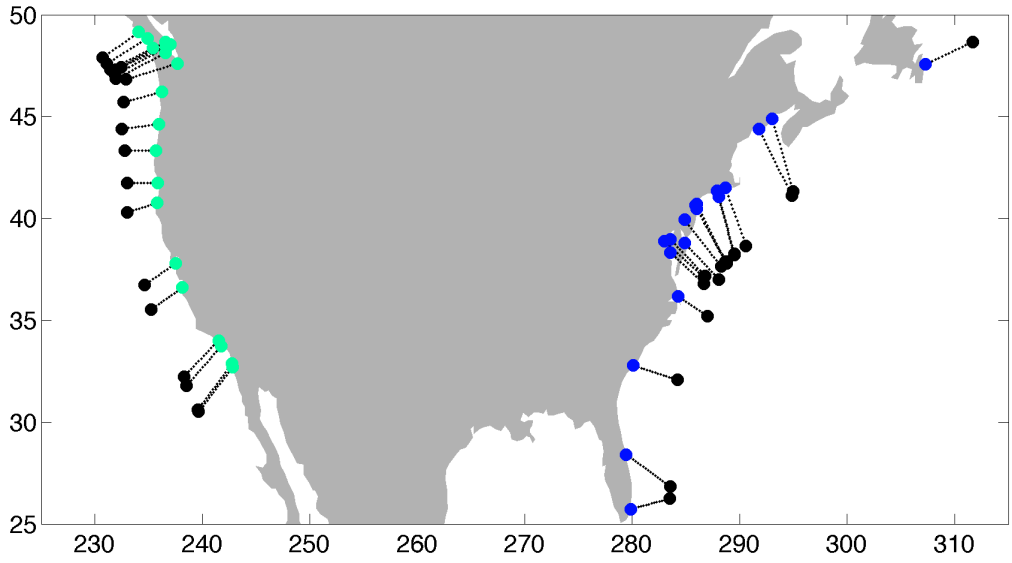

Figure 3.16: Tide gauge locations (green and blue solid circles) and median positions of altimeter points in the nearby open ocean (black solid circles) along the North America coast.

having a combined contribution from sea level to the south and westward radiation of sea level signals via Rossby waves.

Taking derivative of the above equation yields

$$\eta_E - \eta_I = \frac{f}{\beta}\frac{\partial \eta_E}{\partial y}$$

Either on the western or the eastern boundary, the sea level difference induced by Rossby and coastal wave propagations can therefore be expressed as

$$\delta_{o2} = -\frac{f}{\beta}\frac{\partial(\eta_{TG} + \lambda)}{\partial y}$$

where $\eta_{TG} + \lambda$ is sea level at tide gauges corrected for VLM. A numerical model study by Huthnance (2004 [98]) showed that transmission of sea level signal across the coast happens when the alongshore scale is large relative to the decay distance for coastal trapped mode 1, implying that tide gauges are effective monitors of sea level variations only on the large

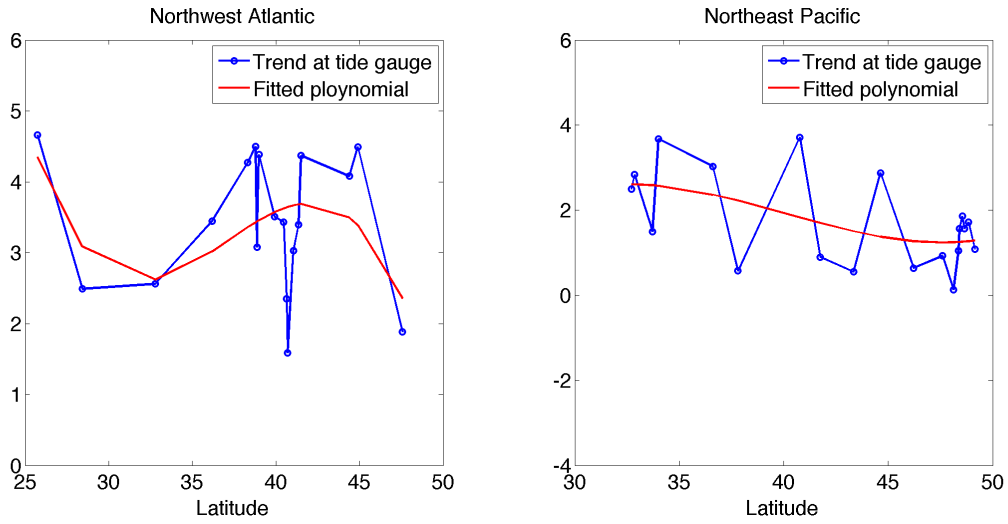

Figure 3.17: Sea level trend (mm/year) corrected for inverse barometric effect and GPS VLM (blue) and fitted curve (red) along the Northwest Atlantic and Northeast Pacific coast.

scale of thousands of kilometers. As a consequence, δ_{o2} tends to be manifested on relatively large scale. However, tide gauges are not evenly distributed along the coast where sea level variation could be dominated by local forcing such as wind stress. Here one cubic polynomial is fitted to the coastal sea level trend corrected for inverse barometric effect. When corrected with GPS VLM, coastal sea level trend exhibits a trough around $32°N$ and a peak around $40°N$ along the Northwest Atlantic coast, and a decreasing trend with latitude along the Northeast Pacific coast (Figure 3.17). When corrected with GIA VLM, coastal sea level trend demonstrates a decreasing trend with latitude along both coasts (Figure 3.18). The fitted curves will be used in the computation of meridional gradient of sea level trend along the coasts.

The three dynamic processes are investigated individually on the Northwest Atlantic coast as shown in Figure 3.19. Meridional variation of sea level trend differences seems to track the trend of alongshore wind stress. Mean trend difference caused by this process is 0.07 mm/year that is much smaller than the observed value of 1.46 mm/year in the case with GPS VLM correction. Trends of Ekman vertical velocity with an inverted sign are averaged in the same nearby open-ocean domain embracing altimeter points paired to each tide gauge.

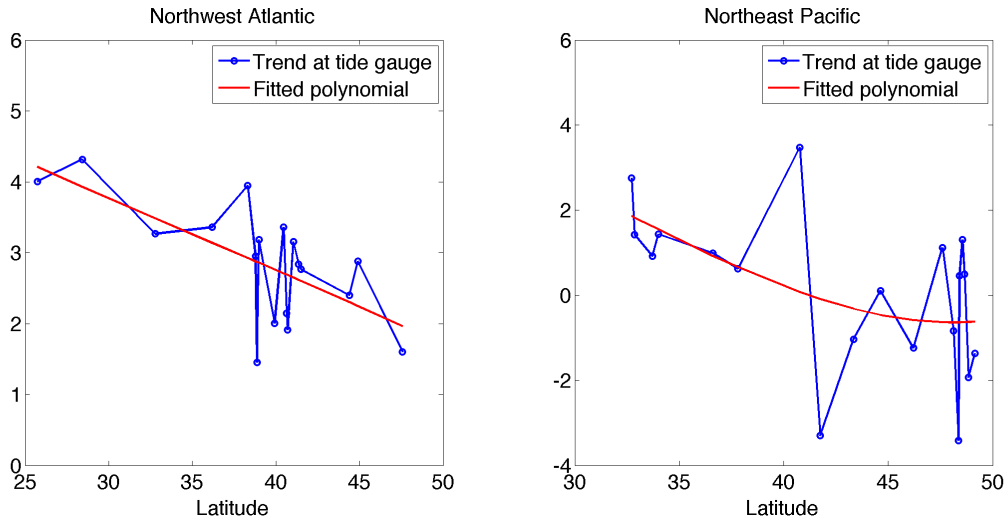

Figure 3.18: Same as Figure 3.17, but coastal sea level is corrected for inverse barometric effect and GIA VLM.

Ekman pumping likely contributes to the observed trend difference south of $37°N$, whereas contradicts the observation north of $37°N$, with an average negative value. As a result, the overall effect of Ekman pumping in the nearby open ocean is opposite to the observed mean trend difference. The remote forcing via Rossby and coastal wave propagations is shown unable to explain the observed δ_o. Although the three processes are qualitatively diagnosed, none of these can fully account for the observed trend difference. In the Northeast Pacific, the three processes are not compatible with the observed trend difference with an overall opposite sign, suggesting that none of these processes are responsible for the trend difference in the Northeast Pacific (Figure 3.20).

The dynamics controlling sea level difference between the coastal and open ocean is more complex than our simplified models. For instance, the costal wave propagation and sea level variations can be impacted by the continental shelf geometry (Ezer, 2017 [99]), which may be one of the reasons that the sea level differences predicted by the wave model markedly depart from the observation along both coasts. It is noted that, on the Northeast Pacific coast, all three processes yield mean trend difference opposite to the observation, which imply the possibility that there is some error in the observation. One error source may come

from GPS VLM rates. GPS time series have shorter length than sea level observation, with average length in the Northeast Pacific coast and Northwest Atlantic coast equal to 13 years and 8.6 years, respectively. If VLM varied nonlinearly over the study period, the linear trend of VLM derived from a shorter time series would invalidate the GPS VLM correction. When GIA VLM are used to correct the coastal sea level, modeled trend difference resulting from wave propagations is closer to the observed δ_o on the Northwest Atlantic coast. In addition, the alongshore wind stress has a larger correlation with the observed δ_o with GIA VLM correction and contributes to trend difference north of $42°N$ on the Northeast Pacific coast. Longer GPS observations are needed to examine the possibility of inherent error in GPS VLM rates over a short period.

Apart from the three processes studied here, other ocean processes may play roles in causing sea level difference. Basin boundary current is an alternative driver of sea level tilt along the coast such as on the south coast of Japan (Lin et al., 2015) and on the Northwest Atlantic boundary (Ezer et al., 2013 [100]; Yin and Goddard 2013 [101]; Thompson and Mitchum, 2014 [102]). Boundary current variability is more related to forcing in the interior ocean, which is beyond the scope of our study. Moreover, sea level signals induced by Greenland ice melting or originated from the Labrador Sea likely propagate southward to impact coast sea level (Stammer, 2008 [103]; Frederikse, 2017 [89]). Numerical model is an alternative way to investigate the sea level trend difference induced by more complex ocean processes.

3.5 Conclusions

Sea level records from tide gauges are the main resource of estimating GMSL for the period before the satellite altimeter era. Most of tide gauges sit along the coast, casting doubt on whether global or regional sea level rising rates measured by tide gauges can represent that in the open ocean. The combination of tide gauge sea level, VLM measured by GPS and modeled by GIA model, and satellite altimeter sea level are used to investigate the sea level

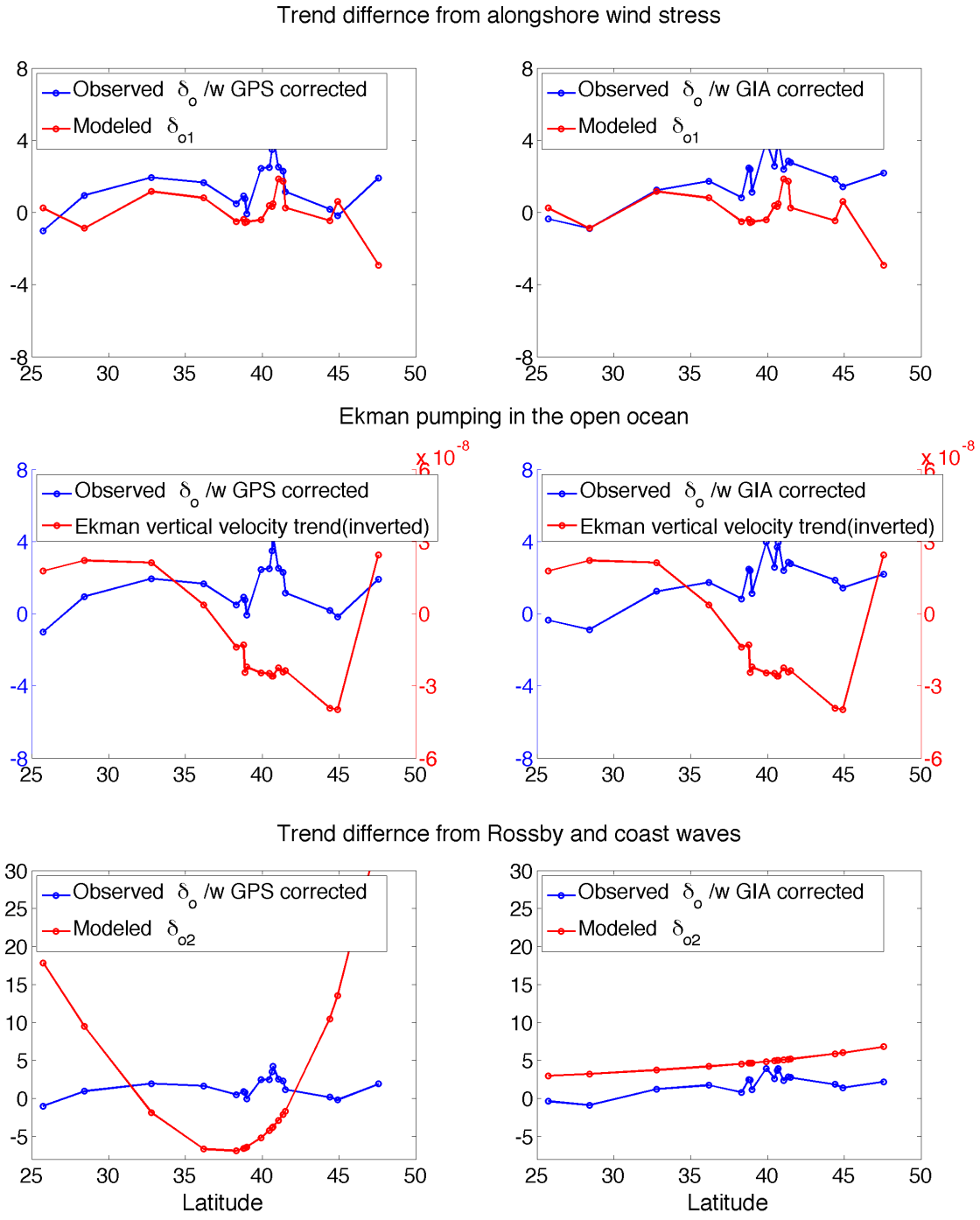

Figure 3.19: Sea level trend difference corrected for VLM (blue curve) with modeled value caused by alongshore wind stress and wave propagations (red curve) and Ekman vertical velocity inverted (red curve), along the Northwest Atlantic coast. Left panel is for the case with GPS VLM corrected; right panel is for the case with GIA VLM corrected.

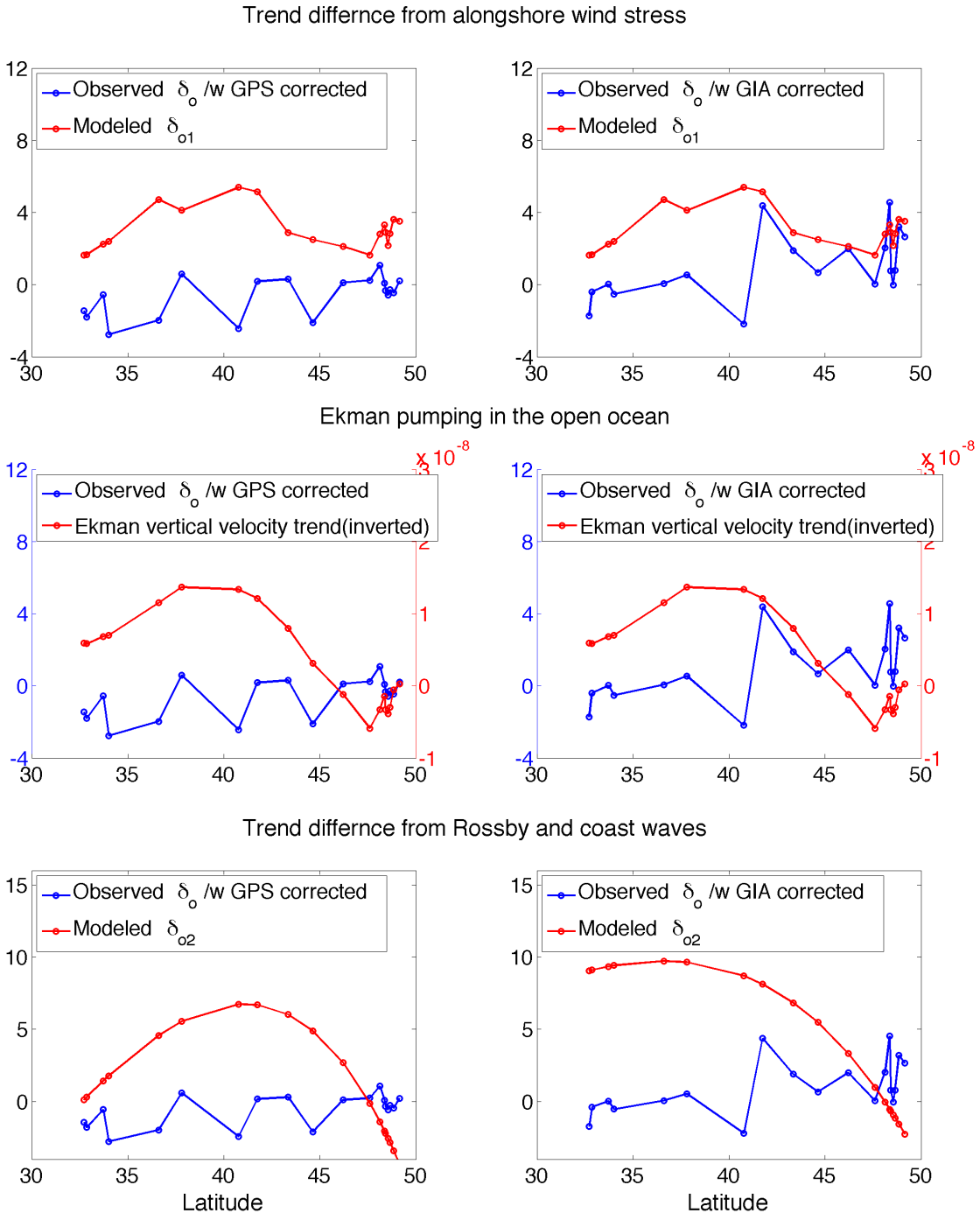

Figure 3.20: Same as Figure 3.19, except along the Northeast Pacific coast.

trend difference between the coastal and nearby open ocean, which is defined as altimetry sea level trend minus tide gauge sea level trend corrected for VLM. Discrepancies between GPS and GIA VLM are observed, which have profound impacts to inferring absolute sea level change at tide gauges. For comparison, both GPS and GIA VLM are used to correct the relative sea level observed by tide gauges.

By Monte Carlo simulations, no significant global mean trend difference is found from the selected tide gauges with GPS VLM corrected. Owing to different geographic settings, tide gauges are further grouped into several coastal regions and open ocean islands. After applying GPS VLM corrections, the mean trend difference of sea level between the coastal and open ocean is not significant either in the coastal group of stations or in the group of island stations. The mean trend difference in the coastal stations is not significantly different from that in island stations. As most island and coastal stations are located at low and high latitudes respectively, the mean trend differences at low and high latitudes are not significant, in agreement with the results for island and coastal groups. Among the global coastal regions, the North America coast and Northeast Atlantic coast have the majority of tide gauges with long records and enough gauges for statistical analysis of mean trend difference. The mean trend difference is not significant on the Northeast Atlantic coast. After correcting GPS VLM at tide gauges, a relatively large positive mean trend difference close to the 95% confidence level is found on the Northwest Atlantic coast, while a significant negative mean trend difference is observed on the Northeast Pacific coast. However, different inferences are drawn from the cases with GIA VLM instead of GPS VLM corrections when using the tide gauges with long record, coastal tide gauges, high-latitude tide gauges, especially gauges along the Northeast Pacific coast. These results highlight the potential problem of using VLM estimated by GIA models to correct relative sea level measured by tide gauges and the importance of non-GIA geological processes for sea level comparisons.

The large and even significant sea level difference over the Northwest Atlantic and Northeast Pacific coast are qualitatively diagnosed with alongshore wind stress, Ekman pumping

in the nearby open ocean, and Rossby and coastal wave propagations. On the Northwest Atlantic coast, alongshore wind stress tracks the sea level difference but contributes a small amount to the mean trend difference. Local Ekman pumping shows contrasting contribution to trend difference over the regions separated by $37°N$. Rossby wave and subsequent coastal wave propagations can not explain the observation either. On the Northeast Pacific coast, none of these simple models can account for the sea level difference, implying that more complex dynamics are likely involved. Nevertheless, we can not exclude the possibility of inherent error in GPS VLM rates over a short period.

Chapter 4

Diagnosis of Large-scale, Low-frequency Sea Level Variability in the Northeast Pacific Ocean

4.1 Introduction

Ocean variables such as sea surface temperature (SST) have demonstrated considerable large-scale, low-frequency variability in the North Pacific, with the primary modes being the Pacific Decadal Oscillation (PDO) (Mantua et al., 1997 [104]) and the North Pacific Gyre Oscillation (NPGO) (Di Lorenzo, et al., 2008 [17]). These modes have profound impacts on climate, fishery, ocean ecosystem and so on. As a result, it is important to understand mechanisms of the low-frequency variability. Compared to the PDO derived from SST, sea surface height (SSH) gives a smoother pattern and a time index linked more closely to ocean interior processes (Cummins et al., 2005 [16]). In this study, the climate variability in the Northeast Pacific (NP) is examined through diagnosis of large-scale, low-frequency sea level variability.

Sea level variability responds to external forcing, of which wind stress is one of the dominant forcings. Wind stress anomalies in the NP could be the result of local ocean-atmosphere interaction or be connected to the tropical Pacific through atmospheric teleconnection. Despite the ambiguity of the source of wind stress anomalies, the resulting Ekman pumping gives rise to sea level and thermocline change. Linear damping of wind forcing can account for the interdecadal variations of dynamic height in the North Pacific (Lagerloef 1995 [20]). This stochastic model (Markov model) with a damping timescale of 1-2 years also accounts for the interdecadal variation of the depth of main pycnocline over the North Pacific (Cum-

mins and Lagerloef 2002 [105]). Capotondi et al. (2005) [23] attributed the success of the local Ekman pumping model in explaining a large fraction of pycnocline variability to the standing character of the pycnocline anomalies. In addition to the local forcing, sea level also changes in response to ocean adjustments via wave propagations. For example, Kelvin waves propagate eastward in the tropical Pacific and then northward along the East Pacific coast. The SSH anomalies originating from the tropical Pacific together with these locally produced in the NP propagate westward as Rossby waves.

Another mechanism for low-frequency variability, therefore, involves Rossby waves that integrate oceanic response to the atmospheric forcing along the Rossby wave trajectory (Qiu, 2002 [21]). Cummins and Lagerloef (2004) [22] modeled interannual variability of SSH both by the reduced-gravity, quasi-geostrophic model and by the Markov model. The quasi-geostrophic model including the baroclinic Rossby wave did not show apparent advantages over the Markov model. However, Fu and Qiu (2002) [106] applied the same linear model but with a weak damping coefficient and demonstrated high correlation between observed and modeled SSH that rely on the propagation of Rossby waves. These studies suggest that ocean damping and Rossby wave propagation can individually account for low-frequency variations without reference to the other process, which raises the question of what are the relative roles of ocean damping and Rossby wave in causing the large-scale, low-frequency sea level variability.

Thompson (2012) [107] presented a method to diagnose the relative importance of the two dynamic mechanisms, using a linear model with both Rossby wave propagation and linear damping included. An integral solution to the linear model, derived by Method of Characteristics (MOC), was fitted to SSH anomalies from observation and numerical model. Given ranges of the fitting model coefficients, the optimized coefficients were obtained by minimizing the differences between the fitted SSH and real SSH in a least-squares sense. The best fitted SSH anomalies account for substantial amounts of variance of the real SSH anomalies. This model has a good performance over the central NP area, but is limited by a

poor performance over the area off the eastern coast of North Pacific and over the open ocean west of dateline. Besides wind forcing, other dynamic processes, such as eddy forcing and buoyancy forcing that are not included in this linear model, can contribute to low-frequency sea level variability. The North Pacific is rich in mesoscale eddies with large amplitudes (Chelton et al., 2007 [108]; Chelton et al., 2011 [4]). Mesoscale eddies with horizontal scale of tens and hundreds kilometer have similar western propagating phase speed as Rossby waves but are generated by different physical mechanisms such as current instability. The eddy momentum flux is shown to generate low-frequency variability in the North Pacific (Qiu et al.,2015 [26]). Model studies showed that Ekman pumping dominates the first-mode response, while buoyancy forcing results in the second-mode response in the North Pacific (Thompson and Ladd, 2004 [25]; Thompson and Dawe, 2007 [109]). In the south tropical Atlantic and Pacific, part of SSH anomalies are caused by surface buoyancy fluxes and westward propagations under the framework of first-mode Rossby wave model (Piecuch and Ponte, 2012 [110]; Piecuch and Ponte, 2013 [111]). A better model of sea level evolution should include the nonlinear momentum flux (Reynold stress) and buoyancy forcing.

When large-scale, low-frequency sea level variability responding to external forcing is studied, the quasi-geostrophic (QG) approximation is usually made and the resulting equations are often solved by a vertical normal mode expansion followed by a MOC solution for each vertical mode (Gill 1982 [94]). Through projections of sea level onto vertical modes determined by ocean mean density, it is suggested that both the first and second modes, and even higher modes are important for the sea level variability (Suzuki an Ishii, 2011 [14]). Although the first mode as an approximation of vertical structure of main thermocline is often used to study sea level variability, it may deviate from true process significantly and cannot explain some phenomena (Perkins and Holbrook, 2001 [112]; Li and Clarke, 2007 [113]; Maharaj et al., 2007 [114]; Maharaj et al., 2009 [115]). A more complete description of ocean processes is often given by ocean general circulation model (OGCM) making approximations of the primitive governing equation (e.g. Aoki et al., 2009 [116]). Nevertheless

interpretation of which mechanism drives sea level variability is difficult as most of the ocean dynamics are mixed together in the OGCM.

A simplified dynamical model that does not resort to a vertical normal mode expansion is developed here to enable a better understanding of the sea level response. The relative roles of local and remote forcing in driving SSH anomalies and how different external forcings contribute to sea level variations in the NP are investigated with this diagnostic sea level model. Data and methods are described in section 4.2, and the questions raised above are addressed in section 4.3. Conclusions are presented in the last section.

4.2 Data and methods

4.2.1 Data

Daily sea level anomalies from January 1993 to December 2016 on 0.25° grids are obtained from the Ssalto/Duacs altimeter products, which are produced and distributed by the Copernicus Marine and Environment Monitoring Service (CMEMS) (http://www.marine.copernicus.eu). Mean dynamic topography was produced by the CLS Space Oceanography Division and distributed by Aviso, with support from CNES (http://www.aviso.altimetry.fr/). The mean sea level and sea level anomalies are used to calculate eddy forcing in the following analysis. Wind stress is derived from the Cross-Calibrated Multi-Platform (CCMP) gridded surface winds (V2.0). The product has a temporal resolution of 6 hours and a spatial resolution of 0.25° degrees, and are produced by Remote Sensing Systems (RSS) (www.remss.com). Monthly means of net shortwave radiation flux, net longwave radiation flux, sensible heat flux, and latent heat flux, precipitation rate are computed from the NCEP reanalysis provided by NOAA/OAR/ESRL PSD (http://www.esrl.noaa.gov/psd/). These are used to calculate buoyancy flux. The climatology fields of in situ temperature and salinity from the World Ocean Atlas version 2 (WOA13 V2) on 1° grids are used for calculations of mean density, and are downloaded from https://www.nodc.noaa.gov/OC5/woa13/. The sea level anomalies and the three forcing fields are smoothed spatially by a two-dimensional

Guassian filter with half amplitude response at 450 km, and are smoothed temporally by a filter with half amplitude response at 5 months. The smoothed anomalies are interpolated to $1^\circ \times 1^\circ$ grids. Seasonal signals and linear trends are removed from these filtered data.

4.2.2 Methods

The governing equations are the Boussinesq horizontal momentum equations, the continuity equation, hydrostatic balance, and the linearized equation of state:

$$\begin{aligned}
\frac{\partial u}{\partial t} + u\frac{\partial u}{\partial x} + v\frac{\partial u}{\partial y} + w\frac{\partial u}{\partial z} - fv + \frac{\partial}{\partial x}\left(\frac{p}{\rho_0}\right) &= \frac{\partial}{\partial z}\left(\frac{\tau^x}{\rho_0}\right) - \lambda u \\
\frac{\partial v}{\partial t} + u\frac{\partial v}{\partial x} + v\frac{\partial v}{\partial y} + w\frac{\partial v}{\partial z} + fu + \frac{\partial}{\partial y}\left(\frac{p}{\rho_0}\right) &= \frac{\partial}{\partial z}\left(\frac{\tau^y}{\rho_0}\right) - \lambda v \\
\frac{\partial p}{\partial z} + \rho g &= 0 \\
\frac{\partial u}{\partial x} + \frac{\partial v}{\partial y} + \frac{\partial w}{\partial z} &= 0 \\
\frac{\partial \rho}{\partial t} - \frac{\rho_0}{g}N^2 w &= \frac{\partial B}{\partial z} - \lambda\rho
\end{aligned}$$

where ρ_0 is constant density, ρ is density deviation from ρ_0, p is pressure deviation from the reference pressure p_0 associated with ρ_0, τ^x and τ^y are zonal and meridional stress forcing components, N is buoyancy frequency, B is buoyancy flux that is positive upward, λ is the Rayleigh damping coefficient in the momentum equation, which also serves as a Newtonian damping coefficient in the equation of state. At the surface, τ is the wind stress, denoted by τ_0, and the surface buoyancy flux is expressed as,

$$B(0) = -\frac{\alpha_T Q}{C_p} + \beta_S (E - P) S$$

where $\alpha_T = -\frac{1}{\rho}\frac{\partial \rho}{\partial T}$ is the thermal expansion coefficient, $\beta_S = \frac{1}{\rho}\frac{\partial \rho}{\partial S}$ is the salinity contraction coefficient, C_p is the specific heat of water, Q is surface heat flux (positive downward), E is evaporation, P is precipitation, and S is surface salinity.

From the equation of state, vertical velocity w scales as $W \sim \frac{\Delta\rho UH}{\Delta\rho_0 L}$, where $\Delta\rho$, $\Delta\rho_0$, U, H, L are scales for the density perturbation, mean density variation from the surface to bottom ocean, velocity, depth and horizontal length, respectively. Then the scale ratio of $w\frac{\partial u}{\partial z}$ to $u\frac{\partial u}{\partial x}$ is $\frac{\Delta\rho}{\Delta\rho_0}$, which is of order of 10^{-1}. Analogously, the two vertical momentum advection terms are small compared to the horizontal advection parts and are neglected in the following analysis.

The velocity components u, v, and w are expanded in an asymptotic series with the small number ϵ, written as $u = u_g + \epsilon u_a + \cdots$, $v = v_g + \epsilon v_a + \cdots$. The Coriolis parameter f is expanded to $f = f_0 + \beta y$, where $\beta = \frac{\partial f}{\partial y}$. These are substituted into the governing equations.

To the order of $\mathcal{O}(\epsilon^0)$, momentum and continuity equations follow

$$\begin{aligned} -f_0 v_g + \frac{\partial}{\partial x}\left(\frac{p}{\rho_0}\right) &= 0 \\ f_0 u_g + \frac{\partial}{\partial y}\left(\frac{p}{\rho_0}\right) &= 0 \\ \frac{\partial u_g}{\partial x} + \frac{\partial v_g}{\partial y} &= 0 \end{aligned}$$

To order $\mathcal{O}(\epsilon^1)$, the momentum and continuity equations are

$$\begin{aligned} \frac{\partial u_g}{\partial t} - f_0 v_a - \beta y v_g &= \frac{\partial}{\partial z}\left(\frac{\tau^x}{\rho_0}\right) - u_g\frac{\partial u_g}{\partial x} - v_g\frac{\partial u_g}{\partial y} - \lambda u_g \\ \frac{\partial v_g}{\partial t} + f_0 u_a + \beta y u_g &= \frac{\partial}{\partial z}\left(\frac{\tau^y}{\rho_0}\right) - u_g\frac{\partial v_g}{\partial x} - v_g\frac{\partial v_g}{\partial y} - \lambda v_g \\ \frac{\partial u_a}{\partial x} + \frac{\partial v_a}{\partial y} + \frac{\partial w}{\partial z} &= 0 \end{aligned}$$

where the momentum advection terms are moved to the right side.

The horizontal momentum and continuity equations are combined to form

$$\left(\frac{\partial}{\partial t} + \lambda\right)\left(\frac{\partial v_g}{\partial x} - \frac{\partial u_g}{\partial y}\right) - f_0\frac{\partial w}{\partial z} + \beta v_g = \frac{1}{\rho_0}\frac{\partial}{\partial z}(\boldsymbol{\nabla} \times \vec{\tau}) - \frac{1}{f_0}E$$

where $\vec{\tau} = \vec{\mathbf{i}}\tau^x + \vec{\mathbf{j}}\tau^y$, $E = (\vec{\mathbf{u}}_g \cdot \boldsymbol{\nabla})\nabla^2\left(\frac{p}{\rho_0}\right)$, and $\vec{\mathbf{u}}_g = \vec{\mathbf{i}}u_g + \vec{\mathbf{j}}v_g$. For large scale motions, $\left(\frac{\partial}{\partial t} + \lambda\right)\left(\frac{\partial v_g}{\partial x} - \frac{\partial u_g}{\partial y}\right)$ is small compared to βv_g, and is therefore neglected. The equation becomes

$$\frac{\beta}{f_0}\frac{\partial}{\partial x}\left(\frac{p}{\rho_0}\right) - f_0\frac{\partial w}{\partial z} = \frac{1}{\rho_0}\frac{\partial}{\partial z}(\boldsymbol{\nabla} \times \vec{\tau}) - \frac{1}{f_0}E \tag{4.1}$$

The hydrostatic balance and the equation of state are combined to give

$$\left(\frac{\partial}{\partial t} + \lambda\right)\frac{\partial}{\partial z}\left(\frac{p}{\rho_0}\right) + N^2 w = -\frac{g}{\rho_0}\frac{\partial B}{\partial z} \tag{4.2}$$

These two equations are often solved by a vertical normal mode expansion followed by MOC solution for each vertical mode. The resulting sea level equation for n^{th} mode is expressed as

$$\frac{\partial h_n}{\partial t} + c_n\frac{\partial h_n}{\partial x} = -\alpha_n^W W_0 + \alpha_n^E L_n^2 E_0 - \alpha_n^B B_0 - \lambda h_n \tag{4.3}$$

where subscript n is mode number, c is wave propagation velocity; α^W, α^E, α^B are forcing coefficients related to mode eigenvector and vertical structure of forcing. $W_0 = \boldsymbol{\nabla} \times \frac{\vec{\tau}_0}{\rho_0 f_0}$, $E_0 = (\vec{\mathbf{u}}_0 \cdot \boldsymbol{\nabla})\nabla^2 h$, $B_0 = \frac{B(0)}{\rho_0}$ are surface Ekman pumping velocity, vorticity advection term, and buoyancy forcing, respectively; $L_n = \frac{c_n^2}{f_0}$ is wave deformation radius for n^{th} mode. In the case of first mode ($n = 1$), α_n^W can be approximated by $\frac{\Delta\rho}{\rho}$ on the order of 10^{-3}; L_n^2 is on the order of $10^3 km^2$ with a deformation radius $L_n = 30km$; α_n^E and α_n^B are on the order of 1; λ^{-1} ranges from one year to six years or longer.

An alternative approach is adopted in this study partly in order to avoid the vertical mode expansion. Integratating (4.1) from the ocean bottom $-H(x, y)$ to depth z with $w(-H) = 0$, we obtain

$$\frac{\beta}{f_0}\int_{-H}^{z}\frac{\partial}{\partial x}\left(\frac{p}{\rho_0}\right)dz' - f_0 w = \int_{-H}^{z}\frac{\partial}{\partial z}\left(\boldsymbol{\nabla} \times \frac{\vec{\tau}}{\rho_0}\right)dz' - \frac{1}{f_0}\int_{-H}^{z} E\, dz' \tag{4.4}$$

Summation of (4.2) and $\frac{N^2}{f_0} \times$ (4.4) yields

$$\left(\frac{\partial}{\partial t}+\lambda\right)\frac{\partial}{\partial z}\left(\frac{p}{\rho_0}\right)+\frac{\beta N^2}{f_0^2}\int_{-H}^{z}\frac{\partial}{\partial x}\left(\frac{p}{\rho_0}\right)dz' = N^2\int_{-H}^{z}\frac{\partial}{\partial z}\left(\boldsymbol{\nabla}\times\frac{\vec{\tau}}{\rho_0 f_0}\right)dz' - \frac{N^2}{f_0^2}\int_{-H}^{z}E\,dz' - \frac{g}{\rho_0}\frac{\partial B}{\partial z}$$

Assuming $\vec{\tau}\to 0$ as $z=-H$ and using the Leibniz rule, we have

$$\left(\frac{\partial}{\partial t}+\lambda\right)\frac{\partial}{\partial z}\left(\frac{p}{\rho_0}\right)+\frac{\beta N^2}{f_0^2}\frac{\partial}{\partial x}\left(\int_{-H}^{z}\frac{p}{\rho_0}dz'\right)-\frac{\beta N^2}{f_0^2}\frac{\partial H}{\partial x}\frac{p(-H)}{\rho_0} = N^2W-\frac{N^2}{f_0^2}\int_{-H}^{z}E\,dz'-\frac{g}{\rho_0}\frac{\partial B}{\partial z} \tag{4.5}$$

where $W=\boldsymbol{\nabla}\times\frac{\vec{\tau}}{\rho_0 f_0}$.

Integrating (4.5) vertically from $-H$ to 0 and again using the Leibniz rule gives

$$\left(\frac{\partial}{\partial t}+\lambda\right)\frac{p(0)}{\rho_0}-\left(\frac{\partial}{\partial t}+\lambda\right)\frac{p(-H)}{\rho_0}+\frac{\beta}{f_0^2}\frac{\partial}{\partial x}\int_{-H}^{0}N^2\int_{-H}^{z}\frac{p}{\rho_0}dz'dz - \frac{\beta}{f_0^2}\int_{-H}^{0}\frac{\partial N^2}{\partial x}\int_{-H}^{z}\frac{p}{\rho_0}dz'dz-\frac{\beta}{f_0^2}\frac{\partial H}{\partial x}\left[N^2\int_{-H}^{z}\frac{p}{\rho_0}dz'\right]_{-H} - \frac{\beta}{f_0^2}\frac{\partial H}{\partial x}\frac{p(-H)}{\rho_0}\int_{-H}^{0}N^2\,dz = \int_{-H}^{0}N^2W dz-\frac{1}{f_0^2}\int_{-H}^{0}N^2\int_{-H}^{z}E\,dz'dz-\frac{gB(0)}{\rho_0}$$

The fifth term on the left side of the above equation is zero, and the fact that $\frac{p(-H)}{\rho_0}$ is small compared to $\frac{p(0)}{\rho_0}$ enables us to neglect terms associated with $\frac{p(-H)}{\rho_0}$, leading to

$$\left(\frac{\partial}{\partial t}+\lambda\right)\frac{p(0)}{\rho_0}+\frac{\beta}{f_0^2}\frac{\partial}{\partial x}\int_{-H}^{0}N^2\int_{-H}^{z}\frac{p}{\rho_0}dz'dz - \frac{\beta}{f_0^2}\int_{-H}^{0}\frac{\partial N^2}{\partial x}\int_{-H}^{z}\frac{p}{\rho_0}dz'dz = \int_{-H}^{0}N^2W dz-\frac{1}{f_0^2}\int_{-H}^{0}N^2\int_{-H}^{z}E\,dz'dz-\frac{gB(0)}{\rho_0} \tag{4.6}$$

Define

$$\frac{p}{\rho_0} = gh(x,y,t)\psi_p(x,y,z)$$
$$W = W_0(x,y,t)\psi_\tau(x,y,z)$$
$$E = gE_0(x,y,t)\psi_E(x,y,z)$$

where h is sea level variable, ψ_p, ψ_τ, ψ_E are respectively vertical structure functions for pressure, stress, and vorticity advection with $\psi_p(x,y,0) = 1, \psi_\tau(x,y,0) = 1, \psi_E(x,y,0) = 1$. $W_0 = \boldsymbol{\nabla} \times \frac{\vec{\tau}_0}{\rho_0 f_0}$ and $E_0 = (\vec{\mathbf{u}}_0 \cdot \boldsymbol{\nabla})\nabla^2 h$ are surface wind forcing and surface vorticity advection term called eddy forcing in this study, respectively, which are already defined in the sea level mode solution (4.3) together with buoyancy forcing $B_0 = \frac{B(0)}{\rho_0}$.

Substitution of the above definitions into (4.6) gives

$$\left(\frac{\partial}{\partial t} + \lambda\right) gh + \frac{\beta}{f_0^2}\frac{\partial}{\partial x}\left(gh\int_{-H}^{0} N^2 \int_{-H}^{z} \psi_p dz' dz\right) -$$
$$\frac{\beta}{f_0^2} gh \int_{-H}^{0} \frac{\partial N^2}{\partial x} \int_{-H}^{z} \psi_p dz' dz = W_0 \int_{-H}^{0} N^2 \psi_\tau dz - \frac{gE_0}{f_0^2} \int_{-H}^{0} N^2 \int_{-H}^{z} \psi_E dz' dz - gB_0$$

Define

$$c(x,y) = \frac{\beta}{f_0^2} \int_{-H}^{0} N^2 \int_{-H}^{z} \psi_p dz' dz$$
$$A_\tau(x,y) = \frac{1}{g} \int_{-H}^{0} N^2 \psi_\tau dz$$
$$A_E(x,y) = -\frac{1}{f_0^2} \int_{-H}^{0} N^2 \int_{-H}^{z} \psi_E dz' dz$$
$$A_B(x,y) = -1$$

It follows, then, that

$$\left(\frac{\partial}{\partial t} + \lambda\right) h = -c\frac{\partial h}{\partial x} - h\frac{\partial c}{\partial x} + \frac{\beta h}{f_0^2} \int_{-H}^{0} \frac{\partial N^2}{\partial x} \int_{-H}^{z} \psi_p dz' dz + A_\tau W_0 + A_E E_0 + A_B B_0$$

To estimate scales for the first three terms on the right side of the above equation, a simplified case with constant stratification is examined. For a constant N^2, the first-mode eigenvector is $\cos\left(\frac{\pi z}{H}\right)$. With the eigenvector representing ψ_p, we obtain

$$c = \frac{\beta}{f_0^2}\int_{-H}^{0} N^2 \int_{-H}^{z} \psi_p dz' dz = -\frac{2\beta H^2 N^2}{f_0^2 \pi^2}$$
$$\frac{\beta}{f_0^2}\int_{-H}^{0} \frac{\partial N^2}{\partial x} \int_{-H}^{z} \psi_p dz' dz = -\frac{2\beta H^2}{f_0^2 \pi^2}\frac{\partial N^2}{\partial x}$$

indicating that the term $\frac{\beta h}{f_0^2}\int_{-H}^{0} \frac{\partial N^2}{\partial x} \int_{-H}^{z} \psi_p dz' dz$ has same scale as $h\frac{\partial c}{\partial x}$.

The scale ratio of $h\frac{\partial c}{\partial x}$ to $c\frac{\partial h}{\partial x}$ is expressed by

$$\frac{h\frac{\partial c}{\partial x}}{c\frac{\partial h}{\partial x}} \sim \frac{\frac{1}{c}\frac{\partial c}{\partial x}}{\frac{1}{h}\frac{\partial h}{\partial x}} = \frac{\frac{1}{\left(\frac{\Delta\rho_0}{\rho_0}\right)}\frac{\partial}{\partial x}\left(\frac{\Delta\rho_0}{\rho_0}\right)}{\frac{1}{h}\frac{\partial h}{\partial x}} \sim \frac{L_h}{L_c}$$

where L_h is the zonal length scale of the sea level variation derived from the low-passed SSH anomalies, and L_c is a zonal length scale for the wave speed associated with density changes from the ocean surface to bottom normalized by the mean density that is derived from WOA13 version 2. The zonal scale is calculated using a Fourier Transform.

Sea level, h and its zonal derivative $\frac{\partial h}{\partial x}$ are written as

$$h = \sum_k a_k e^{if_k x}$$
$$\frac{\partial h}{\partial x} = i\sum_k f_k a_k e^{if_k x}$$

The variances are scaled as

$$var(h) \sim \sum_k |a_k|^2$$
$$var(\frac{\partial h}{\partial x}) \sim \sum_k |f_k a_k|^2$$

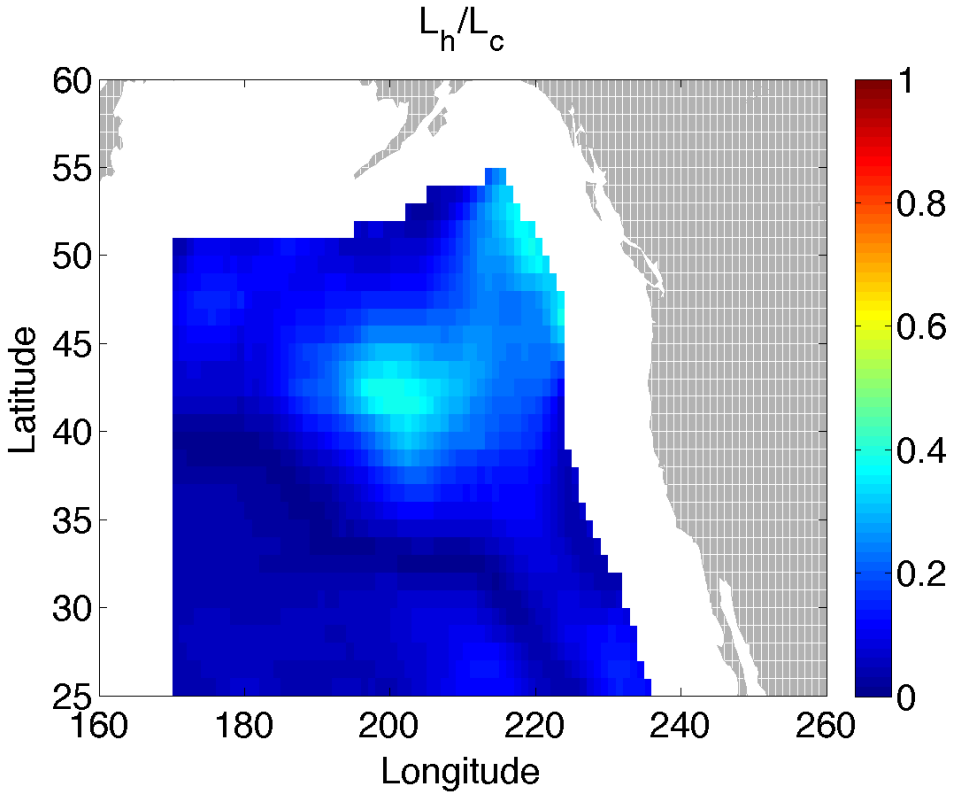

Figure 4.1: Ratio of zonal scale of SSH anomaly, L_h, to zonal scale of wave speed, L_c.

Then zonal length scale L_h is

$$L_h = \left(\frac{\sum_k |a_k|^2}{\sum_k |f_k a_k|^2} \right)^{\frac{1}{2}}$$

L_h is calculated in a zonal moving bin of 21° length. The length scale for the wave speed is calculated in the same way. The scale ratio, $\frac{L_h}{L_c}$, is shown to be less than 0.4 at all grid points and be less than 0.1 at more than half of the grid points (Figure 4.1).

As a result, the following inequality relations hold.

$$h\frac{\partial c}{\partial x} \ll c\frac{\partial h}{\partial x}$$

$$\frac{\beta h}{f_0^2}\int_{-H}^{0}\frac{\partial N^2}{\partial x}\int_{-H}^{z}\psi_p dz'dz \ll c\frac{\partial h}{\partial x}$$

And with the two small terms neglected, we have

$$\left(\frac{\partial}{\partial t}+\lambda\right)h=-c\frac{\partial h}{\partial x}+A_\tau W_0+A_E E_0+A_B B_0 \tag{4.7}$$

which gives the same form as the traditional mode equation (4.3), but presents a novel framework for interpreting the modal equations in terms of an integral solution. As is common in modal solutions, c, λ, A_τ, and A_E can be treated as unknown parameters. A_B, which is -1 in theory, is also allowed to vary because of uncertainties in calculated buoyancy forcing.

The sea level equation (4.7) can be solved by the common MOC method. Following the derivation procedure by Thompson (2012, [107]), the sea level solution is

$$h(x,t)=\frac{h(x_0,t_0)+\int_x^{x_0} q(x',t')e^{\int_{x'}^{x_0}\kappa(x'')dx''}dx'}{e^{\int_x^{x_0}\kappa(x')dx'}} \tag{4.8}$$

where t_0 is initial time, x_0 is eastern boundary, and q, κ and t are respectively defined as

$$q=\frac{A_\tau W_0+A_E E_0+A_B B_0}{c}$$

$$\kappa=\frac{\lambda}{c}$$

$$t=t_0+\int_x^{x_0} c^{-1}(x')dx'$$

Sea level variability in this solution is obtained by integrating three external forcings along wave characteristics.

The alternative approach developed here is to find the optimal solution at each point in space. In the new method, the zonal gradient of sea level is treated like a forcing term and is calculated from the SSH observations. Multiplying $e^{\lambda t}$ on both sides of (4.7), integrating

it from t_0 to t and then multiplying $e^{-\lambda t}$ on both sides yield

$$e^{-\lambda t}\int_{t_0}^{t}\frac{\partial}{\partial t}(he^{\lambda t})dt' = -ce^{-\lambda t}\int_{t_0}^{t}\frac{\partial h}{\partial x}e^{\lambda t'}dt' + A_\tau e^{-\lambda t}\int_{t_0}^{t}W_0 e^{\lambda t'}dt' + A_E e^{-\lambda t}\int_{t_0}^{t}E_0 e^{\lambda t'}dt' + A_B e^{-\lambda t}\int_{t_0}^{t}B_0 e^{\lambda t'}dt'$$

Rearranging the above equation gives

$$h(t) = h(t_0)e^{-\lambda t} - c\int_{t_0}^{t}\frac{\partial h}{\partial x}e^{-\lambda(t-t')}dt' + A_\tau\int_{t_0}^{t}W_0 e^{-\lambda(t-t')}dt' + A_E\int_{t_0}^{t}E_0 e^{-\lambda(t-t')}dt' + A_B\int_{t_0}^{t}B_0 e^{-\lambda(t-t')}dt' \tag{4.9}$$

The sea level variability in this alternative integration is seen to be a damped local response to the forcings, or equivalently, a one-sided smoothing of the forcings, with the damping coefficient taking the role of the smoothing coefficient.

Before exploiting this new method, the approximate order of magnitude of c, A_τ, and A_E are estimated. Given a constant N^2, the related first-mode eigenvector $\cos\left(\frac{\pi z}{H}\right)$ representing ψ_p and assuming $\psi_E = \psi_p^2$, the orders of magnitude of c, A_τ and A_E follow

$$c = \frac{\beta}{f_0^2}\int_{-H}^{0}N^2\int_{-H}^{z}\cos\left(\frac{z\pi}{H}\right)dz'dz = -\frac{2\beta H^2N^2}{f_0^2\pi^2} \sim \frac{10^{-11}\times 10^7\times 10^{-5}}{10^{-8}\times 10}\ m/s = 10^{-2}\ m/s$$

$$A_\tau = \frac{N^2}{g}\int_{-H}^{0}\psi_\tau dz \sim \frac{\Delta\rho}{\rho_0} \sim 10^{-3}$$

$$A_E = -\frac{1}{f_0^2}N^2\int_{-H}^{0}\int_{-H}^{z}\cos^2(\frac{z\pi}{H})dz'dz \sim \frac{H^2N^2}{4f_0^2} \sim \frac{10^6\times 10^{-5}}{10^{-8}}\ m^2 = 10^3\ km^2$$

The estimated scales are consistent with those shown in mode equation (4.3). Propagation is dominantly westward so that c is negative; Ekman upwelling with positive W_0 induces low sea level, while Ekman downwelling with negative W_0 induces high sea level, indicating that the sign of A_τ is negative; positive vorticity advection with positive E_0 causes high sea level,

Table 4.1: Range of model parameters for MOC solution

Parameter	Domain	Interval
Wind forcing coefficient	$-5 \times 10^{-3} <= A_\tau <= 0$	0.5×10^{-3}
Eddy forcing coefficient	$0 <= A_E <= 1.5L_1^2$ where L_1 is first-mode Rossby deformation radius	$0.25L_1^2$
Buoyancy forcing coefficient	$-2 <= A_B <= 0$	0.5
Propagation velocity	$3c_R <= c < 0$ where c_R is standard first-mode Rossby wave velocity	$0.25c_R$
Damping coefficient	$\frac{1}{72}month^{-1} <= \lambda <= 1month^{-1}$	$\frac{1}{6}month^{-1}$

while negative vorticity advection with negative E_0 causes low sea level, indicating that the sign of A_E is positive.

4.3 Results

4.3.1 Sea level solution by MOC

With the unknown forcing coefficients, propagation velocity, and damping coefficient, the sea level solution by MOC (equation 4.8) is fitted to observed SSH anomalies, following the fitting approach proposed by Thompson (2012, [107]). Based on typical magnitudes of these parameters, searching domains of model parameters are given in Table 4.1, and only meridional variation of parameters is allowed in the fitting. The modeled sea level and optimal parameters are found by minimizing variance of sea level difference between model and observation at each latitude. The model performance is measured by correlation and ratio of unexplained sea level variance to observed sea level variance.

Figure 4.2 shows high correlation and low unexplained sea level variance largely in a band extending from southwest to northeast. Although the model solution has better performance in the southwest corner of NP than the model results obtained by Thompson (2012, [107]), sea level variability in the southeast and northwest of NP cannot be accounted for by this

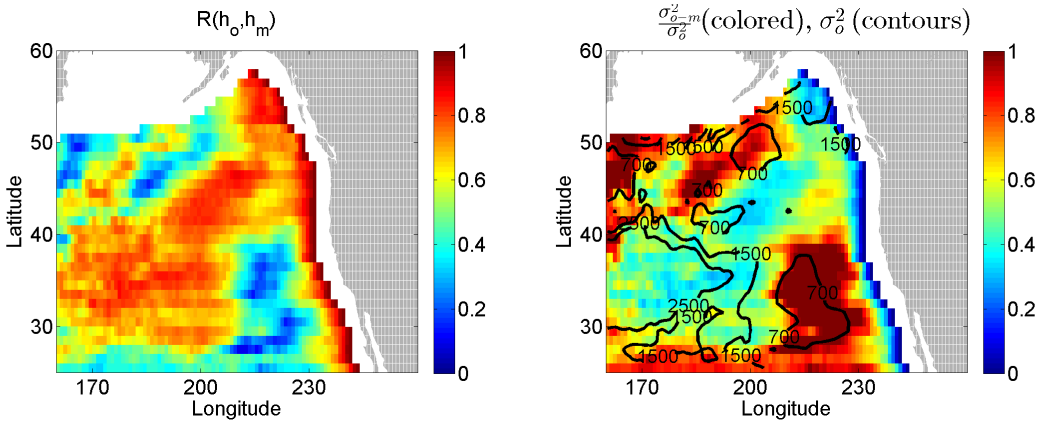

Figure 4.2: Correlation between observed and modeled sea level anomalies (left); Ratio of variance of difference between modeled and observed sea level anomalies to variance of observation (right). Contours represent variance of observed sea level anomalies. The model is solved by MOC method.

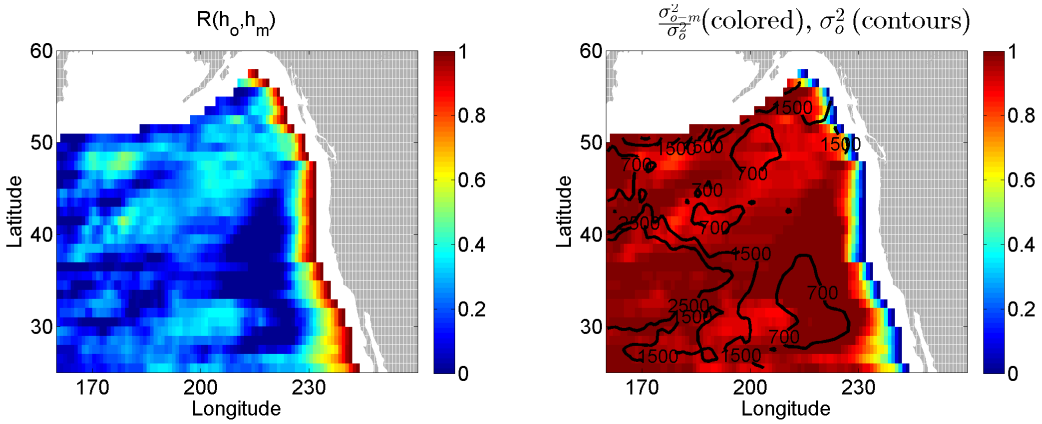

Figure 4.3: Same as Figure 4.2, but modeled sea level anomalies result from the eastern boundary.

model solution. The contribution to modeled sea level from each forcing component is then calculated based on the optimal parameters.

Higher correlation and less unexplained sea level variance are also observed along the eastern boundary, but the sea level anomalies originating from the eastern boundary are mainly limited to within few degrees away from the eastern boundary with minor influence away from the boundary (Figure 4.3). This resembles the spatial correlation pattern owing to the boundary-driven Rossby waves in the study by Fu and Qiu (2002 [106]). Away from the eastern boundary, however, the sea level variability is overwhelmed by the external forcing

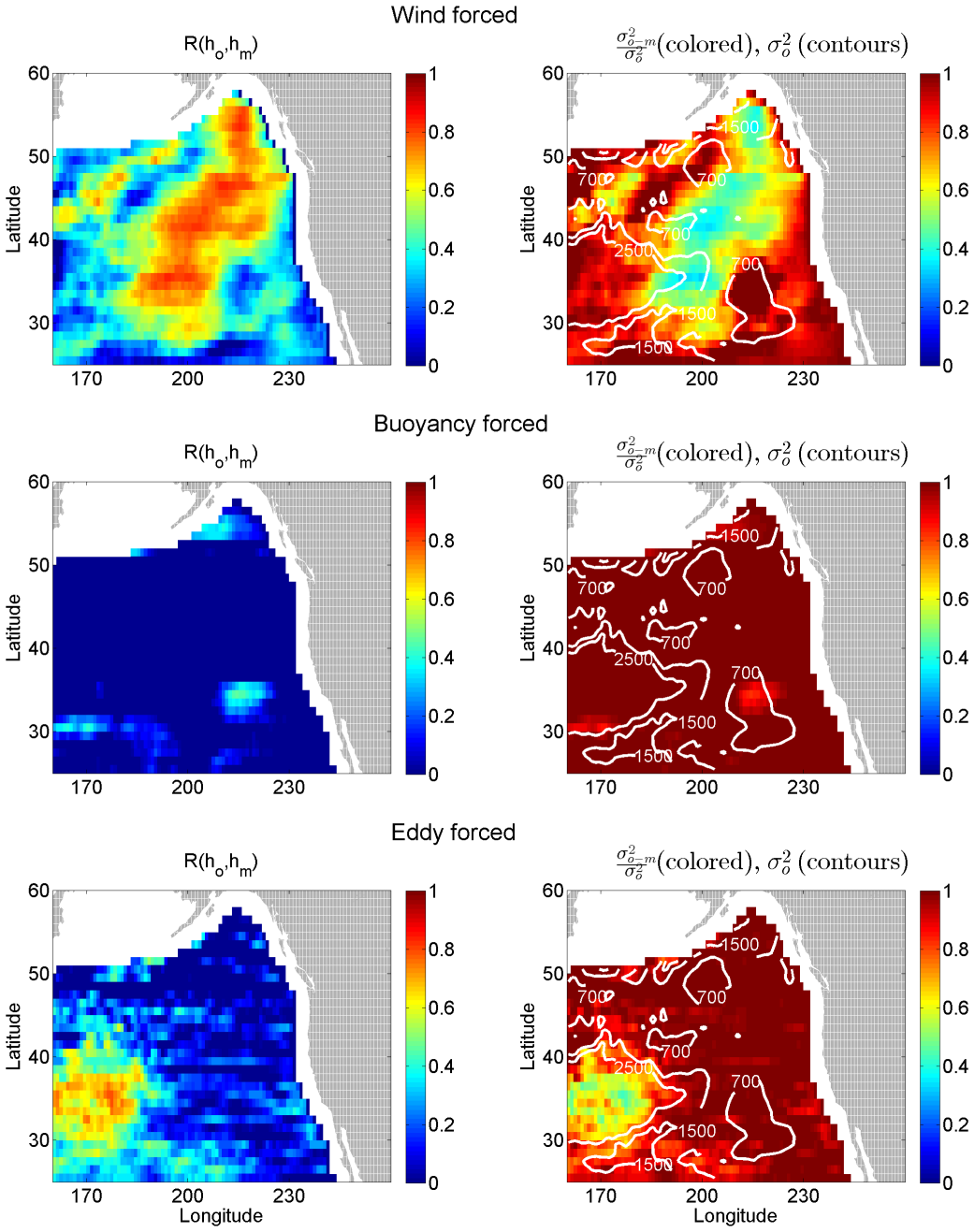

Figure 4.4: Same as Figure 4.2, but modeled sea level anomalies result from wind, buoyancy and eddy forcing respectively.

terms. The roles of wind, buoyancy and eddy forcing in driving sea level variations are exhibited in Figure 4.4. Wind and eddy forcings are the dominant driving forcings in a band

from the central to northeast part of NP and in the southwest corner of NP, respectively, while buoyancy forcing does not have any substantial contribution in this solution.

The failure of the MOC solution over some regions is probably related to two factors. First, the MOC solution needs wave propagation to integrate external forcing, which might fail in places where wave propagation is not important. Second, zonal variation of model parameters is not used in the fitting because Thompson (2012, [107]) showed that this did not improve the results. Our new sea level solution (equation 4.9) via local temporal integration (LTI) is examined in the next section to see if we can improve on the MOC results.

4.3.2 Sea level solution by LTI

The LTI solution (equation 4.9), presented above, has the form of a regression model with the observed SSH as the dependent variable, the integration terms being independent variables, and the forcing coefficients and the wave speed being the model parameters. Given a damping coefficient, the model parameters are obtained by least square fitting and the best fit is obtained by varying the damping coefficient to find the global minimum solution. The LTI solution gives spatial patterns of the model parameters and includes both traveling and standing sea level signals, while MOC solution only allows traveling signal.

With the wind, buoyancy, eddy forcing and sea level zonal gradient derived from observation, the LTI solution 4.9 is fitted to the observed sea level anomalies at every grid point, yielding modeled sea level, propagation velocity, damping and forcing coefficients. The solution performance is again described by the correlation and the unexplained variance ratio as shown in Figure 4.5. At more than 87% of grid points with valid data, the correlation between fitted and observed sea level exceed 0.6, suggesting good performance of the regression model. At the points with a correlation larger than 0.6, more than 50% of variance can be accounted for by the model solution. Comparing Figure 4.2 and Figure 4.5 suggests that the LTI solution gives better model performances than the MOC solution in both correlation and explained variance.

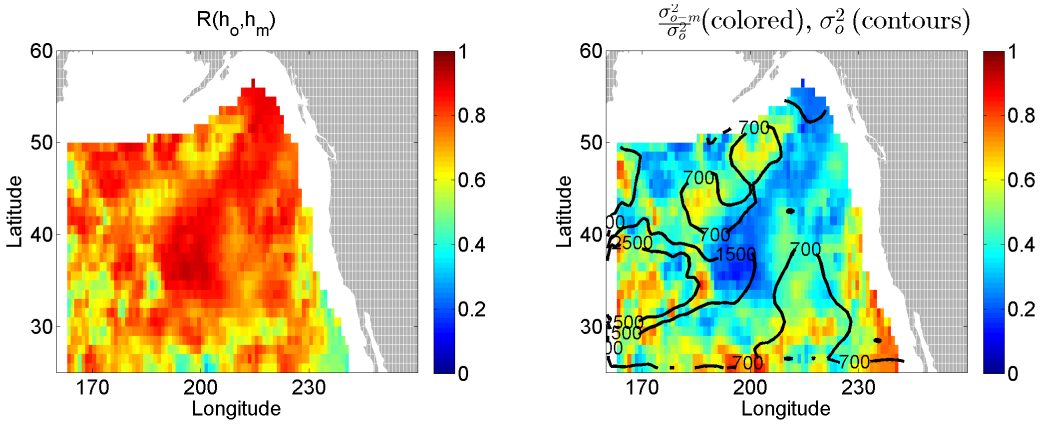

Figure 4.5: Same as Figure 4.2, but the model is solved by the LTI method.

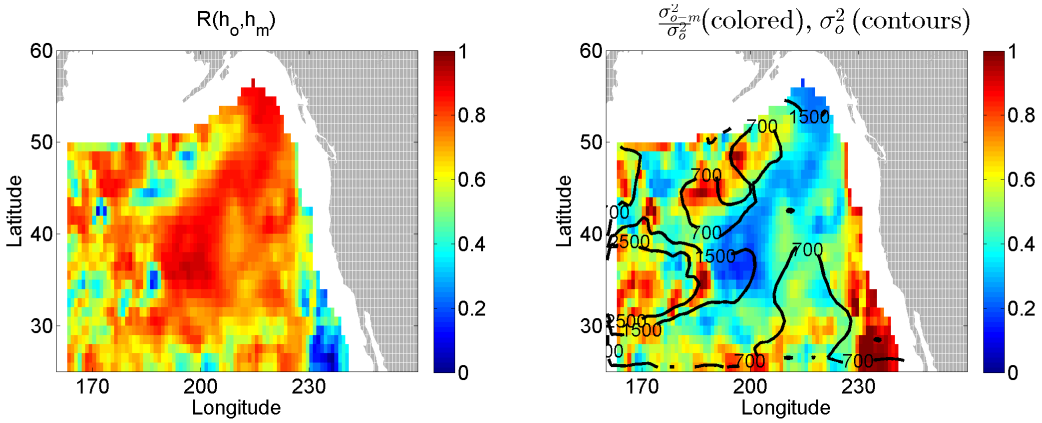

Figure 4.6: Same as Figure 4.5, but the model parameters are smoothed.

It is possible that the improved performance of the LTI solution might result from over-fitting because the model parameters can be different from point to point in space. To test this idea, the parameters are then smoothed with the same filter with half-amplitude scale at 450 km as that used to smooth SSH anomalies and forcing in the MOC solution, which should result in the same or fewer number of degrees. With the smoothed parameters, the LTI solution still shows model performance that is generally superior to the MOC solution (Figure 4.6), suggesting a robust result. We would argue that the LTI solution is worthy of further diagnosis of the large-scale, low-frequency sea level variability in the NP.

Maps of the magnitude of the smoothed forcing coefficients, propagation velocity and damping time are shown in Figure 4.7. Spatial variations of model parameters indicate that each forcing component contributes to the sea level variation in different regions. Relatively

large magnitude of the wind forcing coefficient extends from southwest to northeast, whereas the magnitude is small in the northwest and southeast region, suggesting weak response to wind forcing. The eddy forcing coefficient is most prominent in the west int he region effected by the North Pacific current. The buoyancy forcing coefficient is mostly close to zero but has relatively large magnitude confined to the southeast region. The resulting propagation is slow and even approaches zero in the east and north, but it is faster in the southwest. The optimal damping timescale, which is the inverse of the damping coefficient λ, is below 36 months at more than 90% of grid points, whereas large values area only found in the southeast corner around $220°E$ and the south of Alaska Peninsula where the model is less successful. The propagation speed generally decreases with latitude, as expected, and from west to east, which has implications for the role of propagating signals.

The LTI solution shows that the low-frequency sea level response can be described as the summation of the local damping of wind, eddy, buoyancy forcing and propagation term, but the interpretation is complicated if there are correlations between the forcing terms. Figure 4.8 shows that correlations between the forcing terms are small at the majority of grid points, except for the eddy forcing and propagation term. Although wind forcing can correlate with the buoyancy forcing and the propagation term, the correlations are less than 0.5 and in relatively small areas. On the other hand the eddy forcing and the propagation term are correlated over a large region with correlations greater than 0.5 in smaller regions. In these regions the propagation is likely more important. The high correlation between eddy forcing and propagation term suggests that they cannot be separated when analyzing their contributions to sea level variability.

In order to show the contribution to sea level variation from each forcing components, the correlation between each sea level contribution and the total modeled sea level and the unexplained variance ratio are shown in Figure 4.9. Local wind forcing is the dominant driving force from the central to northeast NP. The correlation pattern agrees well with that found in previous studies using the first-mode Rossby wave model or local one-dimension

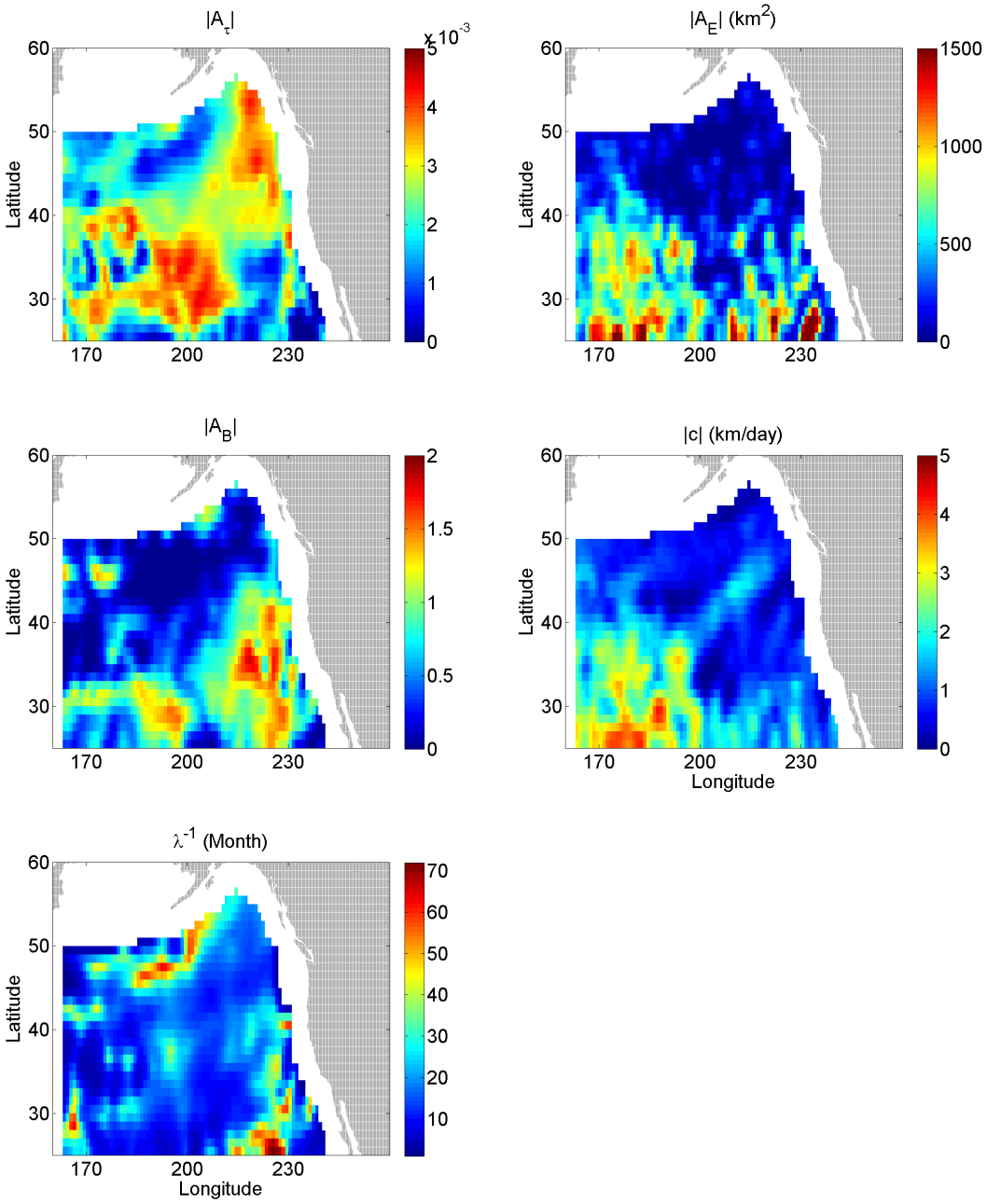

Figure 4.7: Smoothed coefficient magnitude of wind forcing (A_τ, unitless), eddy forcing (A_E, km^2), buoyancy forcing (A_B, unitless), propagation speed (c, km/day), and damping time (λ^{-1}, month).

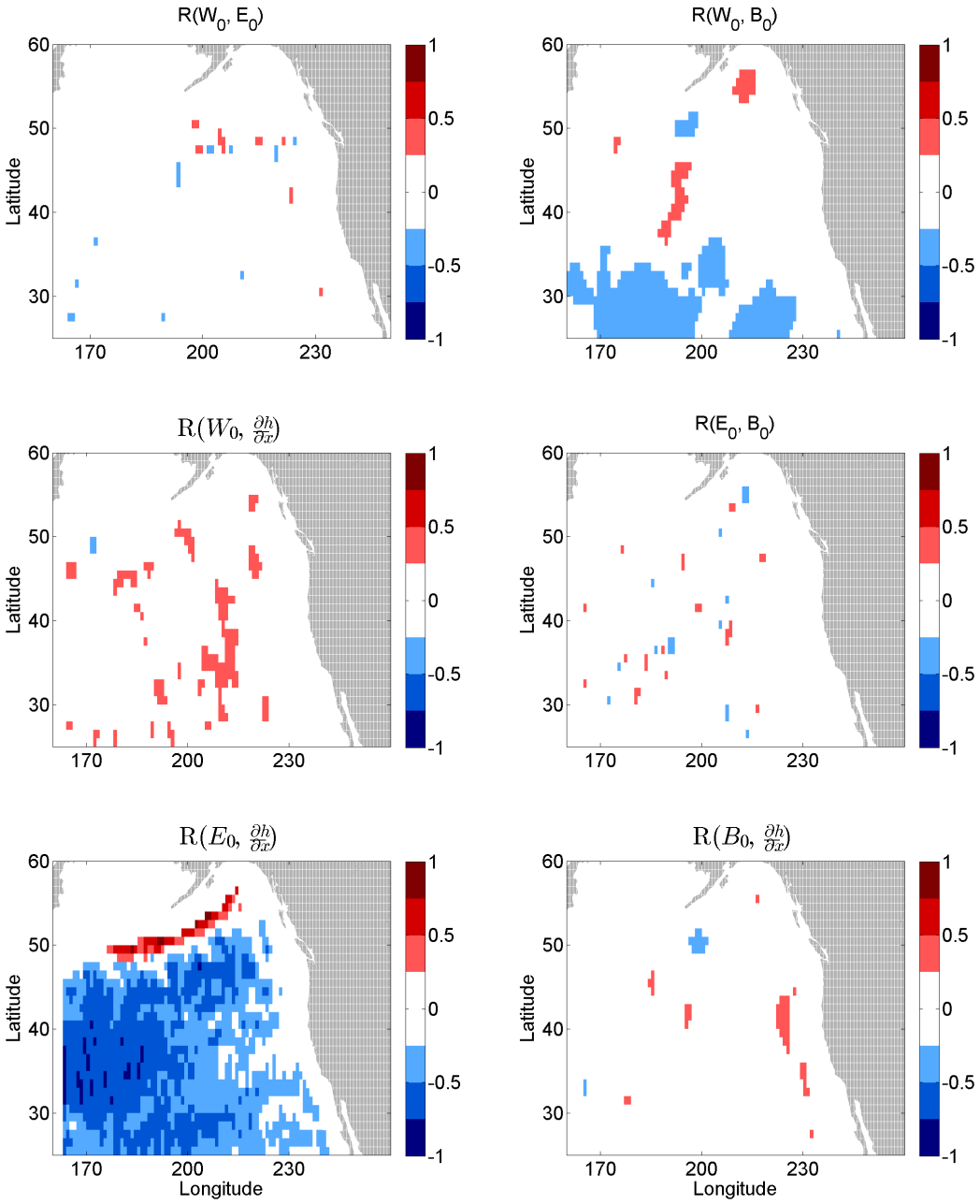

Figure 4.8: Correlations between every pair of forcing terms.

damping model (e.g. Fu and Qiu, 2002 [106]; Cummins and Lagerloef, 2004 [22]). The local response of sea level anomalies to the wind stress curl replicates most variability obtained with the more general model that includes wave propagation. In addition to wind stress curl, buoyancy forcing was suggested to be a driving force of sea level anomalies in earlier studies (Thompson and Ladd, 2004 [25]; Thompson and Dawe, 2007 [109]). In this study, a local response of sea level to buoyancy forcing is seen in the southeast portion of the NP between $210°E$ and $230°E$. A relatively weak response at midlatitudes around $190°E$ is also observed.

4.4 Conclusion

Large-scale, low-frequency sea level variability in the Northeast Pacific is investigated with a newly developed diagnostic sea level model driven by wind, buoyancy and eddy force that does not require a vertical normal mode expansion. This sea level model is solved both by the traditional method of characteristics method and by a new method, which we refer to as a local temporal integration (LTI). The LTI solution simulates the data better than the MOC model.

Wind stress curl, buoyancy and eddy forcing all contribute to sea level variability but play dominant roles in different regions. Sea level anomalies are primarily controlled by local wind forcing in the central to northeast of portion of our study region, by local buoyancy forcing in the southeast region between $210°E$ and $230°E$, and by eddy forcing and wave propagation in the west of NP.

Over most of our study area, the new diagnostic model suggests that local damping rather than Rossby wave propagation does a better job of accounting for the observed sea level changes. One exception is in the southeast portion of our study region where it appears that eddy stresses associated with propagating eddies are reproduced better with the MOC model that depends on propagation. An interesting subject for future work is why our new model, which includes propagation, fails in this region.

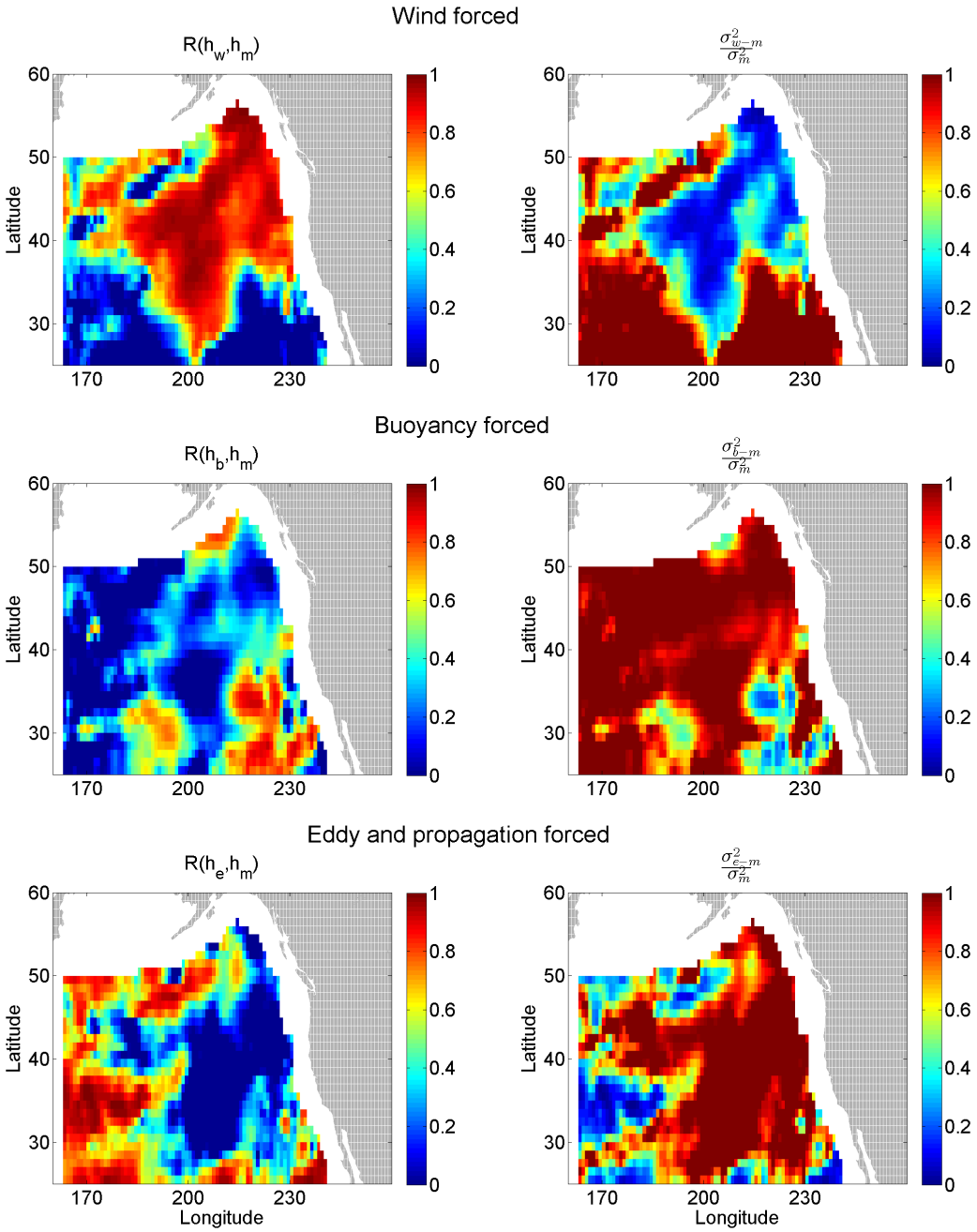

Figure 4.9: Correlation between sea level contributions and total modeled sea level (left); Ratio of variance of difference between sea level contribution and total modeled sea level to variance of observation (right). The upper, middle and bottom panel is for the sea level contributions from wind forcing, buoyancy forcing, eddy and wave propagation forcing, respectively.

References

[1] John A. Church and Neil J. White. Sea-level rise from the late 19th to the early 21st century. *Surveys in Geophysics*, 32(4):585–602, Sep 2011.

[2] J.A. Church, P.U. Clark, A. Cazenave, J.M. Gregory, S. Jevrejeva, A. Levermann, M.A. Merrifield, G.A. Milne, R.S. Nerem, P.D. Nunn, A.J. Payne, W.T. Pfeffer, D. Stammer, and A.S. Unnikrishnan. *Sea Level Change*, book section 13, pages 1137–1216. Cambridge University Press, Cambridge, United Kingdom and New York, NY, USA, 2013.

[3] Dudley B. Chelton and Michael G. Schlax. Global observations of oceanic rossby waves. *Science*, 272(5259):234–238, 1996.

[4] Dudley B. Chelton, Michael G. Schlax, and Roger M. Samelson. Global observations of nonlinear mesoscale eddies. *Progress in Oceanography*, 91(2):167 – 216, 2011.

[5] Fabrice Bonjean and Gary S. E. Lagerloef. Diagnostic model and analysis of the surface currents in the tropical pacific ocean. *Journal of Physical Oceanography*, 32(10):2938–2954, 2002.

[6] Kathryn A. Kelly, LuAnne Thompson, and John Lyman. The coherence and impact of meridional heat transport anomalies in the atlantic ocean inferred from observations. *Journal of Climate*, 27(4):1469–1487, 2014.

[7] John A. Church and Neil J. White. A 20th century acceleration in global sea-level rise. *Geophysical Research Letters*, 33(1):n/a–n/a, 2006. L01602.

[8] M. A. Merrifield, S. T. Merrifield, and G. T. Mitchum. An anomalous recent acceleration of global sea level rise. *Journal of Climate*, 22(21):5772–5781, 2009.

[9] S. J. Holgate and P. L. Woodworth. Evidence for enhanced coastal sea level rise during the 1990s. *Geophysical Research Letters*, 31(7):n/a–n/a, 2004. L07305.

[10] Neil J. White, John A. Church, and Jonathan M. Gregory. Coastal and global averaged sea level rise for 1950 to 2000. *Geophysical Research Letters*, 32(1):n/a–n/a, 2005. L01601.

[11] B. G. Hong, W. Sturges, and Allan J. Clarke. Sea level on the u.s. east coast: Decadal variability caused by open ocean wind-curl forcing. *Journal of Physical Oceanography*, 30(8):2088–2098, 2000.

[12] Asbury H. Sallenger, Kara S. Doran, and Peter A. Howd. Hotspot of accelerated sea-level rise on the atlantic coast of north america. *Nature Climate Change*, 2(12):884, 2012.

[13] D. B. Enfield and J. S. Allen. On the structure and dynamics of monthly mean sea level anomalies along the pacific coast of north and south america. *Journal of Physical Oceanography*, 10(4):557–578, 1980.

[14] Tatsuo Suzuki and Masayoshi Ishii. Long-term regional sea level changes due to variations in water mass density during the period 19812007. *Geophysical Research Letters*, 38(21):n/a–n/a, 2011. L21604.

[15] Gal Forget and Rui M. Ponte. The partition of regional sea level variability. *Progress in Oceanography*, 137(Part A):173 – 195, 2015.

[16] Patrick F. Cummins, Gary S. E. Lagerloef, and Gary Mitchum. A regional index of northeast pacific variability based on satellite altimeter data. *Geophysical Research Letters*, 32(17):n/a–n/a, 2005. L17607.

[17] E. Di Lorenzo, N. Schneider, K. M. Cobb, P. J. S. Franks, K. Chhak, A. J. Miller, J. C. McWilliams, S. J. Bograd, H. Arango, E. Curchitser, T. M. Powell, and P. Rivire. North pacific gyre oscillation links ocean climate and ecosystem change. *Geophysical Research Letters*, 35(8):n/a–n/a, 2008. L08607.

[18] Frédéric Vivier, Kathryn A. Kelly, and LuAnne Thompson. Contributions of wind forcing, waves, and surface heating to sea surface height observations in the pacific ocean. *Journal of Geophysical Research: Oceans*, 104(C9):20767–20788, 1999.

[19] Cécile Cabanes, Thierry Huck, and Alain Colin de Verdière. Contributions of wind forcing and surface heating to interannual sea level variations in the atlantic ocean. *Journal of Physical Oceanography*, 36(9):1739–1750, 2006.

[20] Gary S. E. Lagerloef. Interdecadal variations in the alaska gyre. *Journal of Physical Oceanography*, 25(10):2242–2258, 1995.

[21] Bo Qiu. Large-scale variability in the midlatitude subtropical and subpolar north pacific ocean: Observations and causes. *Journal of Physical Oceanography*, 32(1):353–375, 2002.

[22] Patrick F. Cummins and Gary S.E. Lagerloef. Wind-driven interannual variability over the northeast pacific ocean. *Deep Sea Research Part I: Oceanographic Research Papers*, 51(12):2105 – 2121, 2004.

[23] Antonietta Capotondi, Michael A. Alexander, Clara Deser, and Arthur J. Miller. Low-frequency pycnocline variability in the northeast pacific. *Journal of Physical Oceanography*, 35(8):1403–1420, 2005.

[24] Antonietta Capotondi, Vincent Combes, Michael A. Alexander, Emanuele Di Lorenzo, and Arthur J. Miller. Low-frequency variability in the gulf of alaska from coarse and eddy-permitting ocean models. *Journal of Geophysical Research: Oceans*, 114(C1):n/a–n/a, 2009. C01017.

[25] Lu Anne Thompson and Carol A. Ladd. The response of the north pacific ocean to decadal variability in atmospheric forcing: Wind versus buoyancy forcing. *Journal of Physical Oceanography*, 34(6):1373–1386, 2004.

[26] Bo Qiu, Shuiming Chen, Lixin Wu, and Shinichiro Kida. Wind- versus eddy-forced regional sea level trends and variability in the north pacific ocean. *Journal of Climate*, 28(4):1561–1577, 2015.

[27] Bruce C. Douglas. Global sea level rise. *Journal of Geophysical Research: Oceans*, 96(C4):6981–6992, 1991.

[28] D. P. Chambers, C. A. Mehlhaff, T. J. Urban, D. Fujii, and R. S. Nerem. Low-frequency variations in global mean sea level: 1950-2000. *Journal of Geophysical Research: Oceans*, 107(C4):1–1–1–10, 2002.

[29] S. Jevrejeva, J. C. Moore, A. Grinsted, and P. L. Woodworth. Recent global sea level acceleration started over 200 years ago? *Geophysical Research Letters*, 35(8):n/a–n/a, 2008. L08715.

[30] G. Wöppelmann, C. Letetrel, A. Santamaria, M.-N. Bouin, X. Collilieux, Z. Altamimi, S. D. P. Williams, and B. Martin Miguez. Rates of sea-level change over the past century in a geocentric reference frame. *Geophysical Research Letters*, 36(12):n/a–n/a, 2009. L12607.

[31] Richard D. Ray and Bruce C. Douglas. Experiments in reconstructing twentieth-century sea levels. *Progress in Oceanography*, 91(4):496 – 515, 2011.

[32] F. M. Calafat, D. P. Chambers, and M. N. Tsimplis. On the ability of global sea level reconstructions to determine trends and variability. *Journal of Geophysical Research: Oceans*, 119(3):1572–1592, 2014.

[33] Carling C. Hay, Eric Morrow, Robert E. Kopp, and Jerry X. Mitrovica. Probabilistic reanalysis of twentieth-century sea-level rise. *Nature*, 517(7535):481, 2015.

[34] Philip L. Woodworth, Melisa Menéndez, and W. Roland Gehrels. Evidence for century-timescale acceleration in mean sea levels and for recent changes in extreme sea levels. *Surveys in Geophysics*, 32(4):603–618, Sep 2011.

[35] S. Jevrejeva, J.C. Moore, A. Grinsted, A.P. Matthews, and G. Spada. Trends and acceleration in global and regional sea levels since 1807. *Global and Planetary Change*, 113(Supplement C):11 – 22, 2014.

[36] S. Jevrejeva, A. Grinsted, J. C. Moore, and S. Holgate. Nonlinear trends and multiyear cycles in sea level records. *Journal of Geophysical Research: Oceans*, 111(C9):n/a–n/a, 2006. C09012.

[37] S. J. Holgate. On the decadal rates of sea level change during the twentieth century. *Geophysical Research Letters*, 34(1):n/a–n/a, 2007. L01602.

[38] P. L. Woodworth, N. J. White, S. Jevrejeva, S. J. Holgate, J. A. Church, and W. R. Gehrels. Evidence for the accelerations of sea level on multi-decade and century timescales. *International Journal of Climatology*, 29(6):777–789, 2009.

[39] JA Church, NJ White, and JM Arblaster. Significant decadal-scale impact of volcanic eruptions on sea level and ocean heat content. *NATURE*, 438(7064):74–77, NOV 3 2005.

[40] Don P. Chambers, Mark A. Merrifield, and R. Steven Nerem. Is there a 60-year oscillation in global mean sea level? *Geophysical Research Letters*, 39(18):n/a–n/a, 2012. L18607.

[41] M. S. Bos, S. D. P. Williams, I. B. Arajo, and L. Bastos. The effect of temporal correlated noise on the sea level rate and acceleration uncertainty. *Geophysical Journal International*, 196(3):1423–1430, 2014.

[42] F. M. Calafat and D. P. Chambers. Quantifying recent acceleration in sea level unrelated to internal climate variability. *Geophysical Research Letters*, 40(14):3661–3666, 2013.

[43] B. D. Hamlington, R. R. Leben, M. W. Strassburg, R. S. Nerem, and K.-Y. Kim. Contribution of the pacific decadal oscillation to global mean sea level trends. *Geophysical Research Letters*, 40(19):5171–5175, 2013.

[44] Ivan D. Haigh, Thomas Wahl, Eelco J. Rohling, Ren M. Price, Charitha B. Pattiaratchi, Francisco M. Calafat, and Snke Dangendorf. Timescales for detecting a significant acceleration in sea level rise. *Nature Communications*, 5(4):3635, 2014.

[45] B. D. Beckley, F. G. Lemoine, S. B. Luthcke, R. D. Ray, and N. P. Zelensky. A reassessment of global and regional mean sea level trends from topex and jason-1 altimetry based on revised reference frame and orbits. *Geophysical Research Letters*, 34(14):n/a–n/a, 2007. L14608.

[46] G. Jordà. Detection time for global and regional sea level trends and accelerations. *Journal of Geophysical Research: Oceans*, 119(10):7164–7174, 2014.

[47] R. S. Nerem and G. T. Mitchum. Estimates of vertical crustal motion derived from differences of topex/poseidon and tide gauge sea level measurements. *Geophysical Research Letters*, 29(19):40–1–40–4, 2002. 1934.

[48] Ailin Mao, Christopher G. A. Harrison, and Timothy H. Dixon. Noise in gps coordinate time series. *Journal of Geophysical Research: Solid Earth*, 104(B2):2797–2816, 1999.

[49] M. Becker, M. Karpytchev, and S. Lennartz-Sassinek. Long-term sea level trends: Natural or anthropogenic? *Geophysical Research Letters*, 41(15):5571–5580, 2014. 2014GL061027.

[50] M. Ghil, M. R. Allen, M. D. Dettinger, K. Ide, D. Kondrashov, M. E. Mann, A. W. Robertson, A. Saunders, Y. Tian, F. Varadi, and P. Yiou. Advanced spectral methods for climatic time series. *Reviews of Geophysics*, 40(1):3–1–3–41, 2002.

[51] Victor Ocaña, Eduardo Zorita, and Patrick Heimbach. Stochastic secular trends in sea level rise. *Journal of Geophysical Research: Oceans*, 121(4):2183–2202, 2016.

[52] Simon D. P. Williams and Pascal Willis. Error analysis of weekly station coordinates in the doris network. *Journal of Geodesy*, 80(8):525–539, Nov 2006.

[53] Kara J. Doran. *Addressing the problem of land motion at tide gauges. [electronic resource].* [Tampa, Fla.] : University of South Florida, 2010., 2010.

[54] Chris W. Hughes and Simon D. P. Williams. The color of sea level: Importance of spatial variations in spectral shape for assessing the significance of trends. *Journal of Geophysical Research: Oceans*, 115(C10):n/a–n/a, 2010. C10048.

[55] Peter Diggle. *Time series : a biostatistical introduction.* Oxford statistical science series: 5. Oxford [England] : Clarendon Press ; New York : Oxford University Press, 1990., 1990.

[56] M.B. Priestley. *Spectral Analysis and Time Series*. Number v. 1-2 in Probability and mathematical statistics. Academic Press, 1981.

[57] Thomas C.M Lee and Tan F Wong. Nonparametric log spectrum estimation using disconnected regression splines and genetic algorithms. *Signal Processing*, 83:79 – 90, 2003.

[58] Barry Ruddick, Ayal Anis, and Keith Thompson. Maximum likelihood spectral fitting: The batchelor spectrum. *Journal of Atmospheric and Oceanic Technology*, 17(11):1541–1555, 2000.

[59] F. N. Fritsch and R. E. Carlson. Monotone piecewise cubic interpolation. *SIAM Journal on Numerical Analysis*, 17(2):238–246, 1980.

[60] Wesley Ebisuzaki. A method to estimate the statistical significance of a correlation when the data are serially correlated. *Journal of Climate*, 10(9):2147–2153, 1997.

[61] Joong-Ho Won, Johan Lim, Seung-Jean Kim, and Bala Rajaratnam. Condition-number-regularized covariance estimation. *Journal of the Royal Statistical Society: Series B (Statistical Methodology)*, 75(3):427–450, 2013.

[62] Pierre Prandi, Anny Cazenave, and Mlanie Becker. Is coastal mean sea level rising faster than the global mean? a comparison between tide gauges and satellite altimetry over 19932007. *Geophysical Research Letters*, 36(5):n/a–n/a, 2009. L05602.

[63] K. Richter, R.E.M. Riva, and H. Drange. Impact of self-attraction and loading effects induced by shelf mass loading on projected regional sea level rise. *Geophysical Research Letters*, 40(6):1144–1148, 2013.

[64] Jianjun Yin, Stephen M. Griffies, and Ronald J. Stouffer. Spatial variability of sea level rise in twenty-first century projections. *Journal of Climate*, 23(17):4585–4607, 2010.

[65] Rory J. Bingham and Chris W. Hughes. Signature of the atlantic meridional overturning circulation in sea level along the east coast of north america. *Geophysical Research Letters*, 36(2):n/a–n/a, 2009. L02603.

[66] Sergey V. Vinogradov and Rui M. Ponte. Annual cycle in coastal sea level from tide gauges and altimetry. *Journal of Geophysical Research: Oceans*, 115(C4):n/a–n/a, 2010. C04021.

[67] Sergey V. Vinogradov and Rui M. Ponte. Low-frequency variability in coastal sea level from tide gauges and altimetry. *Journal of Geophysical Research: Oceans*, 116(C7):n/a–n/a, 2011. C07006.

[68] R. J. Bingham and C. W. Hughes. Local diagnostics to estimate density-induced sea level variations over topography and along coastlines. *Journal of Geophysical Research: Oceans*, 117(C1):n/a–n/a, 2012. C01013.

[69] F. M. Calafat, D. P. Chambers, and M. N. Tsimplis. Mechanisms of decadal sea level variability in the eastern north atlantic and the mediterranean sea. *Journal of Geophysical Research: Oceans*, 117(C9):n/a–n/a, 2012. C09022.

[70] M. Andres, G. G. Gawarkiewicz, and J. M. Toole. Interannual sea level variability in the western north atlantic: Regional forcing and remote response. *Geophysical Research Letters*, 40(22):5915–5919, 2013. 2013GL058013.

[71] Philip L. Woodworth, Miguel Á. Morales Maqueda, Vassil M. Roussenov, Richard G. Williams, and Chris W. Hughes. Mean sea-level variability along the northeast american atlantic coast and the roles of the wind and the overturning circulation. *Journal of Geophysical Research: Oceans*, 119(12):8916–8935, 2014.

[72] S. Higginson, K. R. Thompson, P. L. Woodworth, and C. W. Hughes. The tilt of mean sea level along the east coast of north america. *Geophysical Research Letters*, 42(5):1471–1479, 2015.

[73] William Hsieh and Kirk Bryan. Redistribution of sea level rise associated with enhanced greenhouse warming: a simple model study. *Climate Dynamics*, 12(8):535, 1996.

[74] Xiaoming Zhai, Helen L. Johnson, and David P. Marshall. A model of atlantic heat content and sea level change in response to thermohaline forcing. *Journal of Climate*, 24(21):5619–5632, 2011.

[75] Hiroshi Uchida and Shiro Imawaki. Estimation of the sea level trend south of japan by combining satellite altimeter data with in situ hydrographic data. *Journal of Geophysical Research: Oceans*, 113(C9):n/a–n/a, 2008. C09035.

[76] Paul Sterlini, Dewi Le Bars, Hylke de Vries, and Nina Ridder. Understanding the spatial variation of sea level rise in the north sea using satellite altimetry. *Journal of Geophysical Research: Oceans*, 122(8):6498–6511, 2017.

[77] W.R. Peltier. Global glacial isostasy and the surface of the ice-age earth: The ice-5g (vm2) model and grace. *Annual Review of Earth and Planetary Sciences*, 32(1):111–149, 2004.

[78] Gary T. Mitchum. An improved calibration of satellite altimetric heights using tide gauge sea levels with adjustment for land motion. *Marine Geodesy*, 23(3):145–166, 2000.

[79] Simon J. Holgate, Andrew Matthews, Philip L. Woodworth, Lesley J. Rickards, Mark E. Tamisiea, Elizabeth Bradshaw, Peter R. Foden, Kathleen M. Gordon, Svetlana Jevrejeva, and Jeff Pugh. New data systems and products at the permanent service for mean sea level. *Journal of Coastal Research*, pages 493–504, 2013.

[80] Alvaro Santamaría-Gómez, Médéric Gravelle, Sönke Dangendorf, Marta Marcos, Giorgio Spada, and Guy Wöppelmann. Uncertainty of the 20th century sea-level rise due to vertical land motion errors. *Earth and Planetary Science Letters*, 473(Supplement C):24 – 32, 2017.

[81] W. R. Peltier, D. F. Argus, and R. Drummond. Space geodesy constrains ice age terminal deglaciation: The global ice-6g_c (vm5a) model. *Journal of Geophysical Research: Solid Earth*, 120(1):450–487, 2015.

[82] L. Zawadzki, M. Ablain, L. Carrere, R. D. Ray, N. P. Zelensky, F. Lyard, A. Guillot, and N. Picot. Reduction of the 59-day error signal in the mean sea level derived from topex/poseidon, jason-1 and jason-2 data with the latest fes and got ocean tide models. *Ocean Science Discussions*, 2016:1–20, 2016.

[83] Matt A. King, Maxim Keshin, Pippa L. Whitehouse, Ian D. Thomas, Glenn Milne, and Riccardo E. M. Riva. Regional biases in absolute sea-level estimates from tide gauge data due to residual unmodeled vertical land movement. *Geophysical Research Letters*, 39(14), 2012.

[84] Émilie Ostanciaux, Laurent Husson, Gaël Choblet, Cécile Robin, and Kevin Pedoja. Present-day trends of vertical ground motion along the coast lines. *Earth-Science Reviews*, 110(1):74 – 92, 2012.

[85] B. D. Hamlington, P. Thompson, W. C. Hammond, G. Blewitt, and R. D. Ray. Assessing the impact of vertical land motion on twentieth century global mean sea level estimates. *Journal of Geophysical Research: Oceans*, 121(7):4980–4993, 2016.

[86] Dana J. Caccamise, Mark A. Merrifield, Michael Bevis, James Foster, Yvonne L. Firing, Mark S. Schenewerk, Frederick W. Taylor, and Donald A. Thomas. Sea level rise at honolulu and hilo, hawaii: Gps estimates of differential land motion. *Geophysical Research Letters*, 32(3), 2005.

[87] M. N. Bouin and G. Wöppelmann. Land motion estimates from gps at tide gauges: a geophysical evaluation. *Geophysical Journal International*, 180(1):193–209, 2010.

[88] M. Becker, B. Meyssignac, C. Letetrel, W. Llovel, A. Cazenave, and T. Delcroix. Sea level variations at tropical pacific islands since 1950. *Global and Planetary Change*, 80-81:85 – 98, 2012.

[89] Thomas Frederikse, Karen Simon, Caroline A. Katsman, and Riccardo Riva. The sea-level budget along the northwest atlantic coast: Gia, mass changes, and large-scale ocean dynamics. *Journal of Geophysical Research: Oceans*, 122(7):5486–5501, 2017.

[90] J.-P. Montillet, T. I. Melbourne, and W. M. Szeliga. Gps vertical land motion corrections to sea-level rise estimates in the pacific northwest. *Journal of Geophysical Research: Oceans*, 123(2):1196–1212, 2018.

[91] H. Sandstrom. On the wind-induced sea level changes on the scotian shelf. *Journal of Geophysical Research: Oceans*, 85(C1):461–468, 1980.

[92] Jianke Li and Allan J. Clarke. Interannual flow along the northern coast of the gulf of mexico. *Journal of Geophysical Research: Oceans*, 110(C11), 2005.

[93] Christopher G. Piecuch, Sönke Dangendorf, Rui M. Ponte, and Marta Marcos. Annual sea level changes on the north american northeast coast: Influence of local winds and barotropic motions. *Journal of Climate*, 29(13):4801–4816, 2016.

[94] A.E. Gill. *Atmosphere-Ocean Dynamics*. International Geophysics. Elsevier Science, 1982.

[95] Yonggang Liu and Robert H. Weisberg. Ocean currents and sea surface heights estimated across the west florida shelf. *Journal of Physical Oceanography*, 37(6):1697–1713, 2007.

[96] Shoshiro Minobe, Mio Terada, Bo Qiu, and Niklas Schneider. Western boundary sea level: A theory, rule of thumb, and application to climate models. *Journal of Physical Oceanography*, 47(5):957–977, 2017.

[97] Philip R. Thompson, Mark A. Merrifield, Judith R. Wells, and Chantel M. Chang. Wind-driven coastal sea level variability in the northeast pacific. *Journal of Climate*, 27(12):4733–4751, 2014.

[98] John M. Huthnance. Ocean-to-shelf signal transmission: A parameter study. *Journal of Geophysical Research: Oceans*, 109(C12), 2004.

[99] Tal Ezer. A modeling study of the role that bottom topography plays in gulf stream dynamics and in influencing the tilt of mean sea level along the us east coast. *Ocean Dynamics*, 67(5):651–664, May 2017.

[100] Tal Ezer, Larry P. Atkinson, William B. Corlett, and Jose L. Blanco. Gulf stream's induced sea level rise and variability along the u.s. mid-atlantic coast. *Journal of Geophysical Research: Oceans*, 118(2):685–697, 2013.

[101] Jianjun Yin and Paul B. Goddard. Oceanic control of sea level rise patterns along the east coast of the united states. *Geophysical Research Letters*, 40(20):5514–5520, 2013.

[102] P. R. Thompson and G. T. Mitchum. Coherent sea level variability on the north atlantic western boundary. *Journal of Geophysical Research: Oceans*, 119(9):5676–5689, 2014.

[103] D. Stammer. Response of the global ocean to greenland and antarctic ice melting. *Journal of Geophysical Research: Oceans*, 113(C6), 2008.

[104] Nathan J. Mantua, Steven R. Hare, Yuan Zhang, John M. Wallace, and Robert C. Francis. A pacific interdecadal climate oscillation with impacts on salmon production. *Bulletin of the American Meteorological Society*, 78(6):1069–1079, 1997.

[105] Patrick F. Cummins and Gary S. E. Lagerloef. Low-frequency pycnocline depth variability at ocean weather station p in the northeast pacific. *Journal of Physical Oceanography*, 32(11):3207–3215, 2002.

[106] Lee-Lueng Fu and Bo Qiu. Low-frequency variability of the north pacific ocean: The roles of boundary- and wind-driven baroclinic rossby waves. *Journal of Geophysical Research: Oceans*, 107(C12):13–1–13–10, 2002. 3220.

[107] Philip Robert Thompson. *Sea surface height: A versatile climate variable for investigations of decadal change. [electronic resource].* [Tampa, Fla.] : University of South Florida, 2012., 2012.

[108] Dudley B. Chelton, Michael G. Schlax, Roger M. Samelson, and Roland A. de Szoeke. Global observations of large oceanic eddies. *Geophysical Research Letters*, 34(15):n/a–n/a, 2007. L15606.

[109] LuAnne Thompson and Jordan Dawe. Propagation of wind and buoyancy forced density anomalies in the north pacific: Dependence on ocean model resolution. *Ocean Modelling*, 16(3/4):277 – 284, 2007.

[110] Christopher G. Piecuch and Rui M. Ponte. Buoyancy-driven interannual sea level changes in the southeast tropical pacific. *Geophysical Research Letters*, 39(5):n/a–n/a, 2012. L05607.

[111] Christopher G. Piecuch and Rui M. Ponte. Buoyancy-driven interannual sea level changes in the tropical south atlantic. *Journal of Physical Oceanography*, 43(3):533–547, 2013.

[112] Matthew L. Perkins and Neil J. Holbrook. Can pacific ocean thermocline depth anomalies be simulated by a simple linear vorticity model? *Journal of Physical Oceanography*, 31(7):1786–1806, 2001.

[113] Jianke Li and Allan J. Clarke. Interannual sea level variations in the south pacific from 5° to 28°s. *Journal of Physical Oceanography*, 37(12):2882–2894, 2007.

[114] Angela M. Maharaj, Paolo Cipollini, Neil J. Holbrook, Peter D. Killworth, and Jeffrey R. Blundell. An evaluation of the classical and extended rossby wave theories in explaining spectral estimates of the first few baroclinic modes in the south pacific ocean. *Ocean Dynamics*, 57(3):173–187, Jun 2007.

[115] A. M. Maharaj, N. J. Holbrook, and P. Cipollini. Multiple westward propagating signals in south pacific sea level anomalies. *Journal of Geophysical Research: Oceans*, 114(C12):n/a–n/a, 2009. C12016.

[116] Kunihiro Aoki, Atsushi Kubokawa, Hideharu Sasaki, and Yoshikazu Sasai. Midlatitude baroclinic rossby waves in a high-resolution ogcm simulation. *Journal of Physical Oceanography*, 39(9):2264–2279, 2009.